

DISSERTATION

ASPECTS OF GULF SURGES AND TROPICAL UPPER TROPOSPHERIC
TROUGHS IN THE NORTH AMERICAN MONSOON

Submitted by

Andrew James Newman

Department of Atmospheric Science

In partial fulfillment of the requirements

For the Degree of Doctor of Philosophy

Colorado State University

Fort Collins, Colorado

Fall, 2011

Doctoral Committee:

Advisor: Richard Johnson

Sue van den Heever
Eric Maloney
Bogusz Bienkiewicz

Copyright by Andrew James Newman 2011

All Rights Reserved

ABSTRACT

ASPECTS OF GULF SURGES AND TROPICAL UPPER TROPOSPHERIC TROUGHS IN THE NORTH AMERICAN MONSOON

Gulf surges are transient events that propagate along the Gulf of California (GoC) from south to north, transporting cool moist air toward the deserts of northwest Mexico and the southwest United States during the North American monsoon (NAM). The general features and progression of surge events are well studied but the dynamical characteristics and evolution are still unclear. Tropical upper-tropospheric troughs (TUTTs) are another critical transient event occurring during the NAM that enhance precipitation on their western flank. The mechanism of precipitation enhancement associated with TUTT passage needs further refinement as well. To address these unknowns, a number of convection-permitting simulations are performed over the entire core monsoon region for the 12-14 July 2004 gulf surge and TUTT event that occurred during the North American Monsoon Experiment. This allows for extensive comparison with many observational platforms.

A control simulation is able to reproduce the surge event reasonably well, capturing all the important observed features on 12 and 13 July. The dynamical evolution of the surge event notes two distinct features, a precursor event on 12 July and the actual surge on 13 July. Using shallow water theory, the feature on 12 July is likely a coastally trapped, slightly non-linear Kelvin wave. This feature is important because it introduces cooler, moister air into the southern and central GoC. The surge signature

develops early on 13 July in the southern GoC and is likely a coastally trapped non-linear Kelvin wave throughout its lifetime. Sensitivity simulations show that the convective outflow is critical to the intensity of the simulated surge, in agreement with past studies. The removal of mountain gap flows into the GoC from the Pacific Ocean along the Baja Peninsula shows they are not critical in surge initiation and evolution; the surge and its general character remain.

A unique approach to examine the TUTT precipitation enhancement mechanism is used where the vorticity anomaly associated with the TUTT is removed in the initial conditions. It is shown that the TUTT likely enhances convection along the Sierra Madre Occidental (SMO) through slightly increased shear and slightly more convective available potential energy (CAPE) near the SMO. These slight differences lead to enhanced precipitation and microphysical evolution. The control simulation generates 23% more precipitation during the primary period of TUTT interaction with the SMO and has enhanced graupel, cloud and precipitation ice and supercooled liquid water contents, which is related to changes in lightning production.

Finally, two dimensional dry idealized simulations examine some attributes of the observed surge. The GoC LLJ, multiple convective outflows, and slope of the isentropes along the GoC all influence the character of the idealized surge. The slope of the isentropes, which is a consequence of the heat low over the Southwest US, is most important, followed by the convective outflows, and GoC LLJ. The sloped isentropes create a unique thermodynamic environment which significantly impacts gravity wave phenomena like Kelvin waves and bores. Convective outflows modulate surge intensity and its complexity while the GoC LLJ only enhances the surge intensity.

ACKNOWLEDGEMENTS

I'd like to thank my advisor, Richard Johnson, and my other committee members, Sue van den Heever, Eric Maloney and Bogusz Bienkiewicz for all their research guidance, discussions and revisions throughout this process. Many thanks also go out to the entire Johnson Research Group, specifically Paul Ciesielski, Brian McNoldy, and Rick Taft for all their help regarding computing, figures and observational data relating to this research. I'd also like to thank my parents, Paul and Beth, and the rest of my family for their love and support. Finally, and most importantly, I thank my wife Kathryn for always supporting me when I needed it and her thoughtful science discussions. This work was supported by NASA Headquarters under NASA contracts "NNX07AD35G", "NNX10AG81G", and by the National Science Foundation, Mesoscale Dynamic Meteorology Program, under grant ATM-0639461. I would also like to acknowledge high-performance computing support provided by NCAR's Computational and Information Systems Laboratory, sponsored by the National Science Foundation.

TABLE OF CONTENTS

ABSTRACT.....	ii
ACKNOWLEDGMENTS	iv
TABLE OF CONTENTS.....	v
LIST OF TABLES.....	viii
LIST OF FIGURES	ix
CHAPTER	
I. MOTIVATION AND GOALS	1
Introduction.....	1
General background.....	1
Gulf surge events and tropical upper-tropospheric troughs	3
Gulf surge events	3
Tropical upper-tropospheric troughs.....	5
Motivation and research goals	7
Motivation.....	7
Research goals	9
II. DATA AND METHODOLOGY	13
Observational data	13
Integrated sounding system.....	14
Aircraft observations.....	14

Radar network.....	15
Simulation methodology.....	17
Control simulation	19
Sensitivity simulations	20
Evaporation modification.....	20
Filled peninsular ranges	21
TUTT removal	23
Idealized simulations	27
III. OVERVIEW OF GULF SURGE FEATURES	32
Large-scale overview	32
Small-scale overview	35
Summary	40
IV. RESULTS AND DISCUSSION	41
Control simulation	41
Modeled and observed surge evolution	41
Precursor convective disturbances near mouth of Gulf of California, 12 July.....	41
Development of mature surge, 13 July	52
Evolution summary.....	65
Surge dynamics	65
Structure 2.....	68
Surge event.....	71
Southern and central GoC.....	71

Northern GoC.....	73
Dynamical summary	81
Topographic and microphysical modifications.....	82
No sub-cloud evaporation	83
Modified topography	87
Impacts of TUTT removal	95
Convection enhancement mechanisms	95
Divergence mechanism.....	96
Shear mechanism	100
Thermodynamic considerations	102
Combined mechanism.....	106
Microphysical aspects	110
Impacts on surge evolution	118
Summary	121
Idealized Simulations.....	124
V. CONCLUSIONS.....	130
Control simulation	130
Surge schematic	132
Modified topography and microphysics simulations.....	135
Impacts of TUTT removal	136
Idealized Simulations.....	140
REFERENCES	142
LIST OF ABBREVIATIONS.....	153

LIST OF TABLES

2.1	The five idealized simulation names and which process each simulation excludes.....	28
4.1	Total speed of the intense moisture flux associated with the leading surge impulse on 13 July. Uncertainty based on estimated position ambiguities using moisture flux to track the surge.....	58
4.2	Estimated values for H_1 , H_2 , θ_1 , θ_2 in the simulation for S2.....	68
4.3	Theoretical phase speeds using the estimated values in Table 4.2 for S2.	69
4.4	Theoretical phase speeds using the estimated values for the surge near KB.....	73
4.5	Estimated values for H_1 , H_2 , θ_1 , θ_2 in the simulation for the surge at PP.	78
4.6	Theoretical phase speeds using the estimated values in Table 4.5 for the surge at PP.....	78
4.7	Area (km^2) with moisture flux values greater than $150 \text{ g m kg}^{-1} \text{ s}^{-1}$ for the no_SUBCLD and control simulations at 08, 12, and 16 UTC 13 July.....	86
4.8	Area (km^2) with moisture flux values greater than $150 \text{ g m kg}^{-1} \text{ s}^{-1}$ for the no_gaps and control simulations at 08, 12, and 16 UTC 13 July.	95
4.9	Total precipitation (kg) between 18 UTC 12 July and 12 UTC 13 July for the TUTT and No_TUTT simulations in the region defined by Fig. 4.36.	110

LIST OF FIGURES

1.1. Overview of North American Monsoon region for the period of the 12-14 July 2004 surge event. Geographic and political boundaries are noted. The red line indicates the general path of tropical storm Blas, red L indicates center of surface heat low in desert southwest US, yellow line indicates path of TUTT for the case described in the next section, while the two surface high pressure centers are indicated by H	8
2.1. General core NAM region with the three ISS sites (large circles): Puerto Penasco (PP), Kino Bay (KB) and Los Mochis (LM) as well as the radar sites (stars): Cabo San Lucas (CSL), Guasave (GUA) and the NCAR S-Pol (SPOL) highlighted. The red circles denote the approximate range of the three radars.....	15
2.2. The domain for the 4 km simulations (shaded region) with topography, political boundaries and two cross-section (CS) lines. AG1 denotes the along -gulf CS the NOAA WP-3D made while AC1 denotes the across-gulf cross section the WP-3D performed.	18
2.3. 925 hPa wind magnitude (shading), vectors (arrows) and topography height (contours at 0, 500, 1000, 1500, 2000 and 2500 m) at 00 UTC 12 July. Areas in white are above 925 hPa.	21
2.4. The modified topography used in the blocked Peninsular Ranges simulation.	22
2.5. The NARR domain (shaded area) with the 20-km subset domain used for TUTT removal highlighted by bounding rectangle.	24
2.6. Potential temperature profile from the surface to 2200 m for the estimated GoC climatological profile (red) and the idealized marine inversion layer (blue) at grid point 450.	29
2.7. The base state potential temperature profile for all simulations except for the No_slope case.	30
3.1. 200 hPa (a-c) and 700 hPa (d-f) height (black contours (m)) and wind vectors for 12 UTC 11 July, 12 UTC 12 July, and 12 UTC 13 July.	34
3.2. 2-m air temperature (shading (K)), 10-m wind vectors (black arrows) and MSLP (black contours (hPa)) at 06 UTC 12 and 13 July.	35

3.3.	GOES infrared color enhanced brightness temperatures (K) over the core NAM region. (a) 12 UTC 12 July, (b) 15 UTC 12 July, (c) 21 UTC 12 July, (d) 00 UTC 13 July, (e) 06 UTC 13 July, (f) 12 UTC 13 July.	37
3.4.	NAME radar reflectivity. (a) 12 UTC 12 July, (b) 15 UTC 12 July, (c) 21 UTC 12 July, (d) 00 UTC 13 July, (e) 06 UTC 13 July, (f) 12 UTC 13 July.	38
3.5.	915 MHz wind profiler time series of spectral width from PP.	39
4.1.	Height contours (m) and wind vectors at (a) 200 hPa and (b) 700 hPa at 12 UTC 12 July.....	42
4.2.	(a, c) Observed and (b, d) model derived radar reflectivity (dBZ) using the WRF post processor. (a) and (b) at 12 UTC 12 July, (c) and (d) at 15 UTC 12 July. Black diamonds in 4.2(a), (c) denote the three radar sites. Black ring in 4.2(b), (d) denotes the approximate maximum observable range of the radar network.	43
4.3.	Along-gulf (AG1) cross section (CS) from NOAA WP-3D adapted from Mejia et al. (2010) (a) and from simulation (b). WP-3D CS runs from ~1300-1700 UTC, simulated CS taken at 1600 UTC. Potential temperature (orange lines) and mixing ratio (blue dashed line) contoured and wind barbs color coded by wind speed (a). Potential temperature (black lines) contoured and mixing ratio (shading) and wind vectors (arrows) are shown in (b). S1 denotes cold pool associated with convection near GoC entrance, S2 denotes a deeper disturbance discussed in Mejia et al. (2010). Black (a) and red (b) lines give general boundaries of S1 and S2.	45
4.4.	Same as Figure 4.3b except at 20 UTC 12 July. Red line marks general leading edge of S2.....	47
4.5.	Potential temperature (K) (a) and mixing ratio (g kg^{-1}) (b) at Los Mochis at 12 (solid) and 18 (dashed) UTC 12 July. The 12 UTC sounding occurred before the passage of S2 and the 18 UTC sounding after.	48
4.6.	975 hPa simulated wind magnitude (shading (m s^{-1})) and vectors (arrows) at 17 (a) and 20 (b) UTC 12 July. Areas in white are above the 975 hPa elevation level, while the thick black to light gray contours denote 500 m, 1000 m, 1500 m, 2000 m and 2500 m elevations respectively.....	49
4.7.	Simulated radar reflectivity factor (dBZ) at 1630 (a) and 1800 (b) UTC 12 July. The thick black contour denotes 1750 m.	50

4.8. First model level (~40 m AGL) potential temperature (shading (K)) and radar reflectivity factor at 20 and 40 dBZ (thick black and gray contours respectively) at 20 (a) and 2230 (b) UTC 12 July.	51
4.9. Same as Figure 4.1 except for 00 UTC 13 July.	52
4.10. Same as Figure 4.2 except for 0030 UTC and 0600 UTC 13 July.	53
4.11. Simulated top of the atmosphere (TOA) brightness temperatures (K) for 00 (a) and 12 UTC (b) 13 July.	54
4.12. 4.12. 950 hPa moisture flux ($\text{g m kg}^{-1} \text{ s}^{-1}$) at 04, 08, 12, 16 UTC 13 July. Red lines marked AC2-5 give the locations of four across the gulf cross sections used in later analysis.	56
4.13. The observed wind speeds (contours (m s^{-1})) and barbs (color coded by speed) are in (a), potential temperature (contours (K)) in (b) and modeled wind speed (shading (m s^{-1})), direction (arrows) and potential temperature (contours (K)) in (c). The black shading in (b) indicates topography. All panels are along across-gulf cross section (AC1).	59
4.14. Time series of surface temperature ($^{\circ}\text{C}$), dew point ($^{\circ}\text{C}$), and MSLP (hPa) at Kino Bay for the simulation (solid) and observations (dashed) (a), and the observed (b) and simulated (c) wind profile time series from 06 UTC 12 July to 00 UTC 14 July. Barbs in (b) and (c) indicate speed with full barb equal to 5 m s^{-1} and half barb equal to 2.5 m s^{-1}	62
4.15. Same as Figure 4.14 except for Puerto Penasco.	63
4.16. An idealized schematic in a two layer shallow water system of a disturbance moving along the inversion layer in the GoC. H_1 and H_2 denote the height of the top of the inversion before and after the leading edge of the disturbance passes. θ_1 represents the mass weighted potential temperature of the bottom and θ_2 is the temperature at the top of the inversion layer. The thin black line represents the inversion layer and the thick black line is the surface.	67
4.17. Same as Fig 4.13b, except taken along across-gulf cross section AC2 (shown in Fig. 4.12) at 16 UTC 12 July.	71
4.18. Same as Fig 4.13b, except taken along across-gulf cross section AC3 (shown in Fig. 4.12) at 03 UTC 13 July.	72
4.19. Same as Figure 4.5, except for Puerto Penasco.	74

4.20. Puerto Penasco anomalous MSLP (red (hPa)) from 18 UTC 12 July to 00 UTC 14 July. The mean NARR NAME period diurnal cycle MSLP was used to create the anomalies for the simulation	75
4.21. Potential temperature anomalies (shading (K)) and wind magnitude (white contours (m s^{-1})) at Puerto Penasco for 18 UTC 12 July to 00 UTC 14 July. The anomalies were calculated using the NARR NAME period mean diurnal cycle above the surface and the observed NAME mean diurnal cycle for the 2-m values	76
4.22. Simulated omega (neg. upwards (Pa s^{-1})) for Puerto Penasco from 18 UTC 12 July to 00 UTC 13 July from 50 to 3000 m.	77
4.23. Both cross sections are the same as Fig 4.13b, except (a) is taken along across-gulf cross section AC4 at 0930 UTC and (b) is taken along across-gulf cross section AC5 at 13 UTC 13 July.	80
4.24. Simulated reflectivity (dBZ) from the control run at 00 (a) and 06 UTC 13 July (c) and the no_SUBCLD (b) and (d) at the same times.	84
4.25. First model level (~40 m AGL) potential temperature (K) (shading) from the control run (a) and no_SUBCLD (b) at 00 UTC 13 July. The 20 (thick black) and 40 (thick gray) dBZ reflectivity contours are given for reference.	85
4.26. Same as Fig. 4.12 except for the No_SUBCLD simulation. The red box in (a) indicated the area used for the mean surge wind magnitude analysis.	86
4.27. 925 hPa wind magnitude (m s^{-1}) (shading) and vectors (arrows) at 00 UTC 12 July. Topography height (contours at 0, 500, 1000, 1500, 2000 and 2500 m with lighter shading indicating higher terrain). Areas in white are elevations above the 925 hPa elevation level.....	88
4.28. Difference fields (control – no_gaps) of Sfc to 850 hPa mass weighted mean specific humidity (g kg^{-1}) (a), potential temperature (K) (b), lowest 90 hPa above ground mixed layer CAPE (J kg^{-1}) (c) at 18 UTC 12 July, and potential temperature (K) at 06 UTC 13 July (d). Topography height (contours at 0, 500, 1500 m with lighter shading indicating higher terrain), with areas in white above the 850 hPa elevation level except in (c). White areas in (c) have convective inhibition $> 200 \text{ J kg}^{-1}$	90
4.29. Same as Figure 4.13b, except for a plane along 30°N for the control (a) and no_gaps (b) simulations at 00 UTC 13 July.....	91
4.30. Model soundings from the control (solid lines, black wind barbs) and the no_gaps simulation (dashed lines, red wind barbs) for 30°N , 114°W at 00 UTC 13 July.....	93

4.31. Same as Figure 4.12 except for the no_gaps simulation.....	94
4.32. 250 hPa TUTT - No_TUTT temperature (K) (a) and wind differences ($m s^{-1}$) (b) at 12 UTC 12 July. The black vectors in (b) denote the TUTT wind while the green are for the No_TUTT simulation.	96
4.33. 300 hPa TUTT difffluence ($\times 10^{-5} s^{-1}$) (a) and divergence ($\times 10^{-5} s^{-1}$) (c), and No_TUTT difffluence (b) and divergence (d) at 16 UTC 12 July.....	98
4.34. 400-200 hPa (a and b) and 700-400 (c and d) mass weighted vertical velocity ($Pa s^{-1}$) (negative upwards) for the TUTT (a,c) and No_TUTT simulations (b,d) at 16 UTC 12 July.	99
4.35. TUTT – No_TUTT 700-400 hPa (a) and Sfc-500 hPa (b) bulk shear ($m s^{-1}$). The black and green arrows in (a) denote the TUTT and No_TUTT simulations respectively. The black arrows in (b) display the shear difference vector. The light gray contour denotes the 750 m terrain elevation in both.	101
4.36. TUTT – No_TUTT 700-400 hPa (a) and Sfc-500 hPa (b) bulk shear ($m s^{-1}$). The black and green arrows in (a) denote the TUTT and No_TUTT simulations respectively. The black arrows in (b) display the shear difference vector. The light gray contour is the 750 m terrain contour in both.	103
4.37. TUTT (solid) and No_TUTT (dashed) temperature ($^{\circ}C$) (red) and dew point ($^{\circ}C$) (green) sounding for $30^{\circ}N$, $110^{\circ}W$ at 16 UTC 12 July. Wind barbs follow standard convention (knots) with black and red for the TUTT and No_TUTT simulations respectively.....	105
4.38. Average vertical velocity ($m s^{-1}$) for the TUTT (a) and No_TUTT (b) simulations with all grid points and model levels having $w > 1 m s^{-1}$ along the SMO between 22 and $32^{\circ}N$. The two black contours denote the $0^{\circ}C$ (lower) and $-20^{\circ}C$ (upper) average isotherms. All heights are AGL.....	107
4.39. Same as Figure 4.38, except for the vertical velocity differences, TUTT – No_TUTT.	108
4.40. TUTT – No_TUTT cumulative precipitation differences between 18 UTC 12 July and 12 UTC 13 July in mm. The narrow black contour denotes 0 m terrain height, along with 500 m (thick black) and 1000 m (gray).	109
4.41. For all grid points with condensate between 28 and $33^{\circ}N$ along the SMO, (a) shows the fraction of vertically integrated average condensate for graupel, snow and cloud water hydrometeor classes (TUTT is solid and No_TUTT is dashed) and (b) shows the total average vertically integrated condensate (kg m^{-2}). For the time period 16 UTC 12 July to 00 UTC 13 July.....	112

4.42. Average graupel mixing ratios (g kg^{-1}) for the TUTT (a) and No_TUTT (b) simulations using the same guidelines as Figure 4.41 for 16 UTC 12 July to 00 UTC 13 July. Again the two black contours denote 0°C (lower) and -20°C (upper) isotherms and heights are AGL.....	114
4.43. Same as Figure 4.42 except for the difference field, TUTT-No_TUTT.....	115
4.44. Total graupel (a) and supercooled water (b) mass (kg) for the TUTT (blue) and No_TUTT (red) simulations between 16 UTC 12 July and 0930 UTC 13 July.....	115
4.45. Potential temperature differences (TUTT – No_TUTT) (K) on the first model level (~40 m AGL) for 18 UTC (a) and 22 UTC (b) 12 July, and 02 UTC (c) and 06 UTC (d) 13 July. Areas shaded in white are above 1500 m elevation.....	119
4.46. Precipitable water differences (%) between the TUTT and NO_TUTT simulations for the grid point nearest 33°N, 113.5°W (located near the northern extent of the surge event) from 00 UTC 13 to 00 UTC 14 July.....	121
4.47. Initial potential temperature with both cold pools (a) while (b) displays the perturbation potential temperature. The primary cold pool is located near 220 km while the secondary cold pool is initialized near 550 km.....	125
4.48. Simulated potential temperature anomalies (shading) and wind magnitude (contours) for the base simulation in (a), with the observed half-hourly interpolated sounding derived potential temperature anomalies (shading) and half-hourly 915 MHz consensus winds (contours) in (b) for 00 to 16 UTC 13 July. Note the different scales for the potential temperature anomalies.	126
4.49. Same as Figure 4.48a, except for the No_LLJ (a), No_fric (b), No_bub (c), and No_slope (d) simulations.	128
5.1. General schematic of the evolution of important features on 12 July. The red X marks the general position of the TUTT around 12 UTC, the blue H and curved black line denote the position of the coastally trapped disturbance (S2) and corresponding higher MSLP around 12 UTC with the straight line ending near 28°N indicating motion and dissipation location, the heavy thunderstorm symbol denotes the location of the organized convective cluster around 09 UTC, while the dashed line and arrow give the location and movement of the TEW trough.	133

5.2. General schematic of the evolution of important features on 13 July. The red X marks the general position of the TUTT around 06 UTC. The blue S, black curve, thick black arrow denote the general initiation location of the gulf surge as well as its propagation, while the three thinner arrows denote the surge spreading into the northern GoC and desert US after 12 UTC. Smallest arrows indicate general areas of gap/inflow from Pacific Ocean before 12 UTC. The tropical cyclone symbol denotes the location of TS Blas around 12 UTC. The heavy thunderstorm symbols denote areas of more organized and persistent convection between 00-10 UTC while the moderate thunderstorm symbol (near 25°N) indicates less organized and persistent convection.134

CHAPTER I

MOTIVATION AND GOALS

1. Introduction

a. General Background

The North American Monsoon (NAM) is considered a “true” monsoon by nearly all authors (Adams and Comrie 1997). It has the typical characteristics of a monsoon, a seasonal wind reversal, and areas receiving a significant portion of their annual precipitation during the NAM (Carleton et al. 1990; Badan-Dangon et al. 1991; Douglas et al. 1993; Douglas 1995; Stensrud et al. 1995; Adams and Comrie 1997; Anderson et al. 2000a; Vera et al. 2006; Johnson et al. 2007). Higgins et al. (1999) show a mean onset date starting in early June around 15°N, progressing northward into Arizona by mid July. Retreat of the NAM then begins to occur in late September and progresses back down the Mexican coast into October (Vera et al. 2006). Examining precipitation data from Douglas et al. (1993) gives a northern boundary to the NAM of Arizona and New Mexico, defined by the 40% annual precipitation contour. Using the seasonal circulation to define the extent of the NAM, Tang and Reiter (1984) and Reiter and Tang (1984) determine the NAM extends to the Idaho-Utah border from eastern Oregon into Wyoming, which is the northern extent of summer monsoon convection. They designate the Rocky Mountains, Sierra Madre Occidental (SMO) and Mexican Plateau as the North American analog to the Tibetan Plateau.

Features of the NAM began to be noted in the literature roughly 90-100 years ago

(Campbell 1906; Beals 1922). These papers were mainly concerned with summer precipitation features of the Southwestern United States (US) and did not address the large-scale circulation changes seen with the NAM. Some authors did note such precipitation systems may be associated with the strong summer heat low found in the southwest US, which would draw Gulf of California (GoC) moisture northward due to the northward pointing pressure gradient force associated with the heat low (Ward 1917; Beals 1922). These papers seem to be the first to mention the GoC as an important moisture source for summer precipitation in the southwest US.

Reed (1933) used the development of the upper-air sounding network to plot the upper-level circulations. He discovered that an upper-level anticyclone “makes its first appearance in the spring, but it does not become fully established until mid-summer.” Reed (1933) also attributed the summer storms to the position of the high with an eastward (westward) position giving unstable (stable) conditions. However, it was not until Ives (1949) recognized that the summer circulation patterns in southwest North America (NA) were monsoonal in nature that the concept of the NAM came about. The first comprehensive climatology of the NAM was presented by Bryson and Lowry (1955). They noted that the onset of the monsoon generally occurred rapidly in early July and consisted of a shift in the mid-tropospheric circulation giving rise to the easterly flow regime found over southwest NA.

The results of Bryson and Lowry (1955) led to the idea that the Gulf of Mexico (GoM) was the primary source of moisture for the NAM as noted in other papers (Reitan 1957, Green and Sellers 1964; Hastings and Turner 1965). However, the findings of Reitan (1957) showed that a majority of the moisture was below 800 hPa thus raising the

question of how the GoM could be the dominant moisture source. Rasmusson (1967) showed strong moisture flux into the southwest US from the GoC with weaker fluxes from the GoM. Hales (1972) and Brenner (1974) introduced the concept of a “surge” of cool moist air providing moisture to the monsoon region from the tropical east Pacific channeled through the GoC. It is now generally believed that the GoC provides low-level moisture while the GoM provides upper level moisture to the core NAM region including the Mexican states of Sinaloa and Sonora and most of the US state of Arizona (Vera et al. 2006). The GoC provides the low-level moisture through the nocturnal low-level jet (LLJ), gulf surge events, sea/land breezes and the mountain circulation around the SMO (Hales 1972, 1974; Brenner 1974; Carleton 1985, 1986; Stensrud 1995; Adams and Comrie 1997; Berbery 2001; Fawcett et al. 2002; Douglas and Leal 2003; Vera et al. 2006).

b. Gulf surge events and tropical upper-tropospheric troughs

1) GULF SURGE EVENTS

Gulf surge events, or just surge events for short, are critical transient events in the NAM region because they have been tied to moisture flux and precipitation anomalies during the NAM (Anderson et al. 2000b; Berbery 2001; Douglas and Leal 2003; Gochis et al. 2004; Higgins et al. 2004) and possibly severe weather outbreaks in Arizona (Maddox et al. 1995). Hales (1972) and Brenner (1974) first introduced the concept of a “surge” of cool moist air providing moisture to the monsoon region from the tropical east Pacific channeled through the GoC. Hales (1972) describes several surge events and typical characteristics associated with them. These include: the surge is strongest just above the surface and decreases in strength with height, cooling will always coincide

with a surge in Arizona, and the surge is strongest at the onset then gradually decreases in strength. It was also noted that surges are generally associated with some type of cloudy disturbance south of the GoC as shown in satellite imagery (Hales 1972). Brenner (1974) highlights one surge case and notes that easterly waves, tropical cyclones or some other agent could initiate a surge event.

Surge classification of weak versus strong has been performed often in the literature (Hales 1972; Stensrud et al. 1997; Adams and Comrie 1997; Fuller and Stensrud 2000; Higgins et al. 2004; Higgins and Shi 2005; Adams and Stensrud 2007) with varying classification requirements. The classification procedure is done by using the different characteristics of surge events, rather than using a dynamical definition. In one classification scheme, strong surges are considered surges that occur along the length of the GoC and are typically associated with increases in precipitation more frequently (Hales 1972; Adams and Comrie 1997; Higgins et al. 2004; Johnson et al. 2007). Weak surges are considered surge events confined to the northern half of the GoC. Another classification scheme (Stensrud et al. 1997; Fuller and Stensrud 2000; Higgins et al. 2004) of surge events focuses on hourly observations from Yuma, Arizona. Surge onset is considered when the daily maximum dewpoint temperature rises rapidly and stays above 15.6 °C (60 °F) for several days. Strong surges occur when the maximum dewpoint increases or stays constant for the 3-day period after onset. Weak surges occur when the maximum dewpoint decreases in the 3-day period (Fuller and Stensrud 2000).

Statistical and modeling studies using these surge types have been performed to determine causes of both surge types (Stensrud et al. 1997; Fuller and Stensrud 2000; Higgins and Shi 2005; Adams and Stensrud 2007). Fuller and Stensrud (2000) show that

tropical easterly waves (TEWs) are precursors to many surges while Higgins and Shi (2005) show that tropical cyclones moving near the mouth of the GoC lead to a higher occurrence of strong surges. The Madden-Julian oscillation may even modulate surge events through its modulation on Eastern Pacific tropical cyclone genesis (Maloney and Hartmann 2000). Bordoni and Stevens (2006) use principal component analysis to show that a gulf surge mode is the leading empirical orthogonal function (EOF) in the region during the NAM season and that it relates strongly to TEW passage. The modeling studies of Stensrud et al. (1997) and Adams and Stensrud (2007) again show that TEWs are associated with surge events in some manner. Stensrud et al. (1997) developed a conceptual model for surge events that is still mostly applicable today. A TEW moves across Central America, initiating convection over the southern or central GoC. This convection or just the low-level convergence associated with the wave initiates a surge event. The idea of mid-latitude troughs influencing surge intensity (Stensrud et al. 1997) has been shown to be only weakly correlated with actual surge intensity (Fuller and Stensrud 2000). Adams and Stensrud (2007) perform two numerical integrations, one control with observed forcing and one with the TEW signal removed. The removal of the TEW signal changes the occurrence and strength of surge events but does not eliminate them entirely. They attribute these results to the incomplete removal of the easterly wave signal and/or model generation of easterly waves over the Mexican Plateau and SMO.

2) TROPICAL UPPER-TROPOSPHERIC TROUGHS

Tropical upper-tropospheric troughs (TUTTs) (Sadler 1967) are primarily middle to upper-level features. A positive vorticity maximum is typically found around 200 hPa with the corresponding circulation extending up to 100 hPa and weakly down to near 700

hPa. A maximum negative temperature anomaly of a few K is generally found around 300-400 hPa with a maximum warm anomaly around 125 hPa (Kelly and Mock 1982). The negative temperature anomaly can extend down to near 700 hPa (Kelly and Mock 1982; Whitfield and Lyons 1992). TUTTs in the NAM region typically form from the North Atlantic TUTT, or thinning troughs associated with wave breaking on the downstream side of the monsoonal ridge over Texas or the western GoM, (Thorncroft et al. 1993). They are then advected westward south of the monsoonal ridge (Finch and Johnson 2010). TUTTs in the NAM region are very similar in structure to those found elsewhere (Finch and Johnson 2010).

However, unlike TUTTs elsewhere, which have precipitation on the eastern side of the center of circulation (Sadler 1967; Kelly and Mock 1982) they have been shown to have enhanced convection on the western flank (Pytlak et al. 2005, Douglas and Englehart 2007; Bieda et al. 2009; Finch and Johnson 2010). Pytlak et al. (2005) developed a conceptual model of TUTTs in the NAM region and proposed that upper-level diffluence in the front right quadrant (west of the low center) leads to an increase in convection in that region. However, there is an issue with which came first: Is there diffluence because of the convection, or is the diffluence caused by the TUTT enhancing convection? Douglas and Englehart (2007) developed a climatology of transient events in the NAM and documented the precipitation around TUTTs. They found that rainfall is maximized to the west of the TUTT center but did not give an explanation to the observed precipitation pattern. Finch and Johnson (2010) examined a TUTT in the NAM region and concluded that convection over the SMO seems to be modulated by the TUTT through changes in the midlevel shear. The 700-400 hPa shear magnitude increases and

the shear vector changes direction such that it is more perpendicular to the SMO. This creates an environment where convection can organize, grow upscale and propagate off the SMO more readily than days without a TUTT present to the east of the SMO. Finally, Bieda et al. (2009) documented an increase in lightning frequency associated with TUTT passages, which further indicates that TUTTs modulate convection in the NAM region.

2. Motivation and research goals

a. Motivation

The North American Monsoon system is very complex with scale interactions ranging from the microscale through the synoptic scale. This makes study of the NAM difficult due to the range of spatial and temporal scales of important phenomena. These phenomena include: boundary layer meteorology, evapotranspiration, sea/land breeze, low-level jet, orographically forced convection, tropical cyclones and easterly waves, inverted upper-level troughs and interaction with midlatitude synoptic scale waves. By studying the NAM we can improve our understanding of these features thus improving our understanding of scale interactions, moisture transport, boundary layer meteorology and convection. The NAM region, shown in Figure 1.1, is also quite unique in the world for its distribution of landmasses, mountain ranges (i.e. Rocky Mountains, SMO and Peninsular Ranges) and bodies of water (e.g. GoM, GoC). The uniqueness of the NAM region and the complex scale interactions are compelling intellectual reasons to study the NAM.

Besides the intellectual importance of understanding the NAM, there are very important practical reasons to understanding the NAM, which are to protect and improve

quality of life in southwest NA. Regions of northwest Mexico and the southwest US receive 40-80% of their annual precipitation during the monsoon season (Douglas et al. 1993). This makes the NAM critical to regional water resource management, agriculture

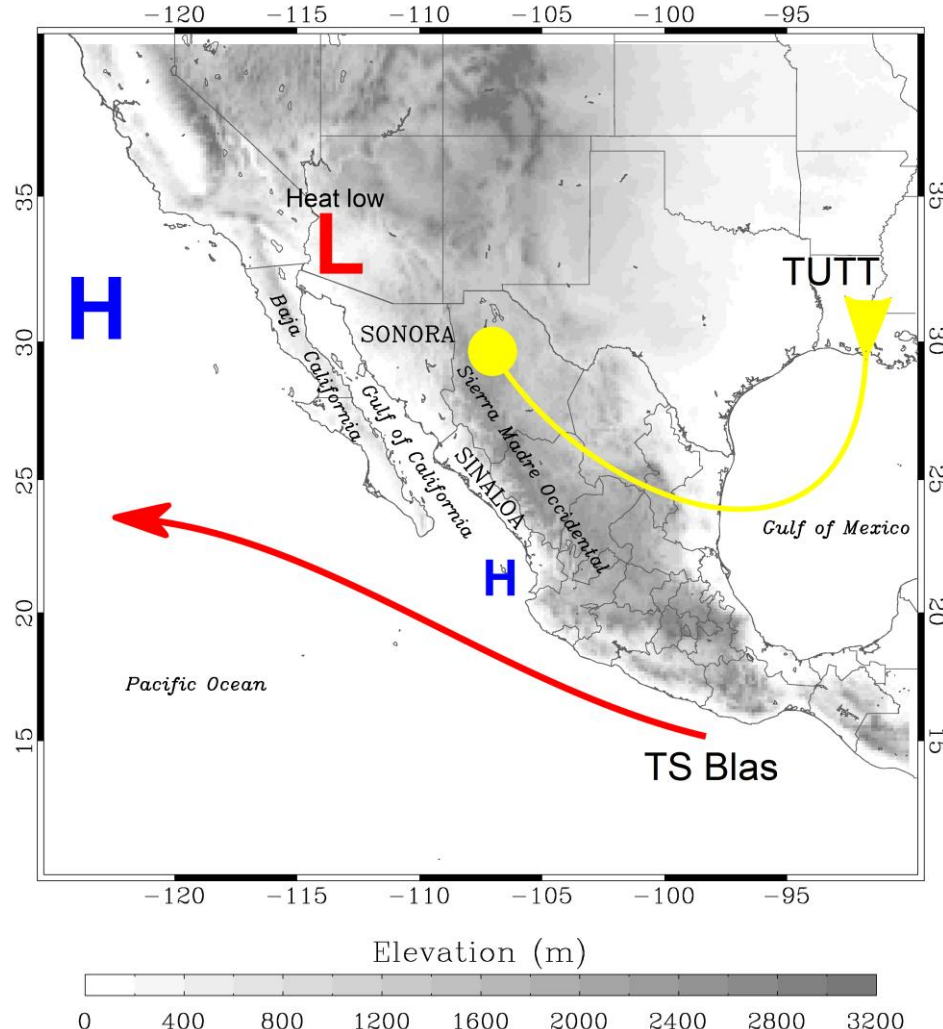


Figure 1.1. Overview of North American Monsoon region for the period of the 12-14 July 2004 surge event. Geographic and political boundaries are noted. The red line indicates the general path of tropical storm Blas, red L indicates center of surface heat low in desert southwest US, yellow line indicates path of TUTT for the case described in the next section, while the two surface high pressure centers are indicated by H.

practices, etc. Also, severe thunderstorm and flash flood events occur in the southwest US during the NAM (Hales 1975; Maddox et al. 1980; Maddox et al. 1995). To provide the public and emergency managers with ample lead time, accurate forecasts of these

events are required, which requires a detailed understanding of processes occurring in the NAM. In this way the intellectual reasons for studying the NAM dovetail with the practical reasons. Ideally, improved understanding of physical processes (i.e. boundary layer development, convection) allow for improved models of those processes. Improved models then lead to improved forecasting ability of sensible weather, directly impacting the practical reasons cited above.

Specifically, surge events modulate convection in the core NAM region and are likely associated with severe weather outbreaks in Arizona (Gochis et al. 2004; Maddox et al. 1995). The dynamics and evolution of these transient events are poorly understood. TUTTs also are known to modulate convection in the core NAM area (Douglas and Englehart 2007; Bieda et al. 2009; Finch and Johnson 2010) and may modulate surge events through their influence on convective organization. Gaining more insight into these two events satisfies in part the intellectual and practical motivational issues associated with the NAM.

b. Research goals

Most of the large-scale features associated with the initiation of a surge event were first identified over 35 years ago and have come to a consensus in the literature. They have been linked to TEW passage south of the GoC and strong surge events occur more frequently when a TC passes close to the mouth of the GoC (Hales 1972; Brenner 1974; Stensrud et al. 1997, Fuller and Stensrud 2000; Higgins and Shi 2005; Johnson et al. 2007; Adams and Stensrud 2007). The characteristics of surge events are also well studied (Hales 1972; Brenner 1974; Badan-Dangon et al. 1991; Anderson et al. 2000b; Douglas and Leal 2003; Bordoni and Stevens 2006; Rogers and Johnson 2007; Mejia et

al 2010). However, there are a few important aspects of surge events that are still unresolved. The largest unknown pertains to the dynamics of surge events and the dynamical evolution of them. Since the events occur in a data-sparse region, it has been difficult to unravel what type of phenomena a surge event is and whether it evolves from one type of system to another (i.e., gravity current to Kelvin wave) during its lifecycle. Zehnder (2004) examines a detailed list of possible linear dynamical mechanisms for surge events, but does not come to a definitive conclusion. Rogers and Johnson (2007), hereafter RJ2007, look at one strong surge event from an observational standpoint and conclude that a bore is the most likely suspect for the initial surge event. Mejia et al. (2010) examine the same surge using airplane data but cannot reach a definitive conclusion regarding the surge dynamics. Overall, the dynamical definition and evolution of surge events is uncertain.

The aspect of TUTTs influencing surge initiation and/or surge strength has also not been examined. An anecdotal link to strong surge events (Johnson et al. 2007; RJ2007; Bieda et al. 2009; Finch and Johnson 2010) seems to be present. But, how this linkage manifests itself or if it even exists is still quite unclear. It is hypothesized here that the TUTT influence on surge initiation and evolution manifests itself through the TUTT modulation of convective organization along the SMO. Finch and Johnson (2010) show that convective organization and propagation is enhanced along the SMO in areas where the TUTT modifies the midlevel shear vector as discussed above. Furthermore, the mechanism for convective enhancement on the western flank of a TUTT is still unclear as well. Finch and Johnson (2010) largely refutes the hypothesis of Pytlak et al. (2005), but their study has limited thermodynamic data and uses observational data at a

0.25° resolution. A high-resolution, explicit convection-permitting simulation should give a more detailed glimpse into how the Finch and Johnson (2010) mechanism evolves and if there is a thermodynamic component.

To examine these two areas, several research goals have been developed. The first is to use a high-resolution regional model to simulate a strong surge event that has a TUTT present before and during the surge event. Using observations from the North American Monsoon Experiment (NAME) (see chapter 2 for more information), the veracity of the simulated surge can be determined. Conclusions regarding initiation and the dynamical characteristics and evolution of the simulated surge event can be made with some confidence in a simulation that agrees well with observations. Sensitivity runs can then be performed to examine certain aspects of the surge event. Specifically, modification to evaporation will be performed to examine the influence of organized convective cold pools on initiation and evolution of the surge event. Altering the structure of the Baja California Peninsula topography will be done in another simulation to examine the influence of flow from the Pacific Ocean into the GoC. The removal of the TUTT through a potential vorticity inversion technique will be performed to investigate changes in the simulated surge and convective initiation and evolution. Finally, several very simple idealized simulations will be performed to examine how certain physical processes change the surge structure and to see if most of the observed surge features can be recreated with convective outflow proxies.

To summarize, surge events and at least most of their large-scale features and triggering events have been noted in the literature for almost 40 years (Hales 1972; Brenner 1974; Stensrud et al. 1997; Douglas and Leal 2003; Higgins et al. 2004; Adams

and Stensrud 2007; etc). However, it has only been more recently that their dynamics have been examined in more detail (Zehnder 2004; RJ2007; Mejia et al. 2010). These studies give some possible dynamical explanations for surge events, but leave a definitive answer still wanting. Also coming out of recent research is the possibility that TUTTs may influence surge initiation and/or strength. Following the spirit of Adams and Stensrud (2007), removal of the TUTT will be performed and the resultant simulation will be compared to the control run to assess any possible TUTT-surge link. Along with the TUTT removal simulation, modification to the rain evaporation component of the microphysics scheme will be performed to examine the effects of convective outflow on surge evolution in more detail. The topographic modification to the Baja California Peninsula simulation allows for examination of the importance of cold Pacific air intruding into the GoC. Idealized simulations will further examine the conclusions reached in the control simulation. All these simulations will allow for a more complete dynamical description of a surge event as well as some of the important factors influencing the evolution of such events.

CHAPTER II

DATA AND METHODOLOGY

1. Observational data

The NAME field campaign (Higgins et al. 2006) produced an unprecedented set of in situ and remotely sensed observations of the core NAM region, mainly the Sinaloa and Sonora regions in Figure 2.1 along with the GoC. The NAME dataset includes surface and upper-air observations, vertical wind profiling radars, the National Center for Atmospheric Research (NCAR) polarimetric radar (SPOL) along with two Mexican radars, surface flux sites, rain gauge network, aircraft observations and many other measurements (Higgins et al. 2006). The extended observational period ran from 1 July – 30 September 2004; however, many instruments were only in place from 1 July – 15 August.

During that period two strong surge events occurred, 12-14 July and 22-24 July 2004. The first event is the subject of this study and it was associated with tropical cyclone (TC) Blas and a TUTT. Also, the surge occurred during an intensive observing period (IOP), which includes increased rawinsonde launches and aircraft observations. Since the surge examined herein occurred during an IOP, a vast observational dataset exists to compare to the simulations. This is advantageous because without reassurance of a proper simulation through comparison to observations, any conclusions regarding the dynamics of the surge event will be less concrete. The following subsections give a brief overview of the research observation platforms used in this work.

a. Integrated sounding system

Three integrated sounding systems (ISS) were deployed from 7 July to 15 August at Puerto Penasco (PP), Kino Bay (KB) and Los Mochis (LM) (Figure 2.1). These systems are maintained by NCAR and contain a bevy of instrumentation. A surface station measuring temperature, pressure, relative humidity, wind speed and direction at 1-min intervals; a global positioning system rawinsonde sounding system measuring temperature, pressure, relative humidity, and wind speed/direction; a 915 MHz Doppler clear-air wind profiler (915 MHz profiler hereafter) measuring vertical profiles of wind speed/direction; and a radio acoustic sounding system (RASS) measuring vertical profiles of virtual potential temperature are all part of an ISS installation. The data are subject to quality control via NCAR developed algorithms and human inspection (RJ2007). The RASS data will not be used in this study due to the instrument being turned off at night. See RJ2007 for details concerning quality control of the ISS data. Model surface variables, wind profile time series and atmospheric soundings will be compared to the ISS data to give comparisons of the surface and vertical evolution of the surge event at the three ISS sites.

b. Aircraft observations

During IOPs a National Oceanic and Atmospheric Administration (NOAA) WP-3D aircraft was flown to sample the low-level structure of gulf surge events (Mejia and Douglas 2005). Temperature and wind speed/direction are sampled at flight level at 1 s resolution. During the 12-14 July surge event two flights were made, one on 12 July and one on 13 July. These data were examined in great detail by Mejia et al. (2010) and

provide vertical cross sections snapshots of the low-level structure of the surge event near its initiation and arrival in the northern GoC. Model cross-sections along the flight path will be compared to the flight cross-sections to assess the three-dimensional simulated surge structure.

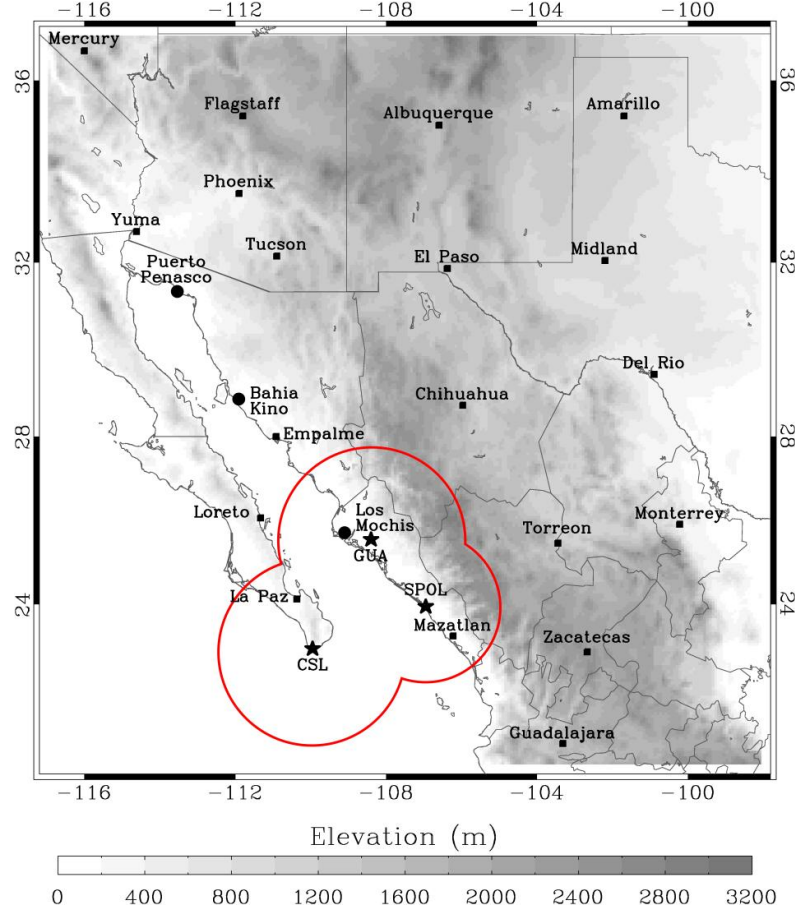


Figure 2.1. General core NAM region with the three ISS sites (large circles): Puerto Penasco (PP), Kino Bay (KB) and Los Mochis (LM) as well as the radar sites (stars): Cabo San Lucas (CSL), Guasave (GUA) and the NCAR S-Pol (SPOL) highlighted. The red circles denote the approximate range of the three radars.

c. Radar Network

The radar network dataset is a gridded dataset comprising the NCAR S-band polarimetric radar (S-pol) and two Servicio Meteorologico Nacional (SMN) Doppler radars with 2 km horizontal and 15 minute temporal resolution (Lang et al. 2007). It is

located in the southern NAM region around the mouth of the GoC (Fig. 2.1). The evolution of convection during the surge event appears to be critical to surge evolution, thus comparisons of simulated and observed reflectivity will be made. Qualitative comparisons at critical junctures on 12 and 13 July will give insight into the simulated convective evolution and help to highlight reasons for discrepancies between the simulation and observed surge.

Quantitative comparisons of reflectivity are not performed in this study due to the many pitfalls to comparing observed and simulated reflectivity. Perhaps the largest issue is developing derived radar reflectivity values. The Weather Research and Forecasting (WRF) post processor (WPP) uses WRF output, which does not include size distribution information, only mixing ratios (WRF-NMM Users Guide Version 3, 2011). Many assumptions about the size distributions present in precipitation are made to arrive at a simulated reflectivity, which may give rise to substantial errors (e.g., Marshall and Palmer 1948; Jones 1956). The second issue is that the NAME network uses only base elevation scans and produces a 2 km merged reflectivity product every 15 minutes (Lang et al. 2007). Radar scanning and earth geometry dictate that observed reflectivities far from all radar sites may be several kilometers above ground, while observations near a radar may only be several hundred meters above ground. The simulated product shown in this work is taken from the first model level above ground (~40 m). Finally, calibration biases in any of the three radars may also introduce systematic differences between the radar sites of a few dB (Anagnostou et al. 2001). Overall, it would be very difficult to correct for all these issues and is outside the scope of this work; therefore only general qualitative comparisons are done throughout this study. That being said,

qualitative comparisons of reflectivity are very useful to determine if the simulation is modeling convective features with the correct spatial and temporal features.

2. Simulation methodology

The ARW core of WRF version 3.2 was used for all real data simulations. The WRF Version 3 modeling system user's guide (2010) provides more details about WRF. For this work, only one high-resolution domain was used. The domain is 2000×2320 km with a horizontal grid spacing of 4 km (500×580 points) and 55 vertical levels between the surface and 100 hPa. The vertical grid is stretched such that it has seven levels in the lowest 1 km to a constant Δz of ~340 m in the upper-troposphere. In all simulations the Rapid Radiative Transfer Model longwave, Dudhia shortwave, Thompson et al. (2008) double moment microphysics, Noah land surface model, and Quasi-Normal Scale Elimination (QNSE) surface and boundary layer schemes are used. Figure 2.2 shows the 4 km domain topography and political boundaries for orientation.

Initial sensitivity simulations (not shown) indicate that the successful simulation of the surge event relies in part on the placement of the domain boundaries. It was found that the domain has to be large enough to capture TC Blas, the SMO and Baja ranges, a portion of the southwest US heat low and the TUTT. A nesting approach was not used because it was deemed important to attempt to explicitly resolve TC Blas and any convective systems associated with the TUTT and diurnal convection along the SMO. As discussed prior, TCs show a positive correlation with surge events and TUTTs influence convection along the SMO. To rely on convective parameterizations for some critical convective features, but not others was deemed inappropriate. It was also found that convective initiation over the SMO has some sensitivity to the number of vertical

levels. The simulation solutions become convergent when performed with over 50 vertical levels. The exploration into the causes of the vertical sensitivity is outside the scope of this work.

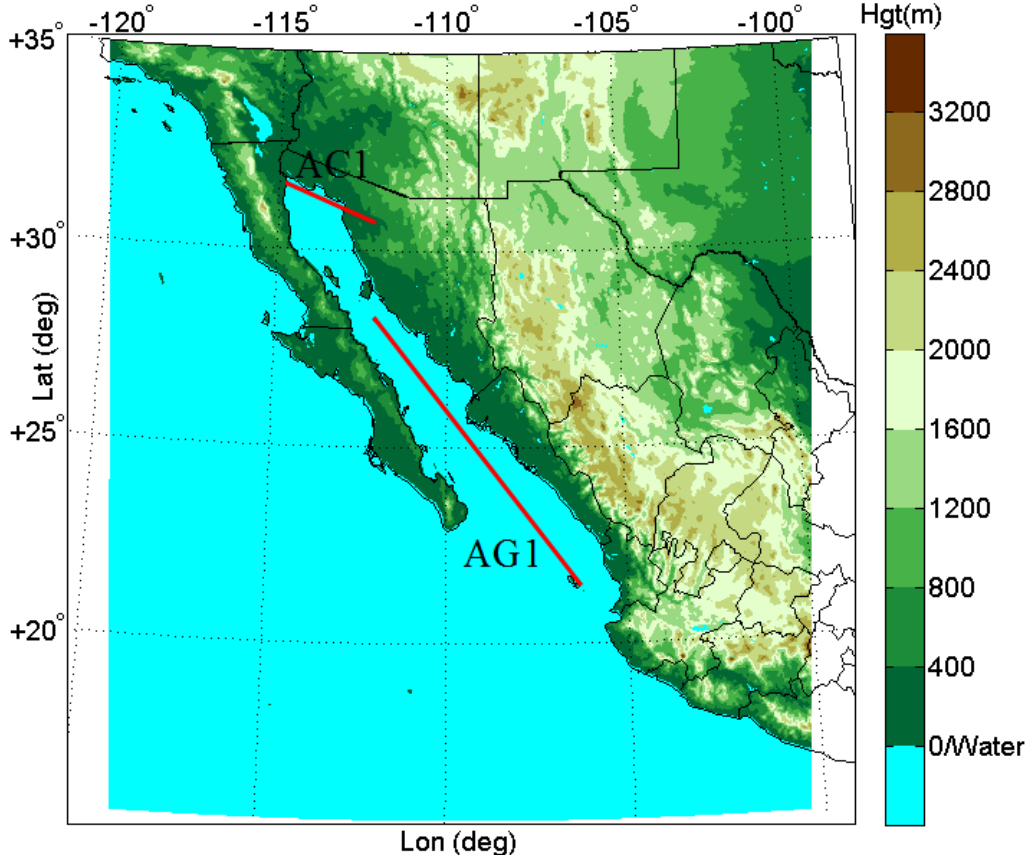


Figure 2.2. The domain for the 4 km simulations (shaded region) with topography, political boundaries and two cross-section (CS) lines. AG1 denotes the along-gulf CS the NOAA WP-3D made while AC1 denotes the across-gulf cross section the WP-3D performed.

A 4 km grid spacing is not sufficient to be called a true convection-resolving simulation (Bryan et al. 2003; Bryan and Morrison 2011), however it should be adequate to resolve convective systems and many mesoscale features. For this work a true convective resolving resolution is impractical due to the large domain size and multiple simulation requirements and is most likely not necessary. Successful simulation of TC Blas and convective clusters along the SMO, their corresponding cold pools and the

actual surge event can be performed with a convection-permitting simulation (Li et al. 2008; Weisman et al. 2011). There will be some discrepancies, like the smoothing and weakening of convective gust fronts, convective updrafts that will be slightly oversized and have lower vertical velocities and less entrainment (Bryan and Morrison 2011), but the dynamics of the surge event and certainly the TUTT should not be changed by a slightly coarser horizontal resolution. To examine if there are significant horizontal resolution effects, a large (2100×2400 km) 2 km run with 61 vertical levels was performed over the same domain as above with the same physics options. The surge evolution from this run is very similar to the 4 km run, giving confidence that the surge event is simulated correctly in the 4 km simulations.

a. Control Simulation

A control simulation of the surge event was made using the North American Regional Reanalysis (NARR) for initial and boundary conditions. The NARR is produced 8 times daily (3 hr interval) with 29 vertical levels from 1000 to 100 hPa at 32 km horizontal resolution (Mesinger et al. 2006). The NARR has been shown to have some deficiencies in the NAM region (Ciesielski and Johnson 2008), particularly with low-level moisture and the GoC low-level jet (GoC LLJ), but it is still believed to be the best available starting point. This is mainly due to the fact that the North American Model (NAM) and Rapid Update Cycle (RUC) model analyses do not extend far enough south to capture TS Blas and the Global Forecast System (GFS) and European Center for Medium Range Forecasts (ECMWF) analyses are at too coarse a resolution ($0.5\text{--}1^\circ$) to properly capture the flow reversal in the GoC. The control simulation was initialized at 12 UTC 11 July and integrated until 00 UTC 14 July. All analysis begins at 06 UTC 12

July giving 18 hours of spin-up time for WRF to generate the appropriate higher resolution circulations and precipitation features.

b. Sensitivity Simulations

In an attempt to unravel some of the important influences on the surge evolution, several modifications to the control run were made. These runs will then be compared to the control run to evaluate the impacts the modifications have on surge evolution. The first modified run examines microphysical influences directly through the removal of sub-cloud evaporation. The reason for this sensitivity test is that there is evidence from the control simulation that convective outflows along the coastal plain of the SMO are the driver of the initial surge event. The second probes the influence of the topography of the Baja Peninsula and the possible role of gaps in the mountain range contributing to the surge. The rationale and methodology used in these sensitivity tests are as follows.

1) Evaporation modification

To directly examine the influence of convection on surge evolution, a modification to the Thompson microphysics scheme was made to remove sub-cloud evaporation. Cloud base is computed at each grid point by determining the lowest level having a cloud water mixing ratio above 0.1 g kg^{-1} and no rain or cloud water evaporation is allowed to take place below that level. This is a less intrusive way to modify the microphysics, yet substantially modify the mechanisms of convective outflow generation. The selective removal of sub-cloud evaporation still allows for outflow generation via precipitation loading, melting ice, and evaporatively cooled air originating above cloud base, but should have substantially weaker cold pools than the control simulation.

2) Filled Peninsular Ranges

Another possible influence on surge evolution is the topographical structure of the Baja California Peninsula. The Peninsular Ranges (see Figure 1.1) extend along the length of the peninsula with a representative height of around 500 m. However, there are many peaks higher than 500 m with some over 1200 m, along with low spots of only a couple hundred meters. This results in a barrier with many gaps open to the Pacific Ocean, allowing flows into the GoC from the cool dome of air in the North Pacific (Anderson et al. 2001, Bordoni et al. 2004). An example of the gap flows is given in Figure 2.3. This influx of cool dense air into the central and northern GoC is expected

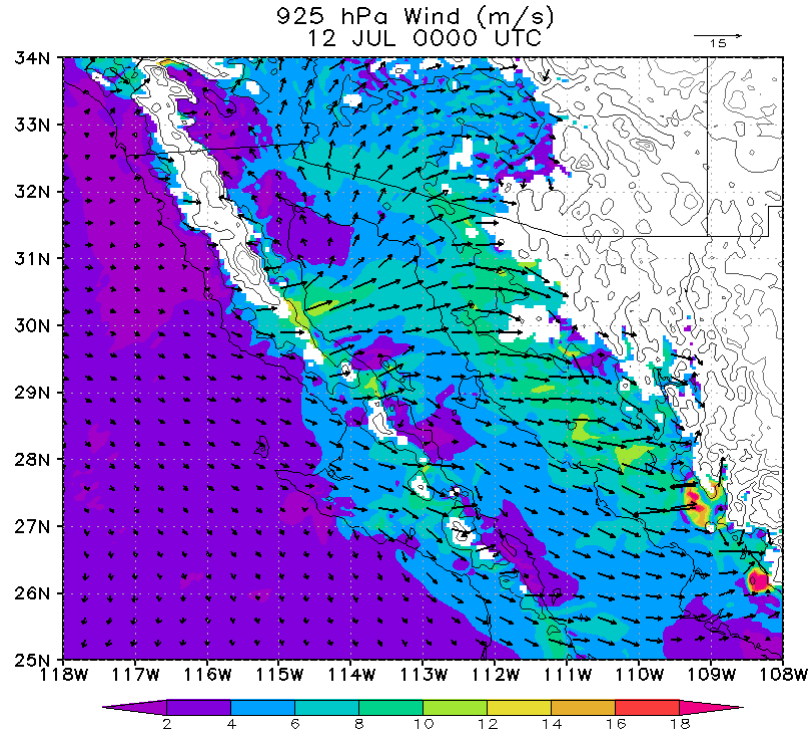


Figure 2.3. 925 hPa wind magnitude (shading), vectors (arrows) and topography height (contours at 0, 500, 1000, 1500, 2000 and 2500 m) at 00 UTC 12 July. Areas in white are above 925 hPa.

to influence the evolution of the surge event through a couple of possible mechanisms. The first is the cool dense air helps reinforce the boundary layer inversion present in the

GoC helping to create an environment conducive to propagating features such as internal bores. The second is that the Pacific air reaches the eastern coast of the GoC in a modified form, which is cooler and drier than the average, weakening convection in the region. Weakening of convection would lead to weaker convective outflow and a weaker initial surge event.

To test these ideas, the topography along the Peninsular Ranges is modified such that nearly all points along the peninsula from the southern end to 31.5°N will be set to 1000 m to create a continuous barrier along the peninsula (Figure 2.4).

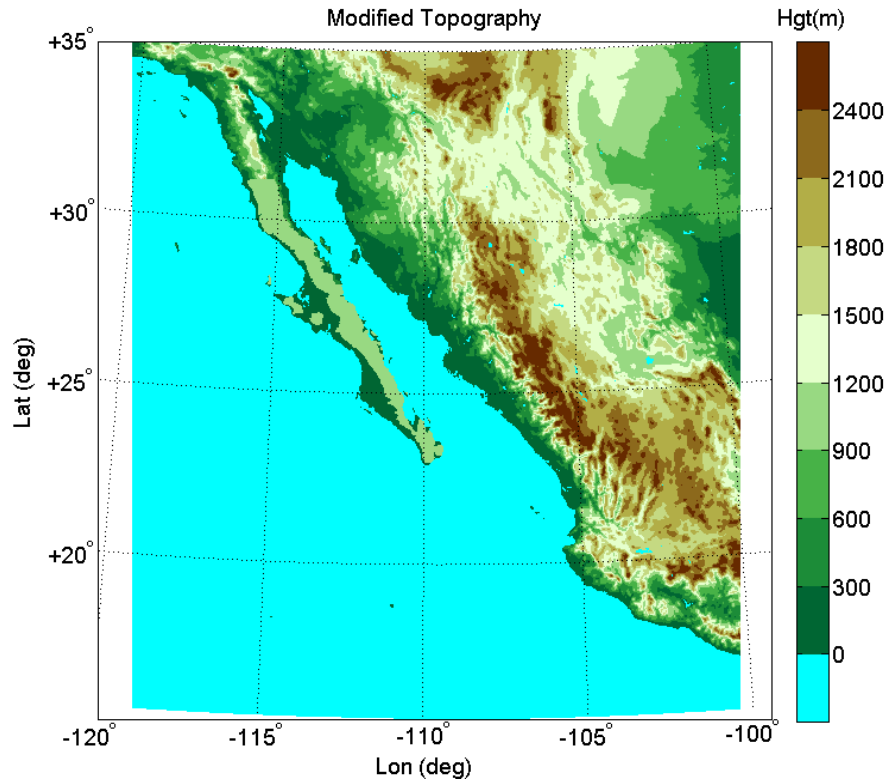


Figure 2.4. The modified topography used in the blocked Peninsular Ranges simulation.

North of 31.5°N the Peninsular Ranges are continuously above ~900 m in elevation. This will block all gap flows and nearly all flow into the GoC from the Pacific Ocean. There will still be a small amount of flow over the artificial barrier, but it will be significantly

less than in the control run. Comparisons between the modified topography run and the control run will be made to highlight which mechanism seems to be more important and how the surge evolution is modified.

c. TUTT removal

It is hypothesized that the TUTT may influence surge evolution through modification of the convection along the SMO. It has also been shown that TUTTs enhance precipitation on the western flank (Douglas and Englehart 2007; Bieda et al 2009; Finch and Johnson 2010) and a full understanding of the mechanism responsible is still unresolved. Thus, two simulations, one base run with the TUTT and a second run without the TUTT will be performed. Comparisons between them will highlight how the absence of the TUTT influences surge evolution and convective enhancement along the SMO.

To remove the TUTT from the NARR data, a 20 km horizontal grid space domain covering a large subset (7400×4900 km) of the NARR was created and displayed in Figure 2.5. The WRF Preprocessing System (WPS) was used to create the 3 hr analyses on the 20 km domain grid. The domain was created such that the TUTT circulation resided entirely inside the domain at the initial time, which was selected as 12 UTC 12 July. A modified version of the TC bogus scheme was then used to remove the vorticity anomaly associated with the TUTT. The TC bogus scheme removes a vorticity center in WPS data files that can then be used to create initial and boundary conditions for simulations.

The standard bogussing scheme begins by searching for the vortex center in the 1000 hPa analysis data as defined by the maximum in relative vorticity within a 400 km

radius of a point specified by the user. For this simulation the actual vortex center was

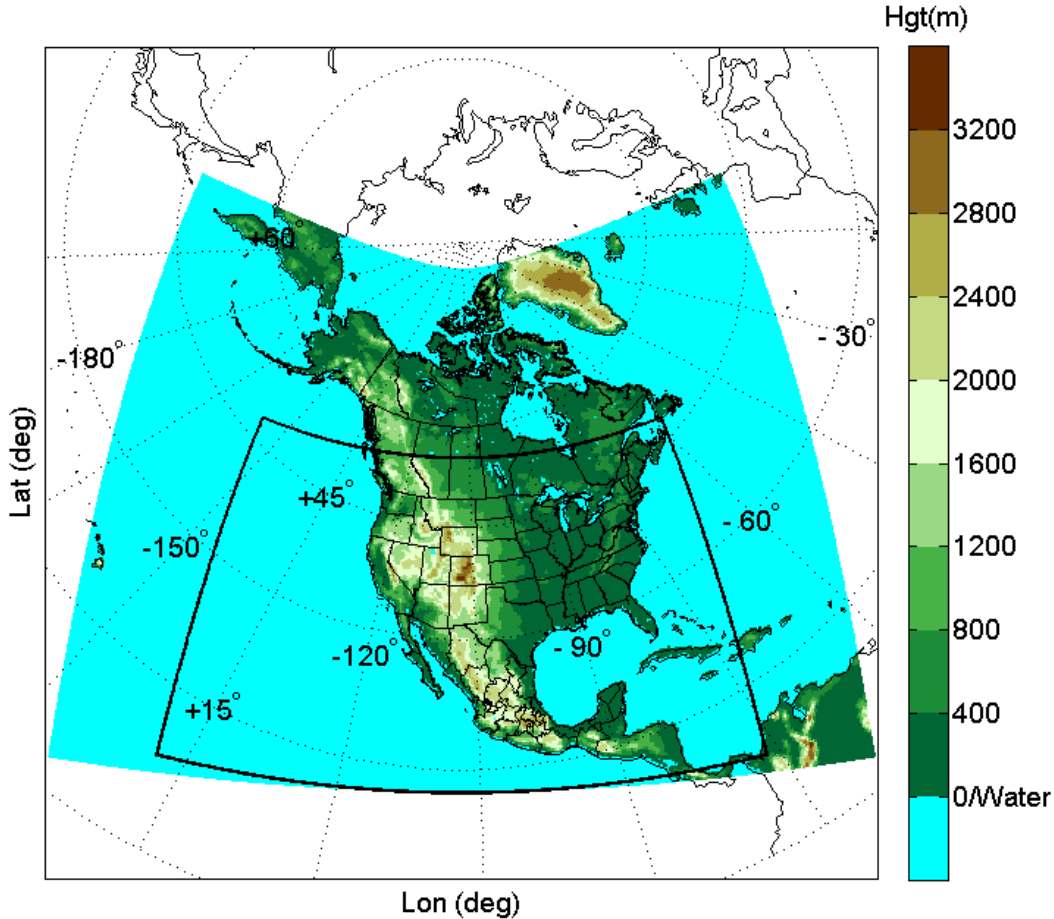


Figure 2.5. The NARR domain (shaded area) with the 20-km subset domain used for TUTT removal highlighted by bounding rectangle.

specified because the relative vorticity of a TUTT is much more diffuse than a TC and the search algorithm may struggle finding the correct center of the TUTT. The vortex center was determined through examination of the NARR relative vorticity and wind fields. The scheme then removes the vortex from each level to the model top. In this case, TUTTs are upper-level features so the removal scheme was modified to only remove relative vorticity above 600 hPa, as this TUTT was relatively weak below this level (Finch and Johnson 2010). The standard bogus scheme removes all relative

vorticity and divergence within a 300 km radius from the vortex center, but for this application the radius is increased to 650 km due to the larger scale of the TUTT.

The vorticity and divergence removal algorithm is described in the WRF documentation and in Fredrick et al. (2009). It starts with the following relationship for vorticity:

$$\nabla^2 \psi = \zeta \quad (2.1)$$

where ψ is the stream function for the non-divergent wind and ζ is the relative vorticity. To obtain the non-divergent wind for the vortex, first the relative vorticity is set to zero outside the vortex radius (650 km from vortex center in this case). Then the Dirichlet boundary conditions stream function is defined to be zero and the method of Successive Over-Relaxation (SOR) is used to solve Eqn. 2.1 on all pressure surfaces included in the calculation (every level at and above 600 hPa for this study). The non-divergent wind is then calculated from:

$$v_\psi = \hat{k} \times \nabla \psi \quad (2.2)$$

The non-divergent wind is then subtracted from the analysis U and V values.

The calculation and removal of the divergent wind associated with the vortex follows a similar procedure. First:

$$\nabla^2 \chi = \delta \quad (2.3)$$

Where χ is the velocity potential and δ is the divergence, which is obtained from the analysis. For the divergent wind case, the divergence is set to zero outside the radius of influence of the vortex, the boundary conditions are specified as above and the SOR method is used to solve Eqn 2.3. Then the velocity potential is calculated using the following:

$$v_\chi = \nabla \chi \quad (2.4)$$

The divergent wind is calculated from Eqn. 2.4 and is then subtracted from the analysis U and V^l .

After the wind field is modified the corresponding height and temperature perturbations are removed. First the height anomaly is found, again with a similar procedure as above. The following relationship between geostrophic vorticity and the height field is solved using SOR:

$$\nabla^2 \phi = \zeta_g f_0 \quad (2.5)$$

where ζ_g is the geostrophic vorticity and f_0 is a reference Coriolis force value. The geostrophic wind is calculated using:

$$v_g = \hat{k} \times \nabla \phi \quad (2.6)$$

And then v_g is subtracted from the analysis field. The temperature anomaly is removed from the analysis using the perturbation height calculated prior and the hydrostatic approximation in the form:

$$\partial \phi' / \partial \ln(p) = -RT' \quad (2.7)$$

where p is the pressure and R is the gas constant for dry air. The vortex is now removed from the analysis and only the estimated background mass and momentum fields are left. These fields are then output to WPS format files for ingestion to create initial and boundary condition files for simulations sans vortex.

Once the vortex is removed from all the NARR fields on the 20 km domain, initial and boundary conditions are created for the 4 km domain (Figure 2.2) and a

¹ The TC bogus scheme removes the rotational and divergent wind because it is designed for tropical cyclone removal. In this case the divergent wind is likely to be small but removed anyways for ease of use.

² Ciesielski and Johnson (2008) show the NARR has an excessively strong GoC LLJ, which is related to

simulation is run from 12 UTC 12 July to 00 UTC 14 July. A corresponding control run initialized at 12 UTC 12 July is also performed since atmospheric simulations are sensitive to the initial conditions (Lorenz 1963). This control run is used as the comparison basis for examining the impact of TUTT removal on the simulated convective and surge evolution. Various difference fields are used to highlight the important features influencing any evolution differences between the two runs.

d. Idealized simulations

In an attempt to further define which surge processes create some of the observed features of the surge at Puerto Penasco, idealized simulations with the Bryan Cloud Model (CM1) (Bryan 2002; Bryan and Fritch 2002) are performed. CM1 is highly configurable and tailored to performing various idealized simulations with or without many physical processes (i.e. friction, surface fluxes, microphysics) using any user defined initial conditions. For this study, two dimensional dry simulations simulating an along the GoC cross-section are made for five different cases, each excluding a different physical processes thought to be important in defining the observed surge features. The domain is set to 1200 km long with a horizontal resolution of 2 km, a vertical resolution of 150 m, model top at 10 km and an integration time of 16 hours. Two dimensional simulations without terrain were chosen to limit the complexity of the simulation and focus on only a few aspects of the surge. In a two-dimensional framework, internal gravity waves are a possible solution. Kelvin waves and bores are simply special cases of internal gravity waves thus Kelvin wave and bore like features are possible in the two-dimensional framework.

Internal gravity waves are generated by the introduction of cold pool(s) at various locations in the domain at the initial time and extending forward in time for two hours. The cold pools have a minimum potential perturbation of -7 K and decay away from the center point as a function of the cosine of the absolute distance from the center point. First a large cold pool with a radius of 220 km is placed in the southern third of the domain, and approximates the main surge feature seen in observations. A second slightly smaller cold pool with a radius of 150 km is placed in the center of the domain and approximates the convective outflow seen in the north-central GoC, which is likely responsible for the leading bore feature observed at PP near 0930 UTC 13 July.

Table 2.1 summarizes the five simulation names and which process is excluded from each simulation. The four attributes examined are the GoC LLJ, surface friction, the inclusion of the secondary cold pool, and the potential temperature profile. To include the GoC LLJ, the wind speed is increased by 2 m s^{-1} over the northern half of the domain over a period of four hours, starting nine hours into the simulation, and then decreased by 1.5 m s^{-1} through the end of the simulation. This approximates about three-quarters of a diurnal cycle in the GoC LLJ as shown in Douglas et al. (1998). The GoC climatology during the NAME period has a slope to the isentropes with lower potential temperatures near the mouth of the GoC in the lowest 1.5 km and higher potential temperatures over the deserts of the southwest US (Johnson et al. 2007). Estimates of the slope of the isentropes are made and used to create the basic state in the lowest two km. For the simulation without the sloped isentropes, a homogeneous base state with an inversion near 750 m across the entire domain is used. This inversion height is near that of the observed marine layer inversion. Figure 2.6 shows the base state potential

temperature profile at a grid point for the estimate of the GoC climatological profile and the homogeneous inversion. The base state sloped potential temperature from the surface to 2.5 km along the entire simulated cross-section is given in Fig. 2.7.

Table 2.1. The five idealized simulation names and which process each simulation excludes.

Simulation Name	Attribute Excluded
base	None
No_LLJ	GoC LLJ
No_fric	Surface friction
No_pool	Secondary cold pool
No_slope	Sloped isentropes

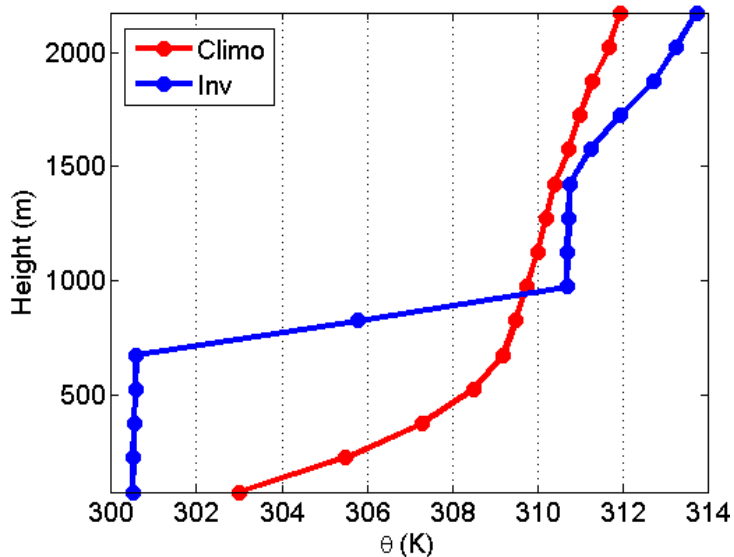


Figure 2.6. Potential temperature profile from the surface to 2200 m for the estimated GoC climatological profile (red) and the idealized marine inversion layer (blue) at grid point 450.

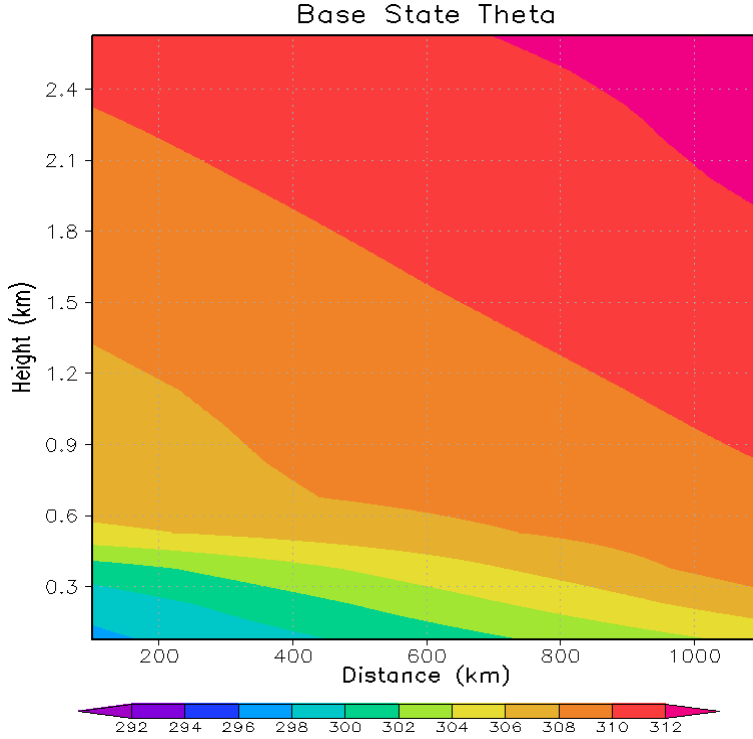


Figure 2.7. The base state potential temperature profile for all simulations except for the No_slope case.

A base simulation that is deemed the most realistic of the simulations and includes all attributes excluded from the other four simulations including: the GoC LLJ, surface friction, the secondary cold pool and the sloped isentropes, is performed first. From there, the simulations exclude one of the processes while including all others. This allows for comparisons between the different simulations to see how the exclusion of a specific process changes the surge features. Surface heat fluxes are not included in any simulation due to the simple nature of inclusion in CM1. The version of CM1 (R14) used for this work does not include a land surface model. Instead, surface fluxes in CM1 are based on a constant, user specified surface temperature, and an exchange coefficient (C_e) that varies with wind speed or is also user specified. With extreme daytime solar heating over the northern GoC land surface, it was deemed that the simple constant flux scheme

in CM1 would not suffice. Therefore all five simulations are performed without the CM1 surface flux parameterization operating.

The strong daytime heating was also the deciding factor for limiting the simulations to 16 hours. The idealized simulations and placement of the cold pools are setup such that they are initialized effectively around 00 UTC, (near peak of observed convection) and the simulated surge will arrive at a point about 800 km away from large cold pool near the time of observed surge arrival at Puerto Penasco for ease of comparisons. Approximately four hours (16 UTC) after the arrival of the strongest observed winds, strong solar heating is beginning to occur in reality. This is then the end of the simulation and allows the idealized simulations to capture the arrival of the initial surge features as well as the maximum wind core and the first hours of surge weakening.

CHAPTER III

OVERVIEW OF GULF SURGE FEATURES

1. Large-scale overview

The synoptic environment associated with the 12-14 July surge event was conducive to the occurrence of a strong surge event. Figure 3.1a-c displays the NARR 200 hPa heights (contours) and wind vectors from 12 UTC on 11-13 July; Figure 3.1d-f the 700 hPa heights (contours) and wind vectors for the same times. Figure 3.2 displays surface mean sea level pressure (MSLP) 2-m temperature and 10-m wind vectors at 06 UTC 12 and 13 July. At 200 hPa, the formation of a TUTT occurs on 8-9 July over the eastern Gulf of Mexico (GoM) from a thinning shortwave trough rounding the crest of the monsoon high with a closed circulation forming on 10 July (not shown). The circulation then begins to move westward under the upper-level monsoon high to the western GoM by 12 UTC 11 July (Fig. 3.1a) (Finch and Johnson 2010). The TUTT continues to have a closed circulation on 12 July while moving westward to near the SMO axis over central Mexico at 12 UTC 12 July (Fig. 3.1b). From that point, the TUTT begins to weaken and move nearly due north to near the Mexico/Texas border at 12 UTC 13 July (Fig. 3.1c) and dissipates by 00 UTC 14 July (not shown). During the evolution of the TUTT, the monsoon ridge center is displaced northward into Arizona, which in concert with the TUTT produces enhanced upper-level easterlies over the SMO on 11-13 July (Fig. 3.1a-c).

The tropical easterly wave (TEW) that develops into TS Blas can be seen in Figure 3.1d at 12 UTC 11 July near 11°N , 105°W with an inverted trough extending up the western coast of Mexico. The inverted trough along the western coast of Mexico associated with Tropical Depression (TD) Blas on 12 UTC 12 July (Fig. 3.1e) likely played a role in the formation of convection along the southern GoC between 06-18 UTC, 12 July. TD Blas develops into TS Blas by 18 UTC 12 July with the center of circulation moving west-northwest to a point within 5° of the tip of the Baja California Peninsula between 12 UTC 13 July (Fig. 3.1f) and 00 UTC 14 July (not shown) as a weakening TS. At the surface, the surface low associated with TS Blas can be seen near the 700 hPa center (Fig. 3.2a-b). An abnormally strong heat low is present in the southwest US deserts on 12 July as indicated by examining surface pressure anomalies (see RJ2007). On late 12 and early 13 July (Fig. 3.2b), surface ridging is present between TS Blas and the southwest US heat low creating an enhanced pressure gradient along the GoC. This ridging may be related to subsidence between TS Blas and the southwest US heat low, or an extension of the subtropical high building in the GoM on 12-13 July. Finally, northwesterly flow to the west of the Baja ranges can be seen in association with the East Pacific subtropical high (Fig. 3.2a-b).

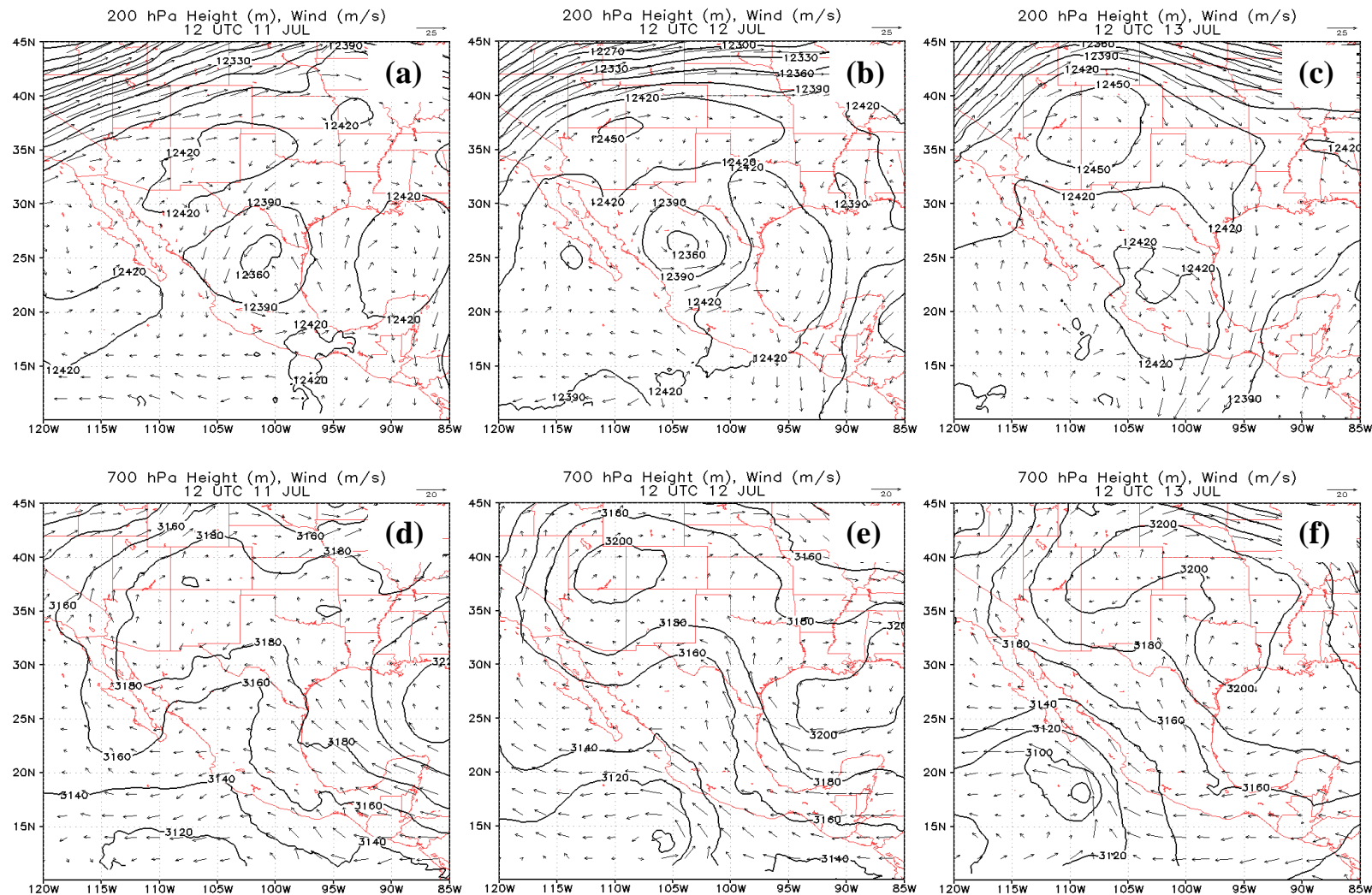


Figure 3.1. 200 hPa (a-c) and 700 hPa (d-f) height (black contours (m)) and wind vectors for 12 UTC 11 July, 12 UTC 12 July, and 12 UTC 13 July.

These features are all consistent with past research examining large-scale features of gulf surge events, and more notably strong surge events. Stensrud et al. (1997), Fuller and Stensrud (2000) and Douglas and Leal (2003) all relate gulf surge events with TEW or TS passage to the south of the GoC. Higgins and Shi (2005) show a statistical correlation between strong surges and TC passage within approximately 5° of Cabo San Lucas. Also, the low-level height and surface pressure field patterns fit very well with the evolution of the surge index developed in Bordoni and Stevens (2006).

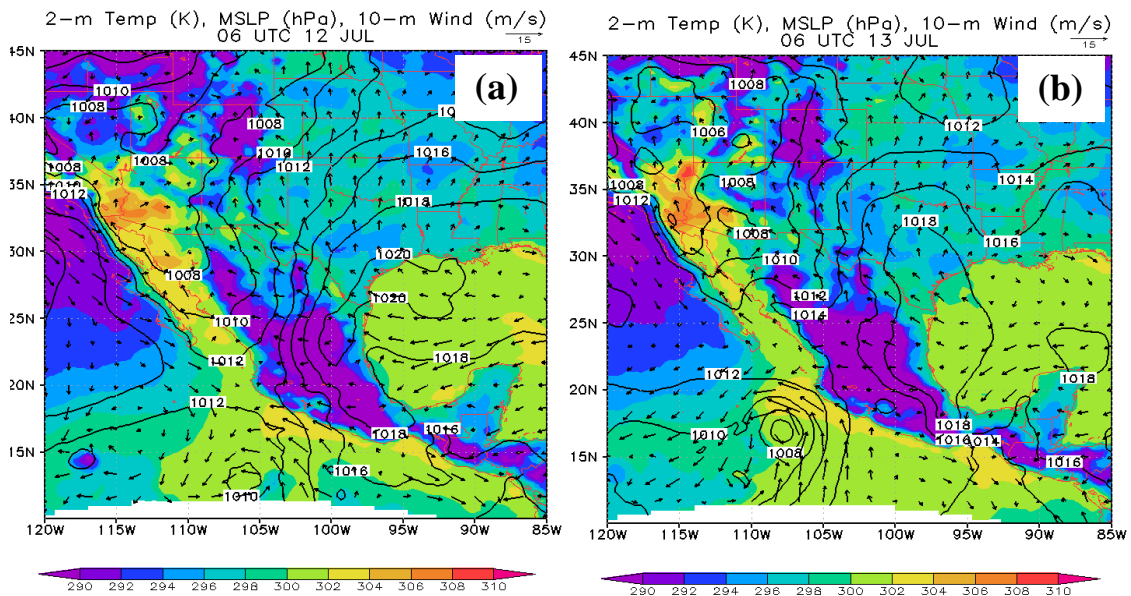


Figure 3.2. 2-m air temperature (shading (K)), 10-m wind vectors (black arrows) and MSLP (black contours (hPa)) at 06 UTC 12 and 13 July.

2. Subsynoptic overview

A brief overview of some mesoscale features relevant to this study will be given here. For a more in-depth analysis of the observed surge structure in its entirety, see RJ2007. Figure 3.3 displays satellite images from various times between 12 UTC 12 July and 12 UTC 13 July, while Figure 3.4 displays radar reflectivity images from the NAME radar network 2 km gridded data set. TS Blas can be seen in Figure 3.3 throughout the

six panels (a-f) as the area of cold cloud tops to the south of the GoC. The center of the TUTT is also visible as a small area of cloudiness near the Big Bend area of Texas (28-29°N, 100-105°W) in the first four panels of Figure 3.3 (a-d).

There are several convective features of note associated with the 12-13 July surge event. The first can be seen in Figure 3.3 and 3.4 (panels a-b) between 12-15 UTC 12 July. A convective complex developed near the mouth of the SMO between 06-09 UTC 12 July (not shown) and moved east-northeast into the radar domain coverage by around 09 UTC. By 12 UTC (Figs. 3.3a, 3.4a) the complex had a well-defined leading arc of convection and trailing stratiform region. The convective cluster also had a well defined cold pool that was observed in Mejia et al. (2010, see their Fig. 8) by the NOAA WP3. This convective cluster is also in the vicinity of a larger dome of cooler air over the mouth of the GoC on 12 July. It appears that this convective cluster may have initiated the northward movement of a portion of this cold dome as will be discussed in Chapter 4.

In Figs. 3.3 and 3.4 (c-d), convection is observed to be initiating over land along nearly the entire length of the SMO. By 00 UTC 13 July (Figure 3.3d) a convective cluster over the northern GoC is evident near 31°N, 113°W. This cluster produced weak convective outflow over the northern GoC (not shown). A stronger convective outflow passage was observed at PP just after 06 UTC, also associated with the convective cluster in Fig. 3.2d, which appears to have aided in the creation of the nighttime inversion layer. Finally, a larger convective cluster developed near the central gulf between 00 and 03 UTC 13 July, was near its greatest extent at 06 UTC 13 July (Fig. 3.3e, 29°N, 110°W) and dissipated by 12 UTC 13 July (Fig. 3.3f). The southern extent of this cluster is also visible in Fig. 3.3e. Note the extensive stratiform precipitation present north of 26°N in

Fig 3e. This large convective cluster produced extensive convective outflow that was likely involved in the initial surge event on 13 July.

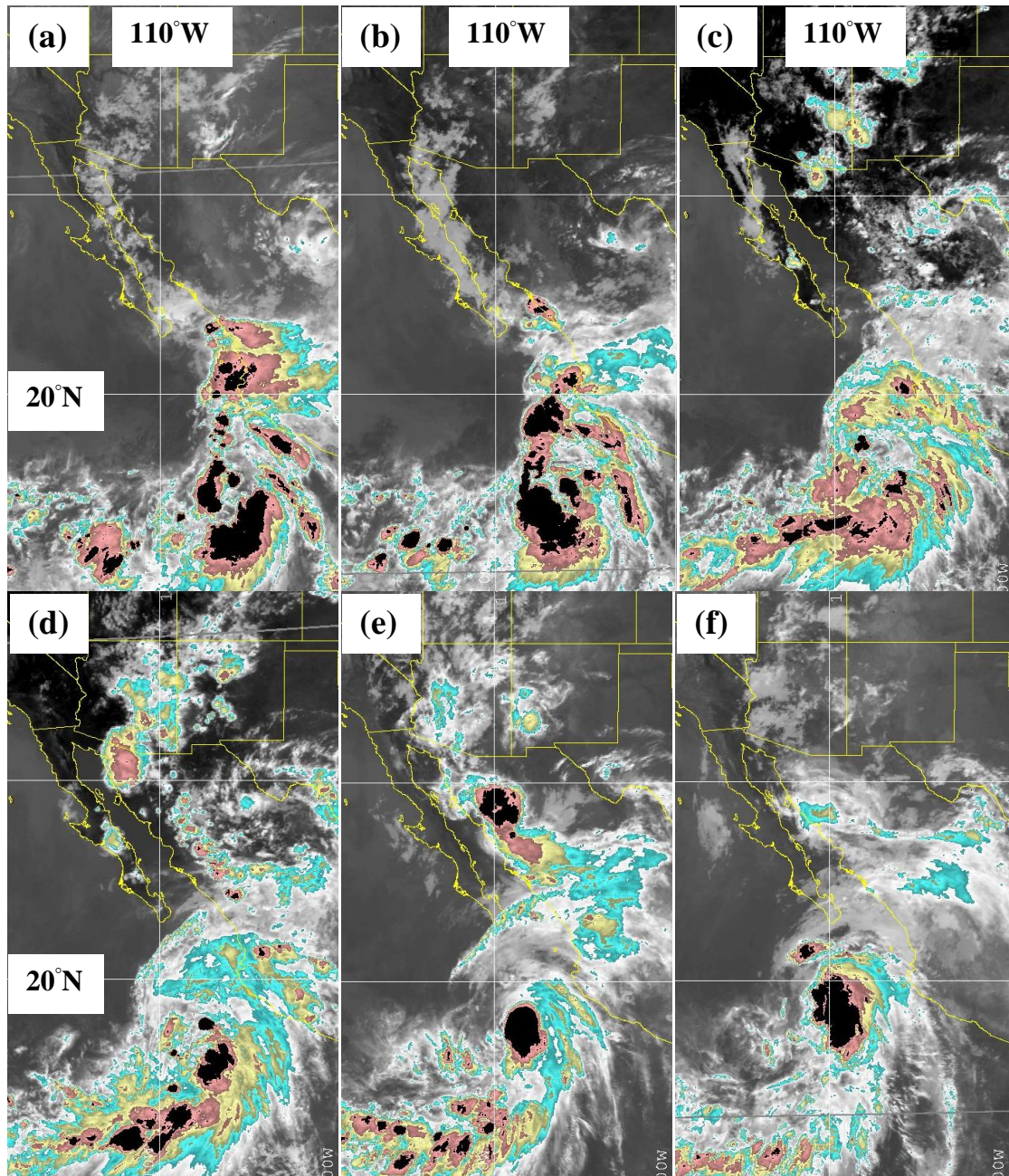


Figure 3.3. GOES infrared color enhanced brightness temperatures (K) over the core NAM region. (a) 12 UTC 12 July, (b) 15 UTC 12 July, (c) 21 UTC 12 July, (d) 00 UTC 13 July, (e) 06 UTC 13 July, (f) 12 UTC 13 July.

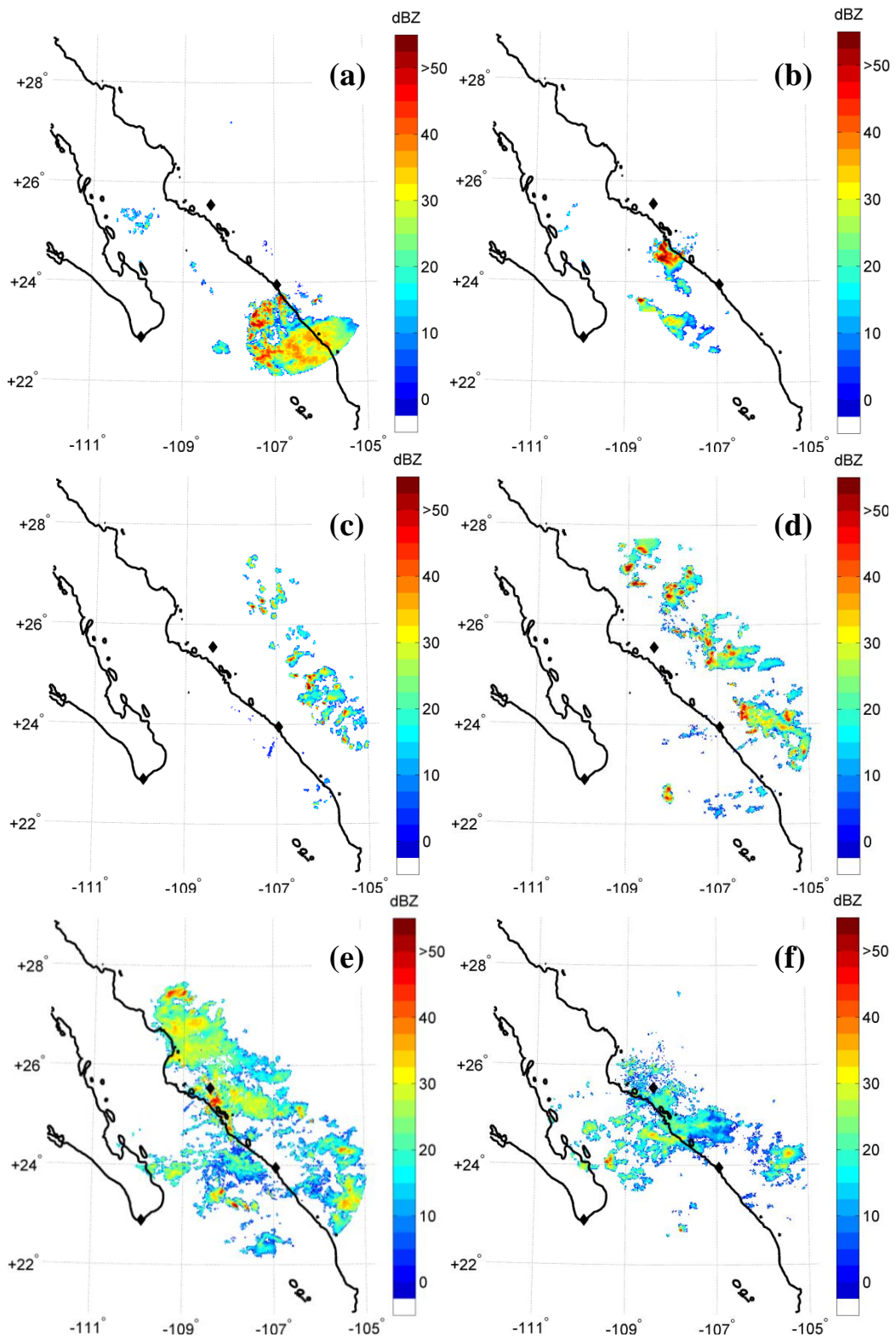


Figure 3.4. NAME radar reflectivity. (a) 12 UTC 12 July, (b) 15 UTC 12 July, (c) 21 UTC 12 July, (d) 00 UTC 13 July, (e) 06 UTC 13 July, (f) 12 UTC 13 July.

Figure 3.5 shows the vertical beam spectral width from the PP 915 MHz profiler, which can be used to help determine the extent and top of the mixing layer (Angevine et al. 1994). The creation of the inversion layer can be seen between 05-09 UTC by using the 1.5 m s^{-1} contour. During the convective outflow, there is higher turbulence (larger spectral width) from 05-07 UTC and the 1.5 m s^{-1} contour rises to near 930 m by 07

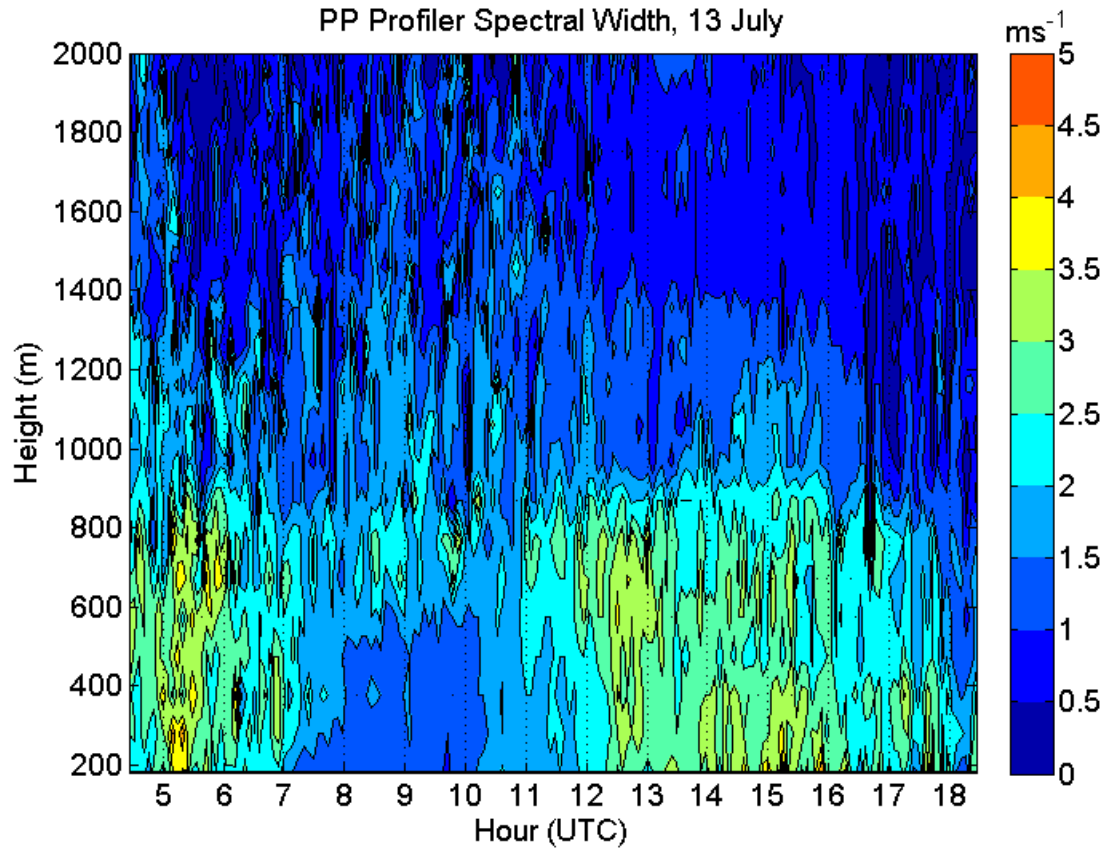


Figure 3.5. 915 MHz wind profiler time series of spectral width from PP.

UTC. After 07 UTC, elevated turbulence can still be seen between 700-1000 m, while there is relatively less turbulent air below 700 m as indicated by spectral widths less than 1.5 m s^{-1} . The onset of the initial surge can be seen after ~ 10 UTC in the increase in spectral width values.

3. Summary

There were multiple features associated with the 12-13 July 2004 surge event spanning a large range of scales. The larger-scale features included a TUTT moving near the SMO axis influencing mid and upper-tropospheric flow and possibly influencing the position of the upper-level monsoon ridge and convection along the SMO. TS Blas moved near the mouth of the GoC and an inverted trough associated with the pre-cursor TEW likely influenced convection on 12 July. Also an enhanced large scale pressure gradient along the GoC is present on 13 July associated with an anomalously strong heat low in the southwest US and higher pressures near the mouth of the GoC.

Several convective clusters formed along the SMO and over the GoC on 12-13 July. They seem to have influenced the surge event through their timing, placement and convective outflow. Of particular interest is a convective cluster on 12 July in the southern GoC that was associated with strong southerly flow along the southern and central GoC. Also a convective cluster in the central GoC produced extensive stratiform precipitation and convective outflow that is believed to be associated with the initial surge on 13 July as will be shown through the modeling studies contained herein.

CHAPTER IV

RESULTS AND DISCUSSION

1. Control simulation

a. Modeled and observed surge evolution

1) PRECURSOR CONVECTIVE DISTURBANCES NEAR MOUTH OF GULF OF CALIFORNIA, 12 JULY

After 18 hours of model spin up, the model generates mesoscale circulations and diurnal convection along the SMO as well as features associated with the TEW that will become TS Blas later on 12 July (National Hurricane Center Best Track, 2004). At 12 UTC 12 July the TUTT is located over central Mexico near 26.5°N , 104.5°W and tropical depression (TD) Blas is beginning to enter the domain along the southern edge near 106.5°W . Figure 4.1a shows the simulated 200 hPa heights and winds, while Figure 4.1b shows the simulated 700 hPa heights and winds. The simulated placement of the TUTT and TD Blas are very near those analyzed by the NARR (compare to Figure 3.1). The monsoon ridge can also be seen near 34°N over Arizona extending northward out of the domain, which is also in good agreement with the NARR. The 700 hPa trough extending northeast from TD Blas as seen in the NARR is present in a slightly weaker state in the simulation.

The convective cluster observed in the southern GoC at 12 UTC is present in the simulation, but has less extensive convection. Figure 4.2 shows derived radar reflectivity from the simulation (4.2a, 4.2c) and the observed radar reflectivity (4.2b, 4.2d) from the

NAME radar network at 12 and 15 UTC 12 July. The black ring in Figures 4.2b, 4.2d denotes the extent of the radar network, so any simulated reflectivity outside that ring will not be seen in the observations. The observed convective cluster has a well defined leading arc of convection and trailing stratiform region. Observations (Mejia et al. 2010) indicate that there is also a well developed cold pool associated with this cluster between 12-15 UTC. The simulated convection is not as well organized. At 12 UTC, the leading convection is more of a broken line with much less trailing stratiform precipitation. Examination of the model fields (Fig. 4.3) finds that the simulated cold pool is weaker than observed at 12 UTC. At 15 UTC (Fig. 4.2d) the simulation reproduces the small convective cluster near the coast and little trailing stratiform echo. The simulated convection is slightly slower than observed between 12-15 UTC (Figs. 4.2a,c), which would agree with a weaker simulated cold pool through most of the evolution of the

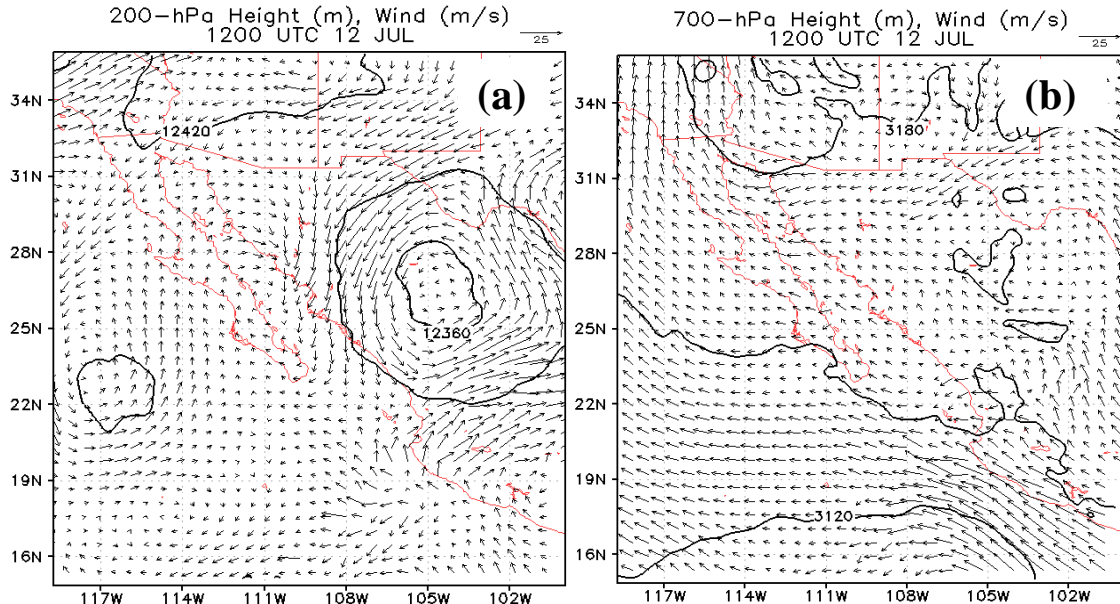


Figure 4.1. Height contours (m) and wind vectors at (a) 200 hPa and (b) 700 hPa at 12 UTC 12 July.

cluster. The slightly filled state of the simulated trough may be part of the cause of the weaker convection through weaker initial convection and a less favorable convective

environment. Also, resolution issues are likely partly responsible for the weaker convection.

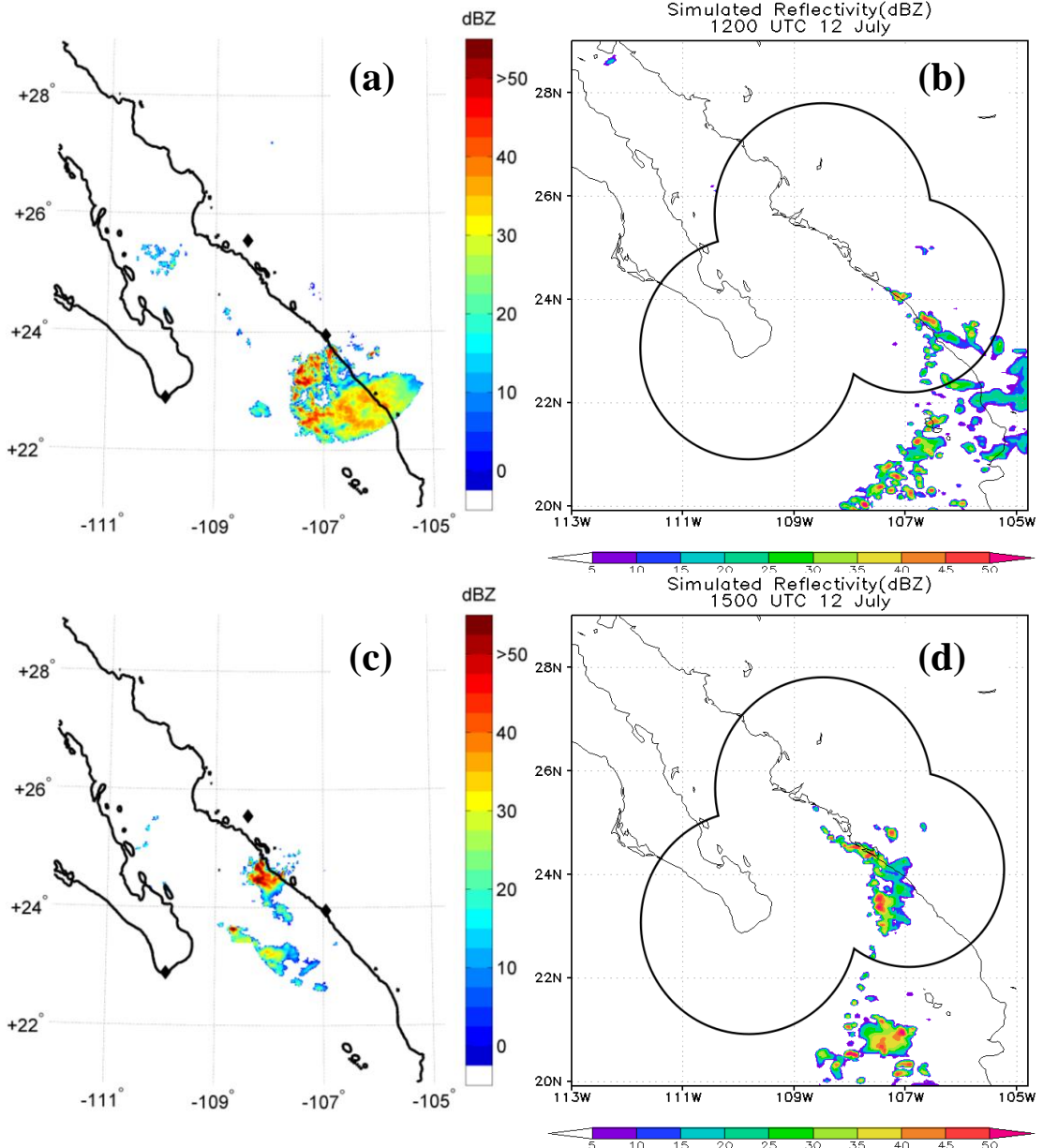


Figure 4.2. (a,c) Observed and (b,d) model derived radar reflectivity (dBZ) using the WRF post processor. (a) and (b) at 12 UTC 12 July, (c) and (d) at 15 UTC 12 July. Black diamonds in 4.2(a), (c) denote the three radar sites. Black ring in 4.2(b), (d) denotes the approximate maximum observable range of the radar network.

This convective cluster and its associated cold pool were sampled by the NOAA WD-P3 aircraft between 1300-1500 UTC 12 July (Mejia et al. 2010). Figure 4.3 displays

a cross-section (CS) of wind and potential temperature from the aircraft and the simulation. The simulated CS shown is along nearly the same line as observed (Figure 2.2 (AG1)), with the northern point being nearly identical, but the southern point being shifted about 80 km farther east (toward the coast) in response to the simulated convection placement (Figs. 4.2a,d). The simulated cold pool has a minimum potential temperature of around 299 K while the observed minimum is near 297 K. Also, the observed cold pool is slightly more moist, ~30 hPa deeper and is more intense. This cold pool is most likely a gravity current moving along the GoC as discussed in Mejia et al. (2010). It has features consistent to that of a gravity current: temperature decreases, wind speed increases and direction changes, and surface pressure increases with the passage of the cold pool (Simpson 1982; Haertel et al. 2001). Mejia et al. (2010) label the cold pool as structure 1 (S1) and that designation will be used herein as well.

Although the simulated cold pool is slightly weaker, it is still able to generate what appears to be a bore or solitary wave just ahead of the cold pool leading edge. This feature was observed and noted as structure 2 (S2) by Mejia et al. (2010) and this work. The potential temperature contours can be seen to slope upwards over S1 ahead of S1 by nearly 100 km in the simulation. Ahead of the feature (near 27.5 N in Fig. 4.3b) the 12 g kg⁻¹ mixing ratio line is near 925 hPa, and behind S2 it is located near 825 hPa. There is an increase in wind speed and a change in wind direction behind the leading edge of S2, along with no decrease in surface temperature and an increase in surface pressure (shown later), which is indicative of a bore or solitary wave passage (Simpson 1997; Knupp 2006).

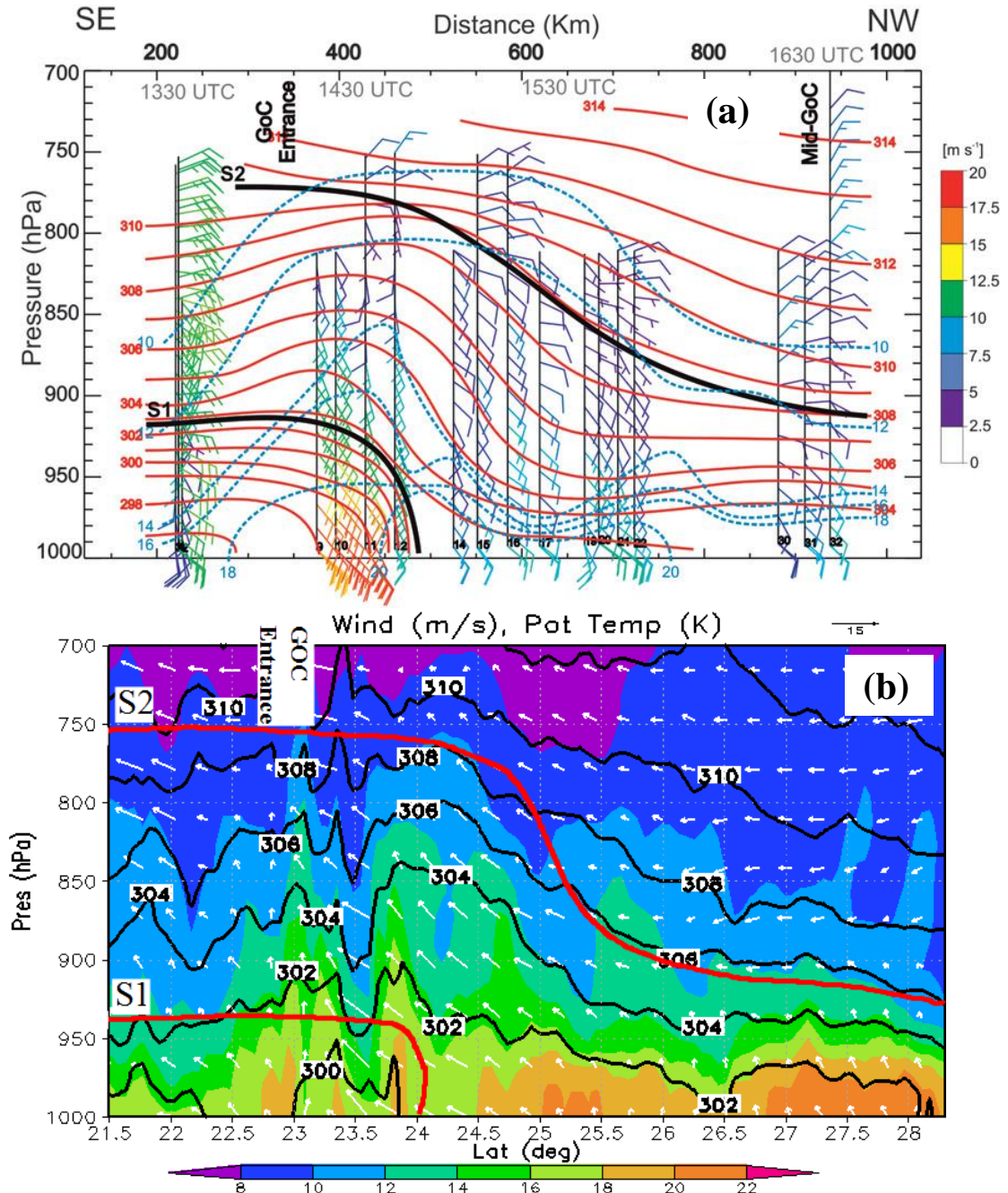


Figure 4.3. Along-gulf (AG1) cross section (CS) from NOAA WP-3D adapted from Mejia et al. (2010) (a) and from simulation (b). WP-3D CS runs from ~1300-1700 UTC, simulated CS taken at 1600 UTC. Potential temperature (orange lines) and mixing ratio (blue dashed line) contoured and wind barbs color coded by wind speed (a). Potential temperature (black lines) contoured and mixing ratio (shading) and wind vectors (arrows) are shown in (b). S1 denotes cold pool associated with convection near GoC entrance, S2 denotes a deeper disturbance discussed in Mejia et al. (2010). Black (a) and red (b) lines give general boundaries of S1 and S2.

Figure 4.4 shows the same CS as in Fig. 4.3b (AG1), except at 20 UTC 12 July, with the leading edge of S2 is now located near 26.5°N in the CS plane. At this time the amplitudes of the moisture and potential temperature perturbations have been reduced. The wind speed behind the leading edge has increased modestly and the direction has veered from southeast to south. The decrease in the definition of S2 from 16 to 20 UTC is most likely due to S1 dissipating by this time and S2 moving faster than S1 allowing it to outrun its forcing mechanism and slowly dissipate through turbulent mixing. S1 has dissipated by this time because the convection generating it dissipated by 18 UTC, leading to the modification of the cold pool through surface heat fluxes from the GoC. Further discussion of the propagation speed and dynamical classification of S2 is given later.

The propagating feature S2 is likely generated by S1 impinging on the mean state in the southern GoC. Johnson et al. (2007) use twice daily (00 and 12 UTC) sounding and NCEP reanalysis data to generate the atmospheric mean state during the NAME period. Their Fig. 12 shows that the mean state along the GoC is very similar to that of Figs. 4.3a or 4.3b, without the anomalous convection and a smaller slope to the isentropes along the leading edge of S2. That is to say the mean state, in the along the GoC sense, has a cold dome over the southern GoC with downward sloping isentropes toward the heat low over the desert southwest US. The marine layer inversion is present along the entirety of the GoC, which allows for propagating features, such as bores or solitary waves to form and propagate. A feature propagating along that mean state may lose amplitude with time due to the decrease in height of the isentropes as it moves northward, which would also explain the amplitude loss as S2 moves into the central GoC.

As S2 moves up the GoC, southeast to southerly flow, slight cooling and moistening through about 800 hPa occurs behind the leading edge. The feature loses definition and becomes washed out near Empalme around 2230 UTC 12 July in the simulation. Although it appears this feature is not the actual gulf surge signature, it is important because it ushers in a southerly flow regime throughout the southern and central GoC. It also begins to redistribute the cool air from near the mouth of the GoC northward. Figure 4.5 shows simulated and observed potential temperature and mixing ratio traces from the 1000 to 700 hPa at LM before and after the passage of S2. The simulation actually produces deeper cooling but moistening only through 750 hPa, and has the largest discrepancies in the boundary layer.

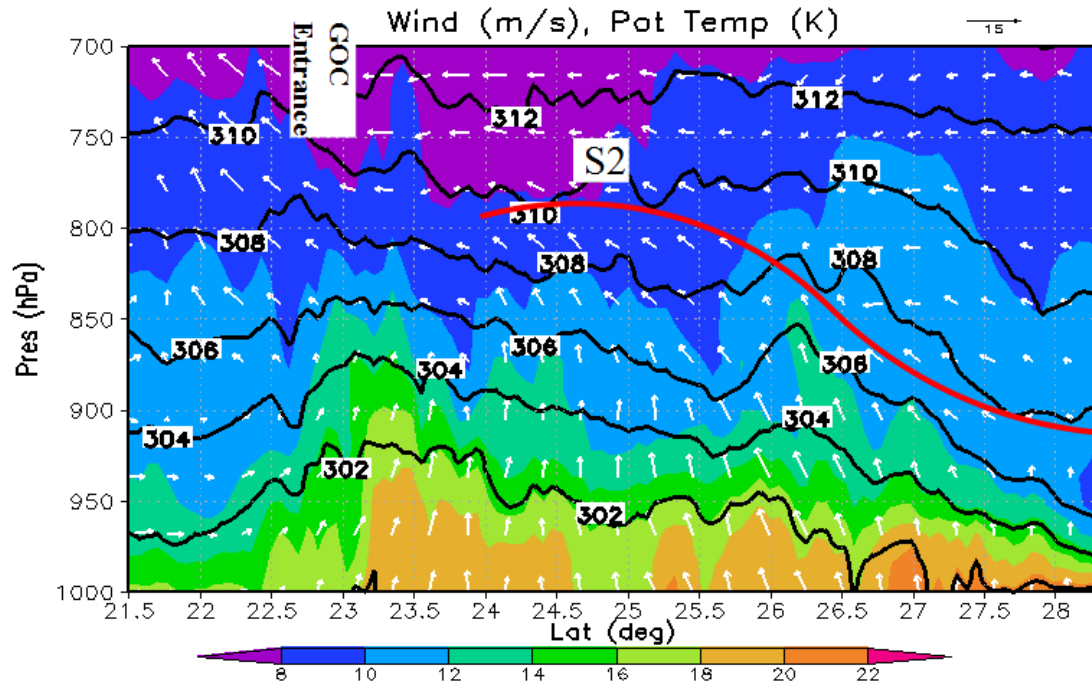


Figure 4.4. Same as Figure 4.3b except at 20 UTC 12 July. Red line marks general leading edge of S2.

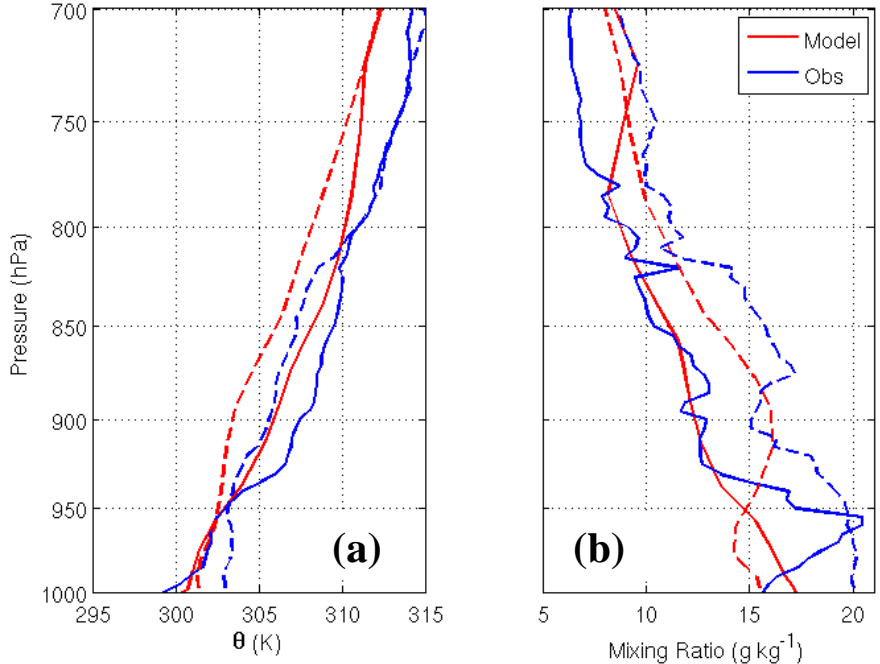


Figure 4.5. Potential temperature (K) (a) and mixing ratio (g kg^{-1}) (b) at Los Mochis at 12 (solid) and 18 (dashed) UTC 12 July. The 12 UTC sounding occurred before the passage of S2 and the 18 UTC sounding after.

Sea-breeze/mountain solenoidal circulations begin to form shortly after sunrise along the GoC coastal plain and show a marked intensification after 19 UTC 12 July with the wind veering from southerly to southwesterly along nearly the entirety of the SMO by 20 UTC (Fig. 4.6a,b). The first afternoon echo along the SMO occurs in the simulation around 1630 UTC near SPOL and over the highest peaks and ridges in the northern SMO (Fig. 4.7), which nearly corresponds with the first observed echo near SPOL (~1645-1700 UTC). This early simulated convection is strongly tied to several protruding ridges along the SMO that may focus low-level convergence and upward velocities. Lang et al. (2007) show a very strong correlation between first echo and echo frequency and topographic features along the SMO as well.

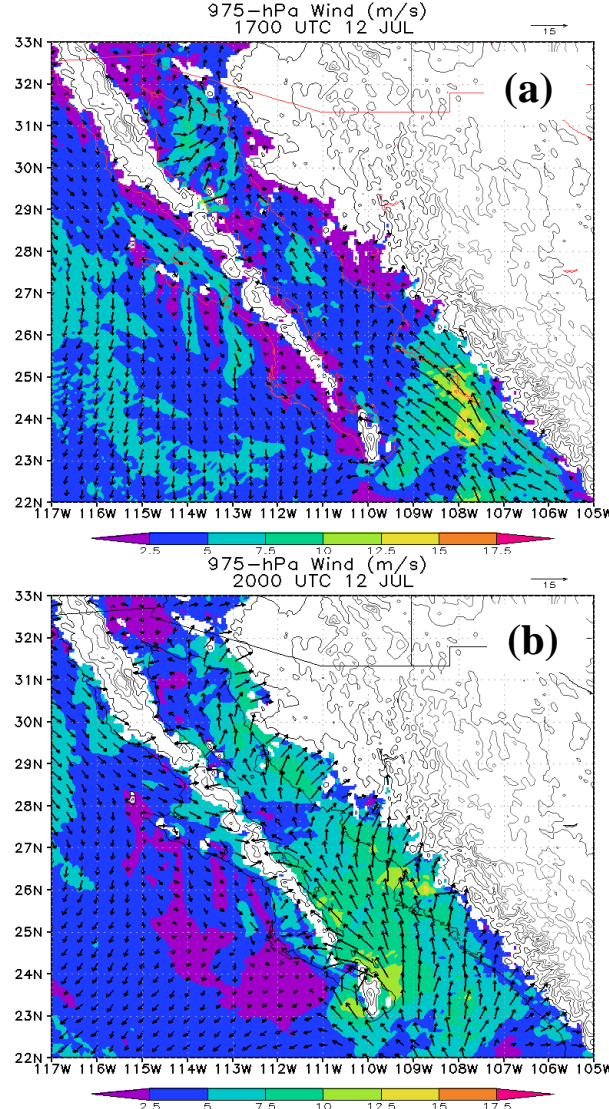


Figure 4.6. 975 hPa simulated wind magnitude (shading (m s^{-1})) and vectors (arrows) at 17 (a) and 20 (b) UTC 12 July. Areas in white are above the 975 hPa elevation level, while the thick black to light gray contours denote 500 m, 1000 m, 1500 m, 2000 m and 2500 m elevations respectively.

Over the next several hours convection gradually intensifies along the SMO with convection beginning to form small clusters and cold pools. Figure 4.8a,b display the first model level potential temperature and the 20 and 40 dBZ reflectivity contours at 20 and 2230 UTC 12 July. Convection readily moves off of the SMO in the northern and central GoC while it moves more parallel to the SMO in the southern GoC. This is due to the 700-400 hPa flow (not shown) being nearly perpendicular to the SMO in the northern

and central SMO, while it is nearly parallel to the SMO in the southern region (Finch and Johnson 2010). The convection forms several small clusters with well defined cold pools

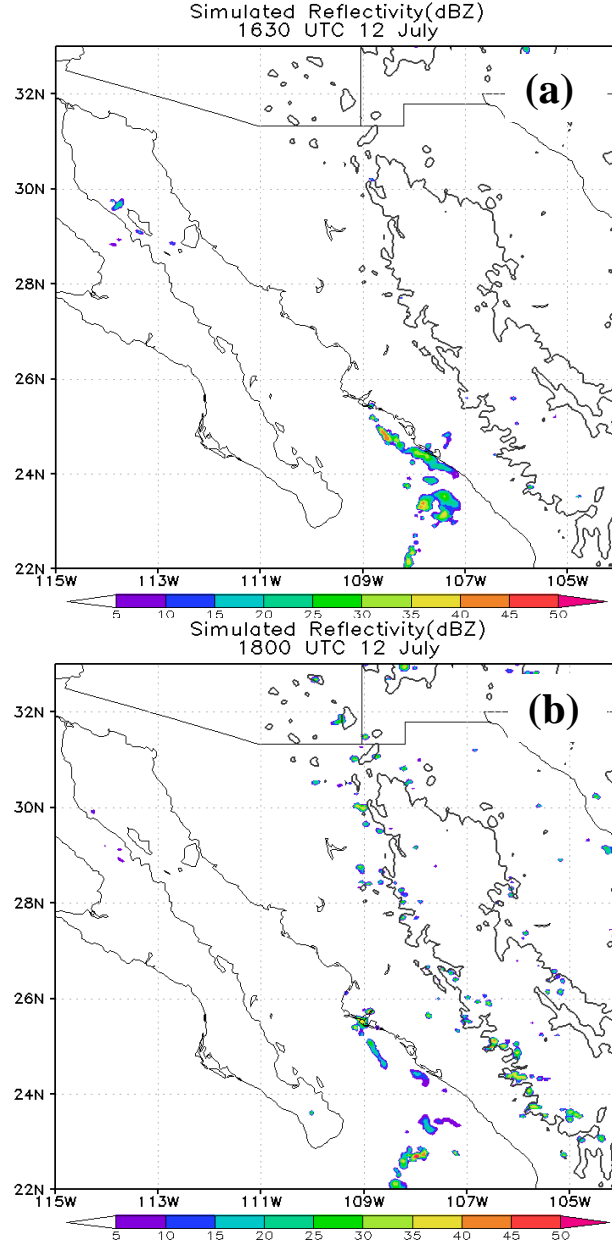


Figure 4.7. Simulated radar reflectivity factor (dBZ) at 1630 (a) and 1800 (b) UTC 12 July. The thick black contour denotes 1750 m.

in the northern and central GoC by 2230 UTC while the southern GoC convection is still more cellular in nature with less defined structure. This agrees with the findings of Finch

and Johnson (2010) which argue that the more perpendicular the 700-400 hPa flow is to the SMO, the more organized and farther away from the SMO convection will propagate.

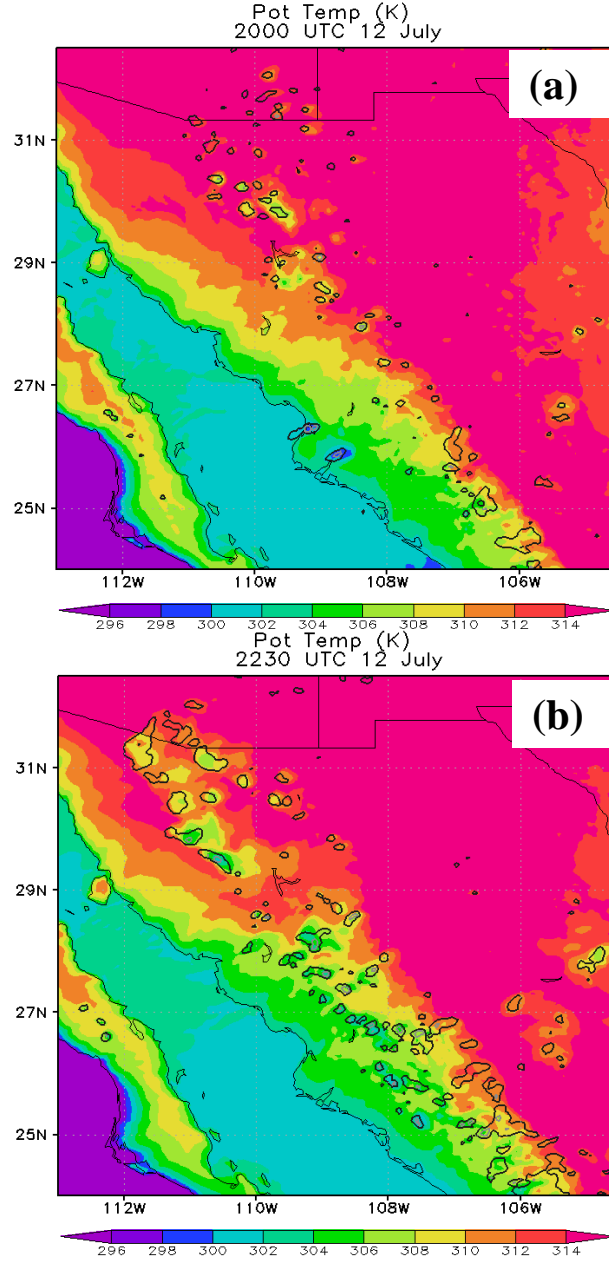


Figure 4.8. First model level (~40 m AGL) potential temperature (shading (K)) and radar reflectivity factor at 20 and 40 dBZ (thick black and gray contours respectively) at 20 (a) and 2230 (b) UTC 12 July.

2) DEVELOPMENT OF MATURE SURGE, 13 JULY

Figure 4.9 displays the 200 and 700 hPa heights and wind vectors at 00 UTC 13 July. Between 12 UTC 12 July and 00 UTC 13 July the TUTT moved nearly due west to a position centered near 27°N , 107.5°W . The 200 hPa heights have also risen at least 30 m near the center of the TUTT. The observed TUTT is centered near 28°N , 107°W with similar heights to that simulated. TS Blas is now nearly fully into the simulation domain with higher wind speeds to the northwest of the center of circulation and is centered near 15.5°N , 108°W in the simulation (Fig 4.9b). Observed TD Blas intensified into TS Blas by 18 UTC 12 July with the center of circulation near 16.4°N , 108°W . The simulation places the center of Blas around 100 km farther south than observed. This is most likely due to Blas riding the boundary of the domain and being subjected to smoothing and damping along the lateral boundaries of the domain.

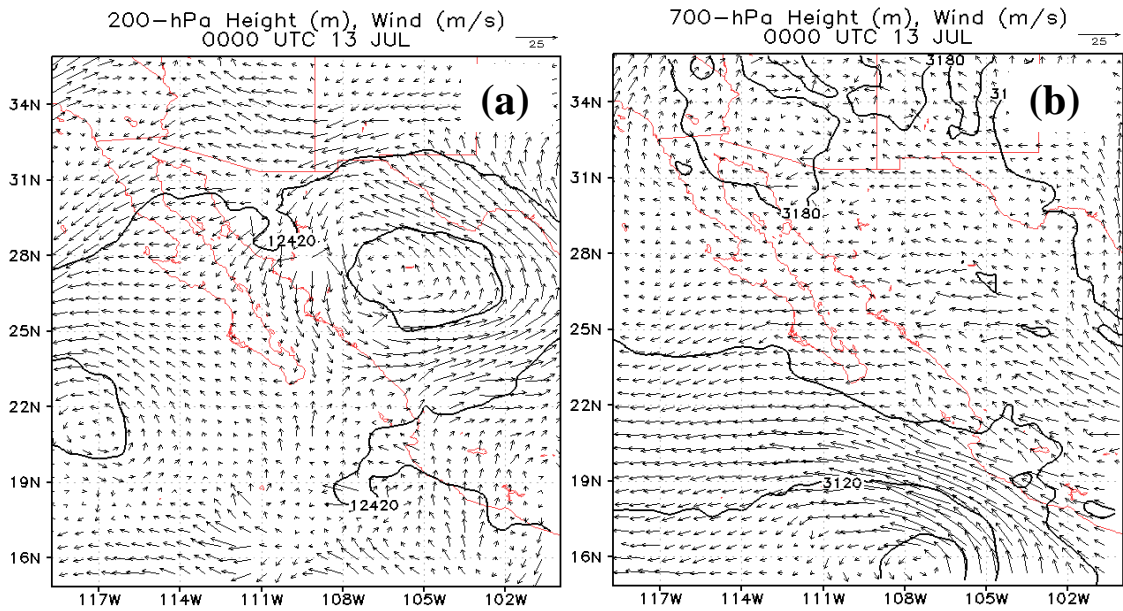


Figure 4.9. Same as Figure 4.1 except for 00 UTC 13 July.

Figure 4.10 displays simulated and observed radar reflectivity (same as Fig. 4.2) for 0030 and 0600 UTC 13 July. By 0030 UTC, the simulated convection (Fig 4.10b) in

the southern GoC has begun to organize into several clusters and move off the SMO slightly. The observed and simulated convective clusters are in very similar locations at 0030 UTC (Fig 4.10a), however there is less simulated convection between 25-28°N than

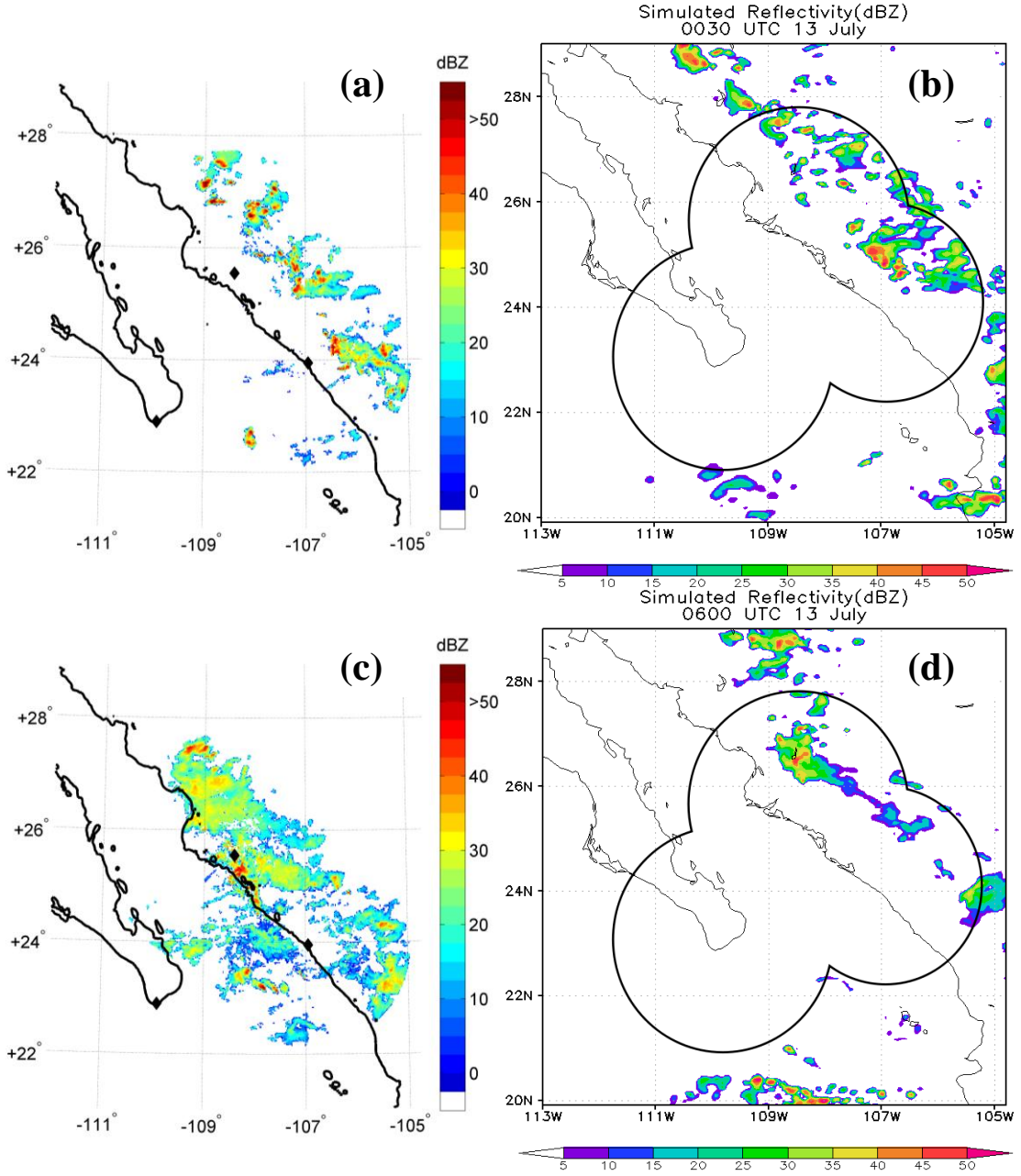


Figure 4.10. Same as Figure 4.2 except for 0030 UTC and 0600 UTC 13 July.

observed. Again, the simulation produces less convection and stratiform precipitation at 06 UTC than observed (Figs. 4.10c,d). The simulated convection also does not progress

to the coastline as observed. This may be related to slight differences in the cloud-bearing layer winds (800-300 hPa), or incorrect cold pool evolution & resolution in the simulation. Also, the simulation progresses through the stages of convective evolution faster than the observed convection. As an example, the simulated convective cluster near 24°N dissipates by 03 UTC, while the observed cluster is active until ~06 UTC and moves west-northwest to near 26°N and the coastline (Fig. 4.10c). An increased evolution rate is found in the northern GoC convection as well.

Simulated brightness temperatures at 00 and 12 UTC are shown in Fig. 4.11. Comparisons to Fig. 3.2 and other GOES images (not shown) highlight that convection is much more extensive along the entire SMO in the simulation than in observations at 00 UTC and the maturing convective cluster present in the simulation at 00 UTC near 29°N, does not develop in reality until after 01 UTC. By 12 UTC nearly all residual convective cloud cover has dissipated in the simulation, while there is still extensive cloud cover present in reality. Li et al. (2008) show similar results for a 3 km

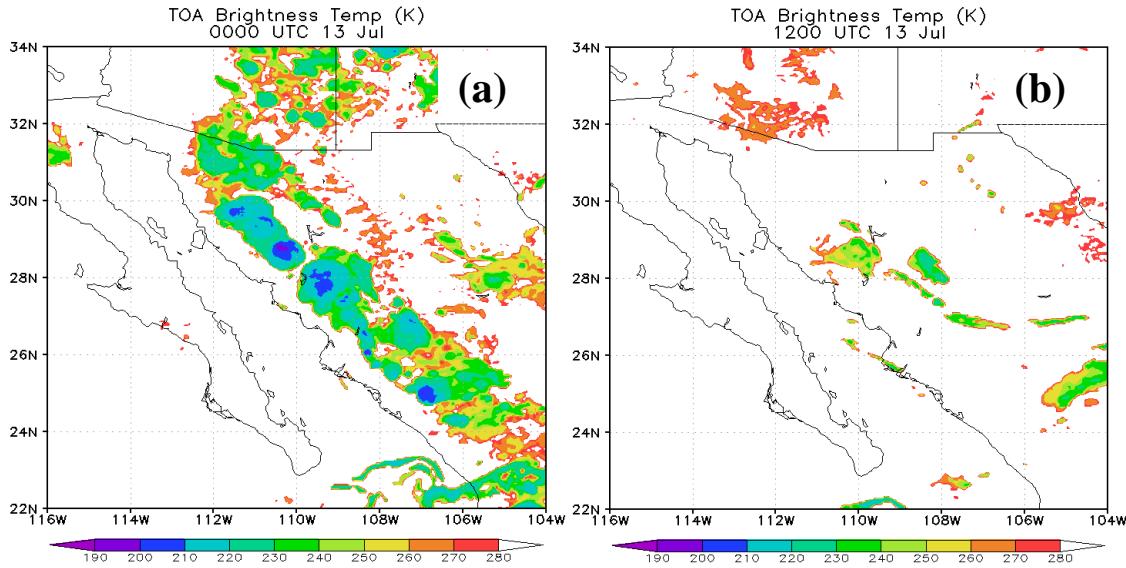


Figure 4.11. Simulated top of the atmosphere (TOA) brightness temperatures (K) for 00 (a) and 12 UTC (b) 13 July.

simulation over the same region. They show the model overestimates precipitation during the 18-06 UTC timeframe and underestimates it from 06-12 UTC, which indicates that the initiation and evolution of precipitation occurs too fast in the model. The reduced amount of convection and stratiform precipitation as well as the increased rate of evolution in this study are important factors when examining the simulated surge evolution.

The simulated surge appears to initiate in the southern GoC between 01-04 UTC 13 July. The 950 hPa moisture flux is a useful field to track the surge and is shown in Fig. 4.12 at 04, 08, 12, and 16 UTC 13 July. At 04 UTC (Fig. 4.12a) one can see an area of enhanced moisture flux between 24.5 and 26.5°N. This area of enhanced moisture flux is the initial surge signal beginning to propagate up the GoC. At this time convective outflow over the southern GoC is just beginning to consolidate along the coastline and move out over the GoC. The simulated surge is initiated by an increase in the flux of cool moist air from near the GoC entrance as well as cold, less moist air from the west side of the peninsula through the large gap in the southern portion of the Peninsular Ranges between 23.5 and 25.5°N along with the initial input of convective outflow near LM. Evidence of smaller gap flows from the Pacific Ocean into the GoC can be seen along nearly the entire length of the Baja Peninsula. The elevated moisture flux in Arizona and near PP is associated with convective outflow from the convection in the northern GoC.

By 08 UTC (Fig. 4.12b) the surge front has propagated north to somewhere near 27.5°N. At this point, convective outflow has been impinging on the GoC along the coastline from 27 to 29°N for about three hours, complicating the interpretation of where

the initial surge front is located. The convective outflow significantly strengthens the

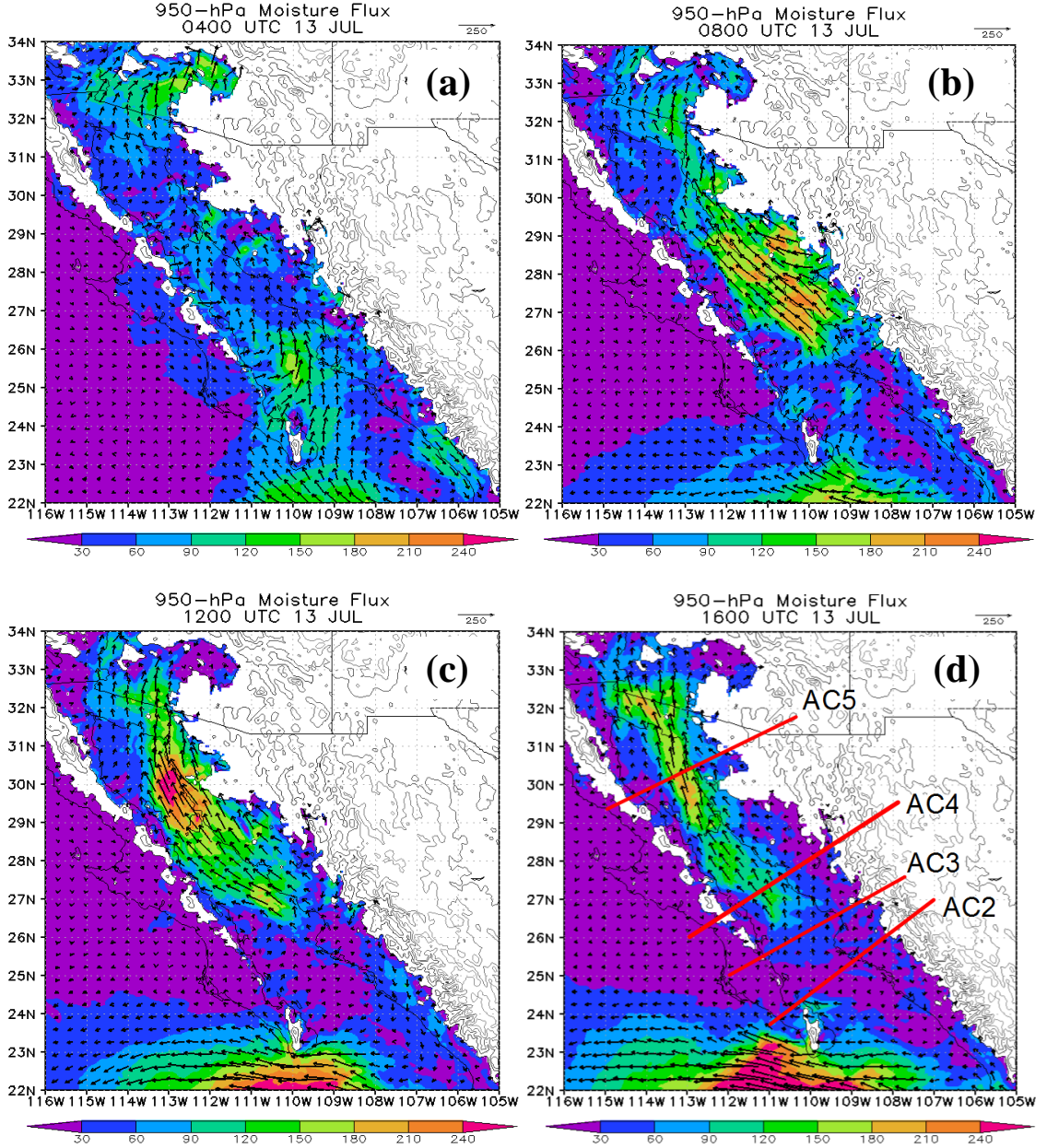


Figure 4.12. 950 hPa moisture flux ($\text{g m kg}^{-1} \text{s}^{-1}$) at 04, 08, 12, 16 UTC 13 July. Red lines marked AC2-5 give the locations of four across the gulf cross sections used in later analysis.

surge as can be seen by the large increase in moisture flux values greater than $150 \text{ g m kg}^{-1} \text{s}^{-1}$ between 04 and 08 UTC. The initial surge feature and convective outflow have merged and become indistinguishable at this point. Further complicating matters is the

GoC LLJ. The GoC LLJ begins to strengthen significantly between 04-09 UTC (Anderson et al. 2001; Douglas et al. 1998) at PP, which may be manifesting itself as the thin line of enhanced moisture flux along the east coast of the GoC at 08 UTC running ahead of the surge. Another convective outflow passed PP around 06 UTC, which may also be adding to the enhanced moisture flux north of the GoC.

At 12 UTC (Fig. 4.12c), the consolidated surge has reached the northern GoC. The leading edge of the wind maximum is slightly ahead of the moisture flux maximum. Figure 4.15c shows that wind speeds greater than 12.5 m s^{-1} reach PP around 12 UTC while the moisture flux maximum is still $\sim 100 \text{ km}$ south. The lag in maximum moisture flux at PP is also observed (RJ2007). By 16 UTC the surge has entered southern Arizona and begun to spread out over the widening coastal plain. Following the leading edge of the intense moisture flux up the GoC between 04 and 14 UTC (after 14 UTC, the surge front becomes too diffuse in Arizona), gives a distance of about 800 km in 10 hours, or an average total system speed (intrinsic phase speed plus background flow) of $\sim 22 \text{ m s}^{-1} \pm 1 \text{ m s}^{-1}$. Table 4.1 displays the total system speed for the surge broken down into two segments. The first is for the time period after the surge feature begins propagating up the GoC, ~ 04 UTC through about 10 UTC; the second is for the surge as it enters the northern GoC and begins to experience the coastline and wider coastal plain. Note that these speeds are total speeds; they do not have the mean flow removed. The observed surge is estimated to move at an average total speed of $\sim 17 \text{ m s}^{-1}$ in the southern GoC and $\sim 22 \text{ m s}^{-1}$ in the northern GoC (RJ2007), which indicates the model surge may move slightly faster than observed, especially in the southern and central GoC.

Table 4.1. Total speed of the intense moisture flux associated with the leading surge impulse on 13 July. Uncertainty estimates are based on position ambiguities using moisture flux to track the surge.

	04-10 UTC	10-14 UTC	04-14 UTC
Surge Total Speed	$23 \pm 1 \text{ m s}^{-1}$	$21 \pm 1.5 \text{ m s}^{-1}$	$22 \pm 1 \text{ m s}^{-1}$

Shortly after the observed surge wind maximum reached PP, the WP-3D made an across the gulf transect, along the line AC1 in Fig. 2.2. Figure 4.13a displays the observed wind vectors, while Fig 4.13b shows the potential temperature and Fig. 4.13c gives the modeled wind vectors and potential temperature. A maximum in observed wind speed just over 20 m s^{-1} near 970 hPa is seen over the east-central GoC. The 10 m s^{-1} wind contour extends upward to $\sim 890 \text{ hPa}$, westward to the Baja, and eastward over the coastal plain. There is also a band of greater than 7.5 m s^{-1} southerly winds extending over the ridge along the eastern side of the CS around 900 to 870 hPa. The simulated surge is less intense and slightly shallower than observed; it has a maximum wind speed of around 15 m s^{-1} at 975 hPa in the east-central GoC. However the structure of the surge is very similar to that observed with greater than 7.5 m s^{-1} southerly winds extending above the ridge to the east and nearly to the Baja Peninsula in the west. The observed and modeled surges have a similar potential temperature structure as well; with the simulation being cooler over the eastern landmass due to it being three hours earlier (14 UTC is near sunrise). The simulated surge CS is taken about 3 hours earlier than observed in this case, at the same time in the surge evolution, which again indicates the evolution of the modeled surge is too fast.

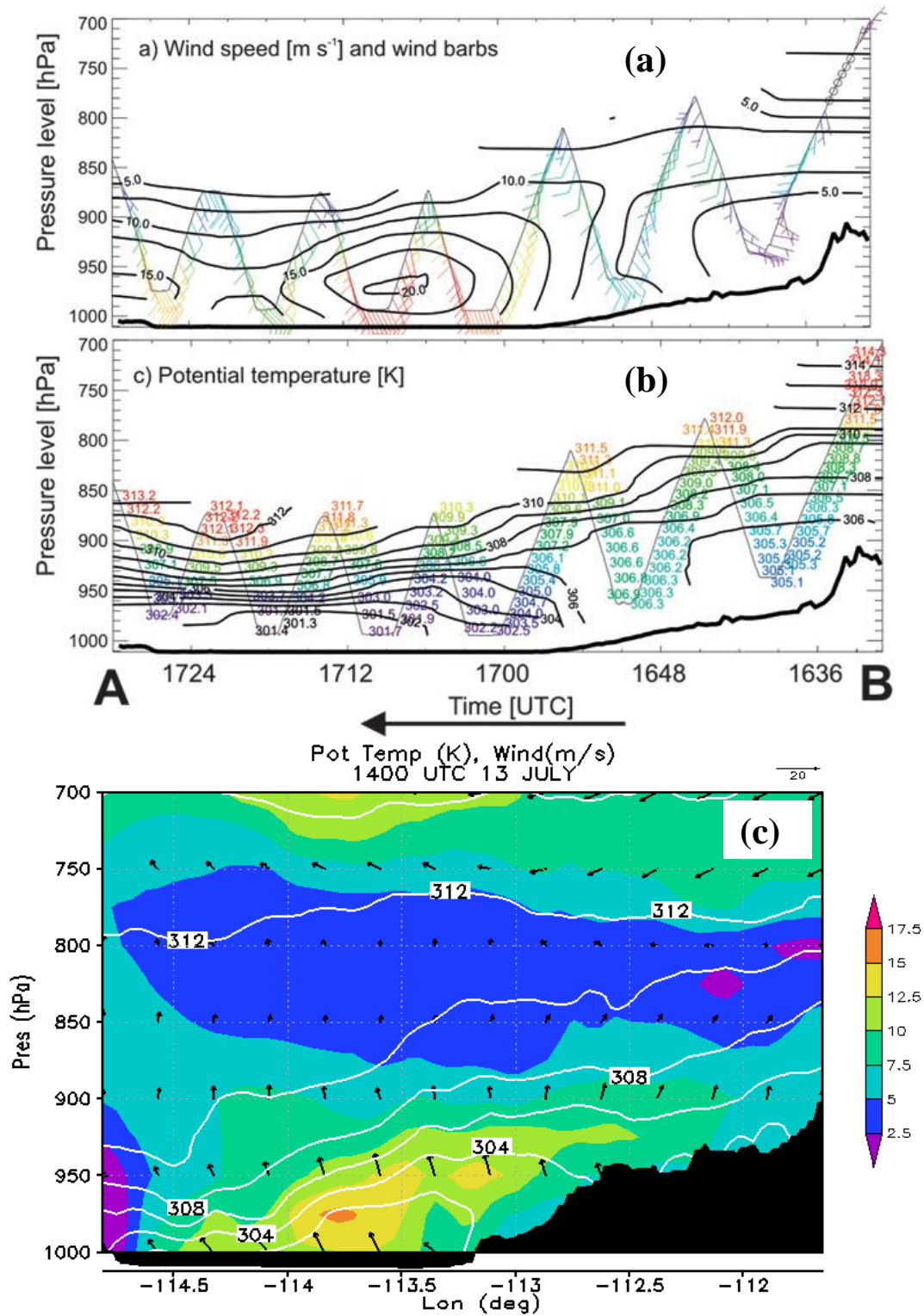


Figure 4.13. The observed wind speeds (contours (m s^{-1})) and barbs (color coded by speed) are in (a), potential temperature (contours (K)) in (b) and modeled wind speed (shading (m s^{-1})), direction (arrows) and potential temperature (contours (K)) in (c). The black shading in (b) indicates topography. All panels are along across-gulf cross section (AC1).

Figures 4.14a and 4.15a display surface traces of temperature, dew point, and mean sea level pressure (MSLP) for KB and PP. Figures 4.14b-c and 4.15b-c show the observed and modeled wind profile respectively, from 200 m to 2 km. The general diurnal cycle of 2 m temperature and pressure is recreated well, with 2 m dew point showing less correlation. There is a bias in MSLP of 0.3 hPa and -0.1 K in temperature at KB. In regards to features of the surge, the simulation reproduces the initial pressure rise around 00-02 UTC 13 July, which may have been a weak convective outflow passage. The model produces too steep of a temperature decline and a slightly stronger outflow. As the initial surge feature passes KB, the model produces slightly too much surface cooling and pressure rises slightly earlier than observed, around 04 UTC rather than 05-06 UTC. The pattern of an initial pressure jump followed by a brief plateau in the simulation (04-10 UTC) is observed (0530-12 UTC); however the second significant pressure rise that is observed is not recreated. It appears this second pressure rise may be related to the decaying convective complex very near KB between 09-12 UTC that is not simulated. The elevated nighttime temperatures observed before 12 UTC and the excess cooling from the simulation could also be explained by excessive radiational cooling in the model due to lack of cloud cover. The wind field of the modeled surge is too shallow by nearly 1000 m using the 10 m s^{-1} contour, less intense than observed with maximum winds $> 20 \text{ m s}^{-1}$ observed and only $> 12.5 \text{ m s}^{-1}$ simulated, but has nearly correct timing.

At PP, the 2 m temperature and MSLP diurnal cycle is represented well, with two notable dry air intrusions on 12 July seen in the dew point trace (Fig 4.15a). This can be related back to excessive inflow of cool, dry air from the Pacific Ocean in the NARR

boundary conditions (Ciesielski and Johnson 2008)². There is an MSLP bias of 2.2 hPa and a temperature bias of -0.6 K at PP. The weak convective outflow passage observed around 00 UTC is replicated in the simulation by one stronger gust front around 02 UTC. There is evidence that the second convective outflow passage over PP may be an atmospheric bore (RJ2007) and the modeled convective outflow passage at 07 UTC may be a bore as well. The leading edge of the strong winds associated with the surge is timed well at PP (Fig 4.15b-c), about 1 h early, but again the surge is too shallow by nearly 1000 m and less intense with the maximum wind magnitude around 7-9 m s⁻¹ too small. It has been shown that the QNSE has a cool and moist bias of 1-2 K in the 2 m temperature and dew point over the US, especially in the late afternoon and evening (Wolff et al. 2011), which would explain the cool bias at KB and PP and the relatively good performance in dew point temperature. The NARR has a dry bias of -1.9 g kg⁻¹ at the surface (about -1.5 K dew point bias at a dew point of 298 K, MSLP of 1008 hPa) (Ciesielski and Johnson 2008), while the KB and PP surface traces have dew point biases of -0.3 K and 0.1 K (disregarding dry air intrusions from Pacific Ocean on 12 July) respectively.

Many of the differences between the observed and simulated surge depth are likely related to the QNSE boundary layer scheme and other model deficiencies. A test run using the Yonsei University (YSU) planetary boundary layer scheme was performed as well. This run did produce slightly warmer surface temperatures and a deeper surge feature. However, the simulated surge feature was deemed to be too gravity current-like and its features did not match those observed as well as the QNSE run. This shows some

² Ciesielski and Johnson (2008) show the NARR has an excessively strong GoC LLJ, which is related to strong flow from the Pacific Ocean into the northern GoC. This will show up in this simulations in the initial and boundary conditions.

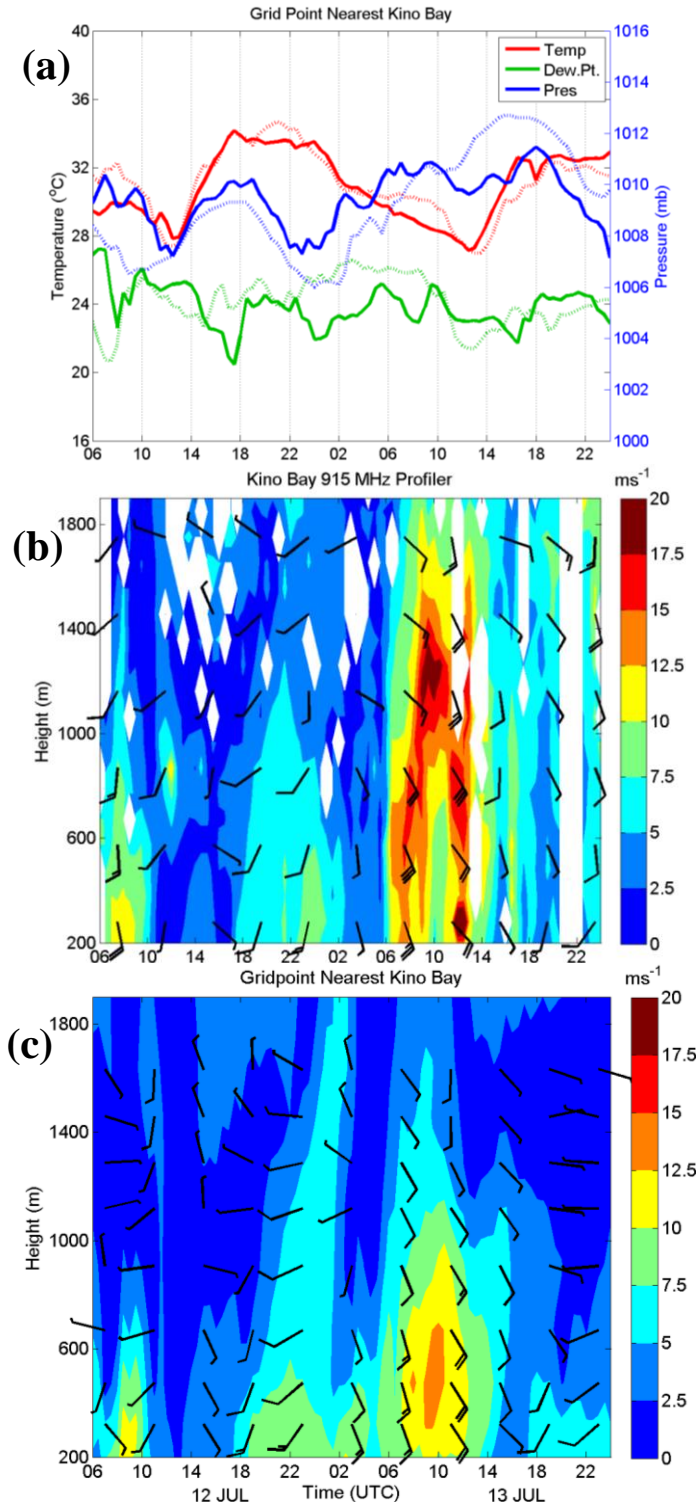


Figure 4.14. Time series of surface temperature ($^{\circ}\text{C}$), dew point ($^{\circ}\text{C}$), and MSLP (hPa) at Kino Bay for the simulation (solid) and observations (dashed) (a), and the observed (b) and simulated (c) wind profile time series from 06 UTC 12 July to 00 UTC 14 July. Barbs in (b) and (c) indicate speed with full barb equal to 5 m s^{-1} and half barb equal to 2.5 m s^{-1}

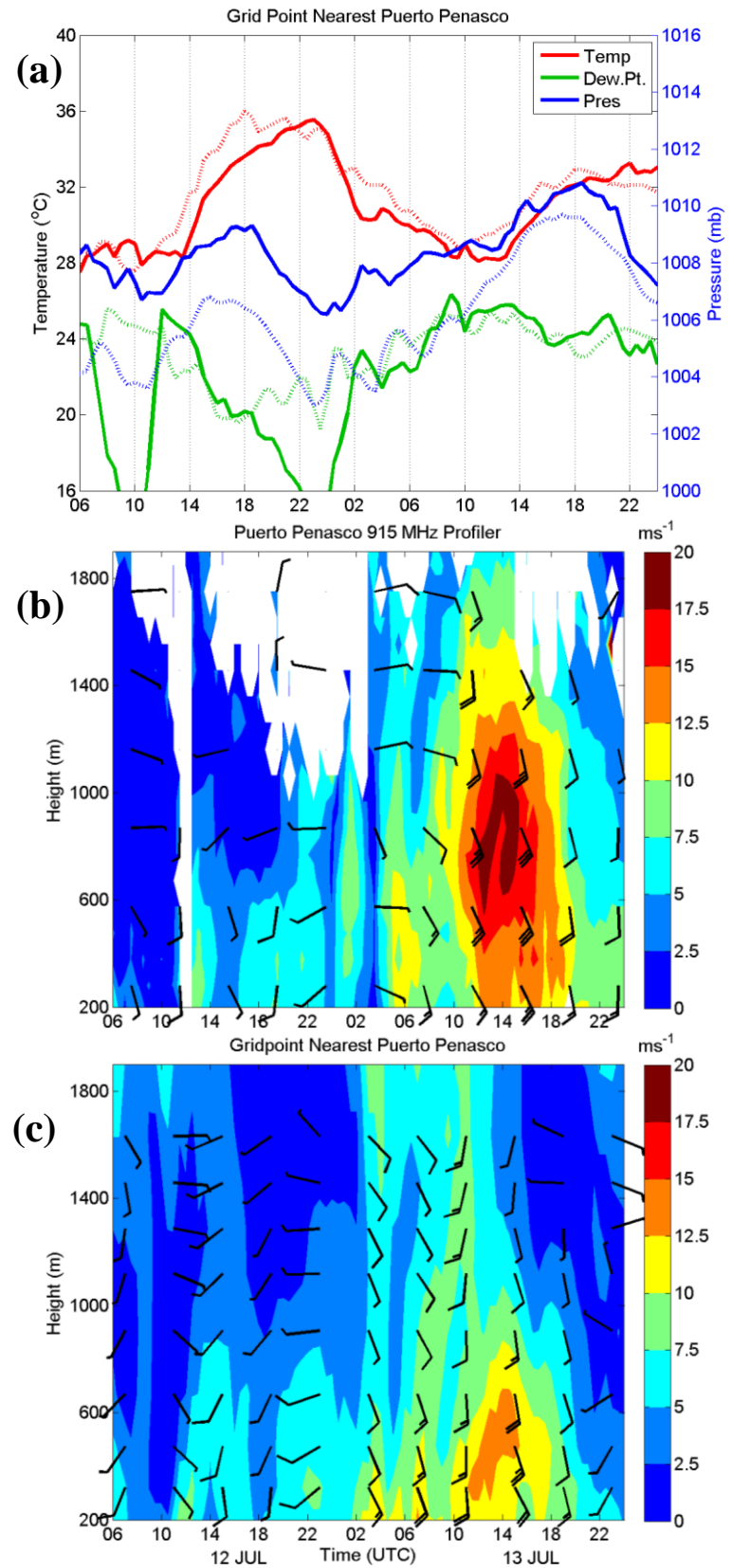


Figure 4.15. Same as Figure 4.14 except for Puerto Penasco.

of the sensitivity of the modeled surge to parameterization choices. Misrepresentation of vegetation type and a corresponding error in the roughness length may also contribute to the shallow simulated surge, especially at PP. Significant changes in vegetation occur during the NAM, as precipitation induces green-up and growth of the local vegetation (Watts et al. 2007) and impacts winds in the region (Douglas et al. 2006; Ciesielski and Johnson 2008). This study used static United States Geological Survey (USGS) land surface and vegetation maps, which may have significant differences to the actual vegetation during the simulation period.

Finally, the weaker convection, reduction of stratiform precipitation, and faster precipitation feature evolution may be the biggest reason for a shallow and weak simulated surge. As highlighted above (Figs. 4.2 and 4.3), the simulation produces weaker convection and less stratiform precipitation in the convective cluster related to S1 and S2. Correspondingly, S1 is shallower and less intense than observed and possibly the propagating portion of S2 is as well. On late 12 into 13 July, the simulated convective clusters along the SMO are slightly less intense, have less stratiform rain and evolve too fast (Figs. 4.10-4.13). This would produce weaker convective outflow and cold pools just on the basis of less duration of precipitation evaporating into the sub-cloud layer. As it has been shown, the initial surge is related to convective outflow in the southern and central GoC. If this outflow is weaker than observed it would be expected that the surge will be weaker as well.

3) EVOLUTION SUMMARY

This simulation seems to capture the evolution of the surge quite well. Stensrud et al. (1997) conclude that convection along the southern SMO is integral for gulf surge evolution. They also show that a surge event will evolve without diabatic effects from convection, although in a modified form that evolves more slowly in time. This case is very similar to those results. The surge appears to initiate before the influence of convective outflow reaches the GoC and suggests the surge would evolve without convection like Stensrud et al. (1997) show, but at a slower and possibly weaker pace in this case. When the convective outflow impinges on the GoC, the initial surge consolidates and intensifies. It begins to slow down again as it enters the very northern extent of the GoC, which is very similar to the results of Stensrud et al. (1997).

Also, the simulation performs qualitatively very well when compared to observations. All important observed features are recreated in the simulation with reasonable timing throughout the two days examined. There are some discrepancies in the strength, extent and evolution of convection throughout the simulation, but the important convective events are present at generally the right times and locations. The simulated surge wind field is too shallow and has smaller wind speeds than observed, but it moves at nearly the observed speed and has many similar features to the observed surge. Therefore the dynamics of the simulated surge should apply well to reality.

b. Surge dynamics

To answer the unresolved question of the dynamical mechanism of the initial gulf surge impulse, possible theoretical phenomena are compared to the simulated surge feature. Using the shallow water system of equations, equations for the propagation

speeds for linear Kelvin waves, solitary (non-linearity included) Kelvin waves and internal bores can be developed. Ralph et al. (2000) performs a similar analysis for a coastally trapped disturbance along the west coast of the US. Reason and Steyn (1992) develop the phase speed relationship for solitary Kelvin waves in a discussion of coastally trapped ridges and restate the phase speed for linear Kelvin waves as well, while Klemp et al. (1997) develop an improved phase speed relationship for internal bores. Ralph et al. (2000) adapt those equations to two possible scenarios for their study. Those same equations are adapted in a similar manner for this study as well.

One can view the stratified atmosphere as a shallow water system with two layers having different densities or potential temperatures for features that are described well by the hydrostatic balance approximation like Kelvin waves (Gill 1982; Reason and Steyn 1992) or bores (Klemp et al. 1997). In the case of gulf surges, the lower atmosphere is strongly stratified with a marine mixed layer topped by a strong inversion and another well mixed layer above the inversion. This atmospheric structure is suitable for approximation using the two layer shallow water system. Kelvin wave and bore phenomena occur on the interface between the two layers (Rottman and Simpson 1989; Reason and Steyn 1992; Klemp et al. 1997; Ralph et al. 2000). For this case, an idealized 2-d schematic oriented along the disturbance is shown in Fig. 4.16.

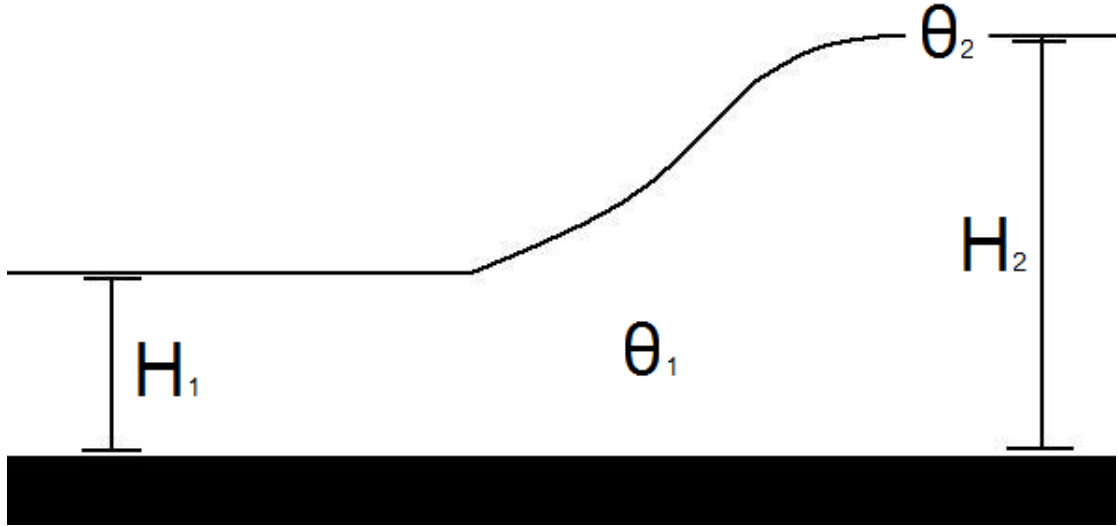


Figure 4.16. An idealized schematic in a two layer shallow water system of a disturbance moving along the inversion layer in the GoC. H_1 and H_2 denote the height of the top of the inversion before and after the leading edge of the disturbance passes. θ_1 represents the mass weighted potential temperature of the bottom and θ_2 is the temperature at the top of the inversion layer. The thin black line represents the inversion layer and the thick black line is the surface.

Using Fig. 4.16 as a template and the equations from Reason and Steyn (1992) and Klemp et al. (1997) one arrives at the phase speed relationships for linear and Solitary Kelvin waves and internal bores:

$$C_{LKW} = [g'H_1]^{1/2} \quad (4.1)$$

$$C_{SKW} = [g'H_2]^{1/2} \quad (4.2)$$

$$C_B = [g'2H_2^2/(H_1 + H_2)]^{1/2} \quad (4.3)$$

Where g' is reduced gravity given by:

$$g' = g[(\theta_2 - \theta_1)/\theta_2] \quad (4.4)$$

And the subscripts LKW, SKW and B stand for linear Kelvin wave, solitary Kelvin wave and bore respectively. Note that these are the intrinsic phase speeds, which is the propagation speed relative to the flow. Thus to determine the theoretical phase speed of

these three phenomena, one only needs to determine four parameters: two heights and two potential temperatures.

1) STRUCTURE 2

The four parameters needed to calculate the theoretical phase speeds for S2 on 12 July are estimated using the associated wind shift and speed increase. From Figure 4.3b and 4.4 the wind shift and speed increases are primarily seen below ~ 308 K. Examination of the along-the-cross section winds also highlights a maximum in wind magnitude below 308 K. Although the modeled cooling and moistening after the feature passage extends upwards to around 750 hPa (Fig 4.5), it appears that the cooling and moistening above 308 K (~ 800 hPa) is not associated with S2. The 308 K surface corresponds to a pre-disturbance height of ~ 1250 m and a post disturbance height of ~ 1900 m. Table 4.2 gives two estimated values of H_1 , H_2 , θ_1 , θ_2 . Using those values, Table 4.3 gives the theoretical phase speeds (determined as the average of the two parameter groups) for the three possible mechanisms. An areal and mass weighted vertical average of the flow over the region just

Table 4.2. Estimated values for H_1 , H_2 , θ_1 , θ_2 in the simulation for S2.

	H_1	H_2	θ_1	θ_2
Estimates from Simulation	1250 m 1400 m	1900 m 2300 m	303.4 K 303.6 K	308 K 309 K

ahead of S2 over the lowest 2 km gives an estimate of $\sim 4 \pm 0.2$ m s $^{-1}$ for the mean wind on the plane in which the feature is propagating. The modeled average total system speed from 16-20 UTC 12 July is 21 m s $^{-1} \pm 1.5$ m s $^{-1}$, less the 4 m s $^{-1}$ mean flow, gives a modeled intrinsic phase speed of 17 m s $^{-1} \pm 1.5$ m s $^{-1}$. This estimated phase speed is

closest to that of a solitary Kelvin wave. The uncertainty bounds of the theoretical phase speeds are determined by using the two stated height and potential temperature pairs.

Table 4.3. Theoretical phase speeds using the estimated values in Table 4.2 for S2.

	C _{LKW}	C _{SKW}	C _B
Theoretical Estimate	$14.5 \pm 1.0 \text{ m s}^{-1}$	$18.3 \pm 1.6 \text{ m s}^{-1}$	$20.2 \pm 1.9 \text{ m s}^{-1}$

Examining the leading edge of S2 in Figure 4.4 shows a possible leading undulation, in agreement with the more generalized theory in Reason and Steyn (1992). Several other parameters used in Reason and Steyn (1992) need to be estimated before continuing the discussion, the first of which is the Rossby radius of deformation, R :

$$R = c/f \quad (4.5)$$

Where c is the intrinsic phase speed of the feature and f is the Coriolis parameter. The second is d , which is a scaling parameter used in the calculation of the phenomena time scale, T .

$$d = \left[\frac{RH}{aL^*} \right]^{5/3} \quad (4.6)$$

$$T = d^{-3}f^{-1} \quad (4.7)$$

Where H is the depth of the lower layer, a is the perturbation height and L^* is an estimate of the alongshore length scale. This timescale is an estimate of the length of time it will take for the Kelvin wave to become established at a point. Using the model estimated phase speed and the Coriolis value at 25°N of $6 \times 10^{-5} \text{ s}^{-1}$, R is about 270 km. The alongshore length scale L^* is estimated at 425 km from time series information (not shown) and a is ~900 m ($H_2 - H_1$). Reason and Steyn (1992) use the ratio a/H as a measure of the non-linearity of a wave with larger values indicating more non-linearity.

From Eqn. 4.6 and Eqn. 4.7 one can see that if the wave is nearly linear and has an alongshore length that is near R , the timescale will be shorter than compared to a longer, more nonlinear wave.

Examination of MSLP anomalies at Los Mochis (not shown) find that it takes approximately 4 hours for the pressure to increase to a constant, higher level during S2 passage. The nonlinearity parameter, a/H is estimated to be 0.6 which indicates that the modeled wave should have some weak nonlinearity and explains the slightly faster than linear phase speed. The timescale is theoretically estimated at about 3.4 hours, which is in good agreement with the modeled value of about 4 hours.

Figure 4.17 shows a CS along AC2, near the leading edge of S2 at 16 UTC 12 July. The 304 K potential temperature contour gives a good estimate of the leading edge of S2 at this point seen through the wind shift from east-southeasterly to southerly below this contour. The convection forcing S2 is the reason the CS is taken far ahead of the peak disturbance height as there is convective contamination near and behind the peak. A necessary condition for coastally trapped Kelvin waves is that the potential temperature contours intersect the barrier (Zehnder 2004). There should also be decay in the cool dome associated with the Kelvin wave as the distance from the barrier increases. The CS shows that the potential temperature contours intersect the SMO (right side of CS) and also that there is a decay away from the SMO in the heights of the 302 and 304 K potential temperature contours. The channel width at this point is about 250 km, which is smaller than R here, which may explain why the 302 K isentrope appears to extend over the most of the GoC channel.

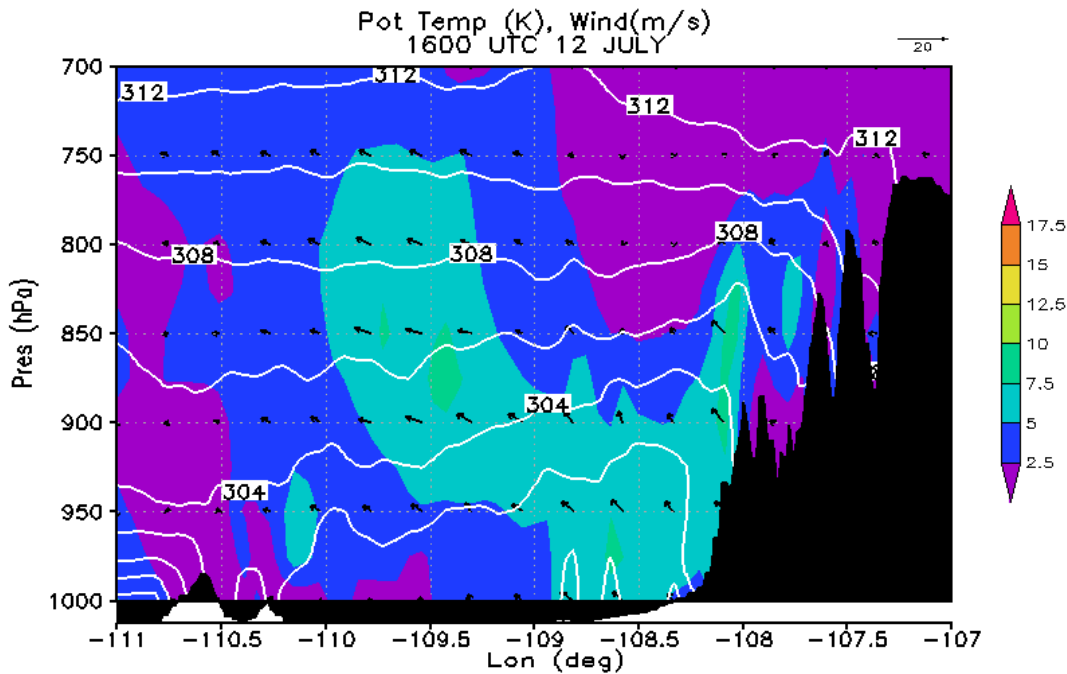


Figure 4.17. Same as Fig 4.13b, except taken along across-gulf cross section AC2 (shown in Fig. 4.12) at 16 UTC 12 July.

2) SURGE EVENT

(i) Southern and central GoC

The surge feature on 13 July is very complex with many subtle features and possible evolution through several dynamical mechanisms. An increase in cool air coming from the Pacific Ocean through gap flows and convectively cooled air from TS Blas near the mouth of the GoC appear to consolidate by around 04 UTC 13 July near Los Mochis and initiate the surge, with surface pressure rises occurring at Los Mochis between 01-06 UTC. Figure 4.18 shows a hydraulic jump resulting from Pacific air flowing through lower elevation gaps along AC3. There is a distinct wind shift from south-southeasterly ahead of the front, to westerly behind between 975 and 900 hPa and indications of some warming below 950 hPa as the 302 and 304 K theta contours approach the surface. The leading edge of the hydraulic jump (to the left of -110.5°

longitude) propagates to the east-northeast (not shown) shunting the cool air toward the

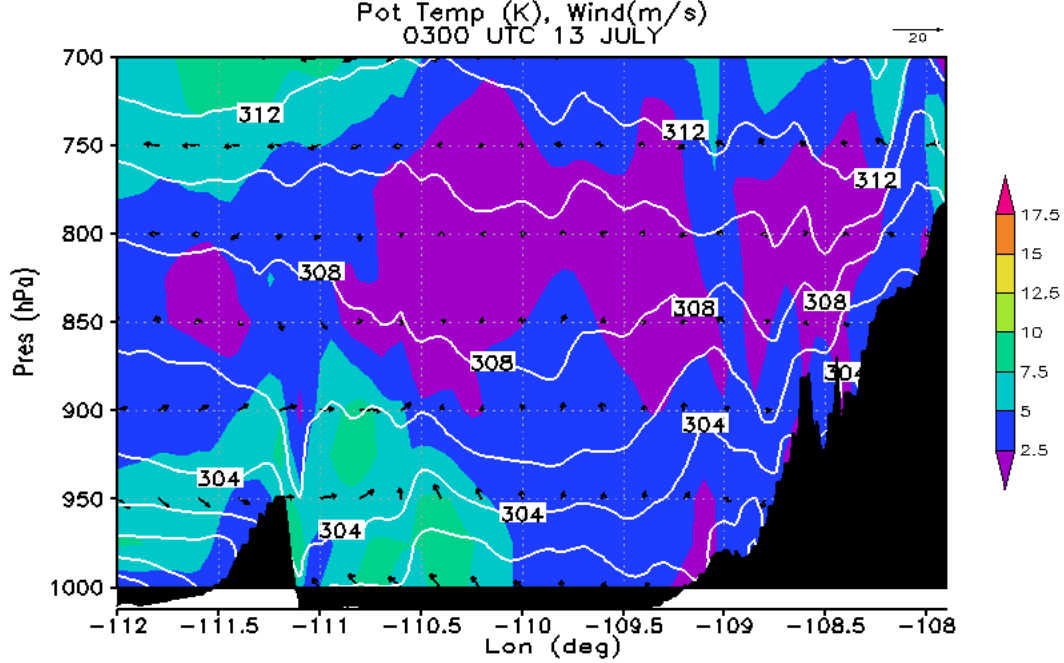


Figure 4.18. Same as Fig 4.13b, except taken along across-gulf cross section AC3 (shown in Fig. 4.12) at 03 UTC 13 July.

coastline. The pooling of cool air near the coastline may assist in the formation of a Kelvin wave-like wind and potential temperature structure shortly after 03 UTC.

Between 06 and 10 UTC 13 July there is substantial convective influence as noted above. The initial Kelvin wave feature is strengthened and merges with the large area of convective outflow along the central GoC. The along the wave flow is very strong with multiple gravity current and bore intrusions. Assuming a mean flow of $10 \pm 2 \text{ m s}^{-1}$ during this time frame, the resulting intrinsic phase speed of the surge is $13 \pm 2.2 \text{ m s}^{-1}$. Modeled potential temperature and mixing ratio soundings at KB indicate the pre-surge layer $H_1 \approx 400$ or 500 m with a mass-weighted mean temperature of 302.4 or 303.1 K, while the post surge layer is defined best by the 307 or 308 K isentrope and $H_2 \approx 1300$ or 1500 m. This results in the phase speeds summarized in Table 4.4. The best fit is the

solitary Kelvin wave solution, which makes physical sense considering $a/H \approx 2\text{-}2.25$ at this junction, indicating the wave is nonlinear (Reason and Steyn 1992).

Table 4.4. Theoretical phase speeds using the estimated values for the surge near KB.

	C_{LKW}	C_{SKW}	C_B
Theoretical Estimate	$8.3 \pm 0.6 \text{ m s}^{-1}$	$14.6 \pm 0.8 \text{ m s}^{-1}$	$18.0 \pm 0.9 \text{ m s}^{-1}$

(ii) Northern GoC

Now focus will shift to the surge in the northern GoC, after 10 UTC 13 July. Figure 4.19 displays the modeled and observed potential temperature before and after surge passage at PP. The most significant low-level cooling occurs below 900 hPa in both the observations and simulation; however simulated cooling is present through 600 hPa making determination of the surge top more difficult. Moistening is present in the simulation below ~ 900 hPa, while the wind shifts to more easterly above ~ 850 hPa (not shown). This suggests the top of the surge feature is located somewhere around 309-310 K. Another factor in determining the height of the perturbation is the height of the barrier, which is near or just above the 310 K surface. Coastally trapped Kelvin waves typically extend to near the top of the barrier (Holland and Leslie 1986; Skamarock et al. 1999). The northern SMO extends to around 850 hPa, which is near 310 K. It may also be that the cooling above 850 hPa is caused by other factors such as a general wind shift from easterly flow to southerly, likely influenced by TS Blas.

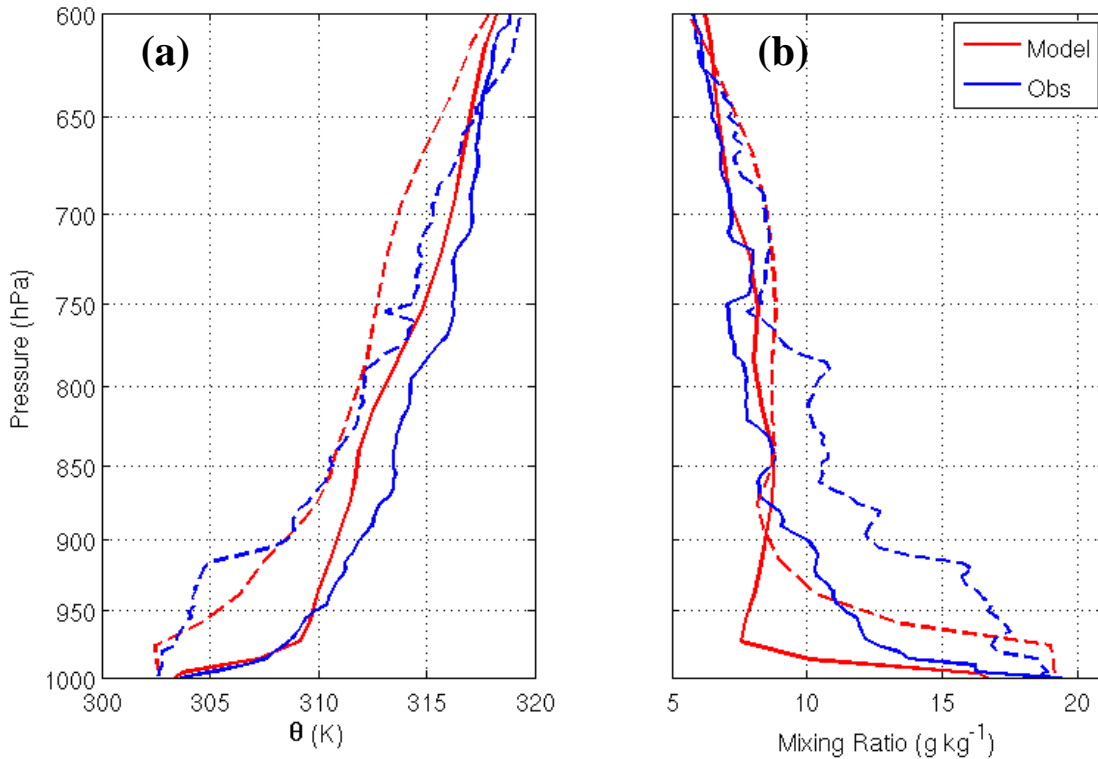


Figure 4.19. Same as Figure 4.5, except for Puerto Penasco.

Figures 4.20 and 4.21 display simulated MSLP and potential temperature anomaly from the surface to 700 hPa at PP respectively. The observed NAME mean diurnal cycle was used for surface anomaly calculations, while the NARR NAME mean diurnal cycle was used for anomaly calculations aloft. These two figures show the initial gravity current passage between 00 and 04 UTC 13 July with anomalous cooling associated with increasing wind speeds, a change in wind direction, and a sharp rise in MSLP followed by a quick decline. Figure 4.22 displays simulated omega at PP. One can see upward motion coinciding with the leading edge of the gravity current with a maximum around 1000 m, followed by sinking motion behind the head with the maximum higher aloft, near 2500 m.

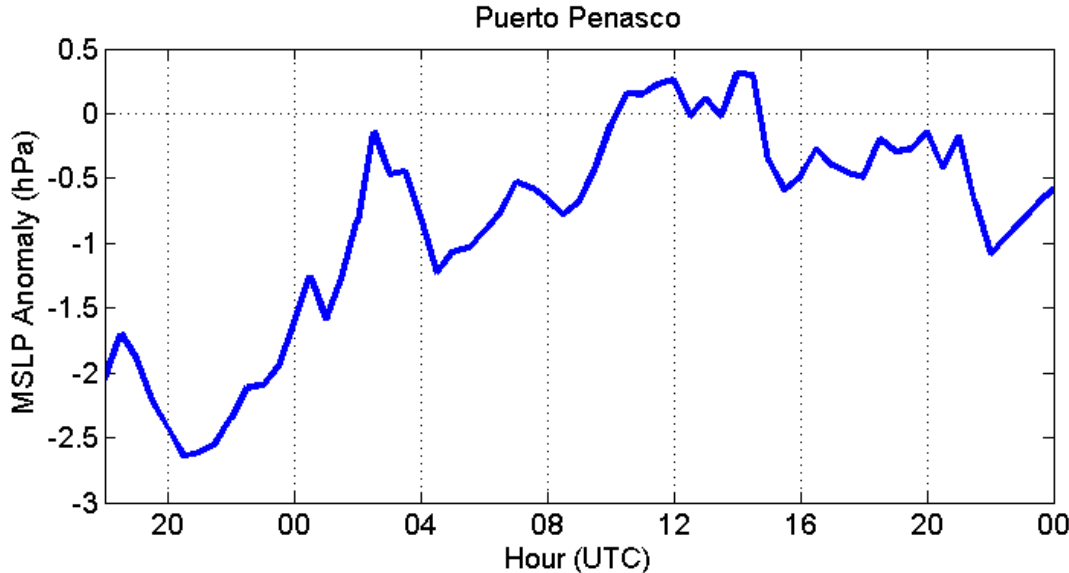


Figure 4.20. Puerto Penasco anomalous MSLP (red (hPa)) from 18 UTC 12 July to 00 UTC 14 July. The mean NARR NAME period diurnal cycle MSLP was used to create the anomalies for the simulation.

The second outflow passage near 05-07 UTC is likely a bore passage due to the lack of significant near-surface cooling, cooling around 975 hPa, a sharp MSLP rise between 0530 and 07 UTC followed by steady MSLP anomalies through 0830 UTC, and the initial wind increase occurs near 975 hPa. Also, there is slight anomalous surface warming around 07 UTC, which corresponds with simulated downward motion extending to the surface, indicating mixing of potentially warmer air to the surface behind the lead undulation (Martin and Johnson 2008). Wind direction analysis is severely complicated by the prior gravity current passage and is ignored. There may be some residual of the gravity current signature around 07-08 UTC with slight surface cooling and further increase in wind magnitude from the surface to 950 hPa. The omega field (Fig. 4.22) shows strongly oscillating vertical velocities between 0530 and 0830 UTC. The leading edge of the bore has upward motion, followed by strong downward motion.

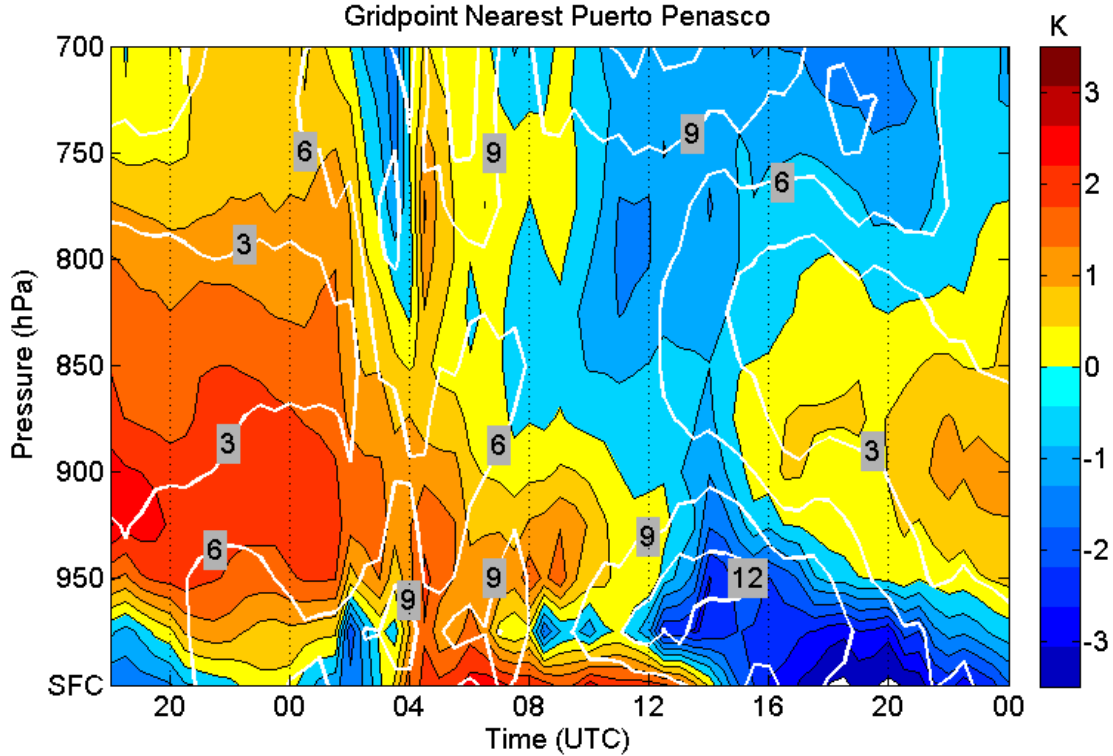


Figure 4.21. Potential temperature anomalies (shading (K)) and wind magnitude (white contours (m s^{-1})) at Puerto Penasco for 18 UTC 12 July to 00 UTC 14 July. The anomalies were calculated using the NARR NAME period mean diurnal cycle above the surface and the observed NAME mean diurnal cycle for the 2-m values.

A second oscillation follows, with strong upward motion leading downward motion through 0830 UTC. This bore passage is similar to one observed by Knupp (2006) in the central US before the generation of the solitary wave in their case.

Beginning around 0830-09 UTC 13 July, the surge signature begins to impact PP with an increase in MSLP and wind speed. This initial surge feature will be denoted as Feature 1 (F1). No anomalous surface cooling occurs with the cooling again located near 975 hPa, extending upwards to 900 hPa by 12 UTC. An upward/downward vertical velocity couplet is present with the arrival of this impulse between 10-1230 UTC. Again, there is actually slight, brief warming around 10 UTC (Fig. 4.21). This may be related to vertical mixing even though there are no large vertical velocities near the surface to

indicate mixing. There is an increase in surface wind velocities, which would increase mechanical mixing and possibly raise the 2 m temperatures as well. Following this undulation, another deeper undulation passes over PP beginning around 1230 UTC (Fig. 4.21). This second, deeper feature will be denoted as Feature 2 (F2). Significant,

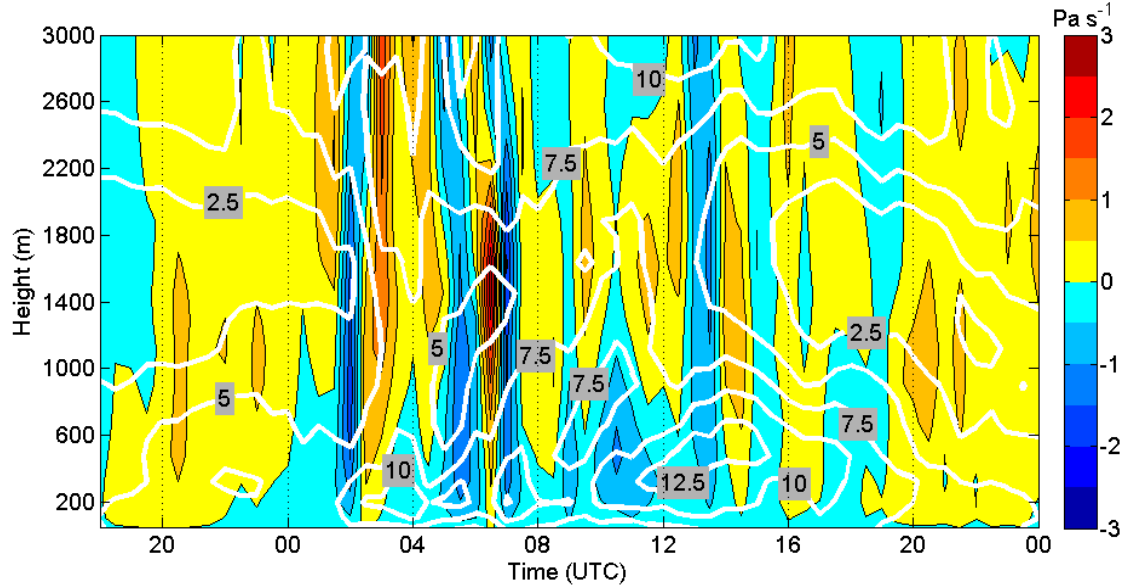


Figure 4.22. Simulated omega (neg. upwards (Pa s^{-1})) for Puerto Penasco from 18 UTC 12 July to 00 UTC 13 July from 50 to 3000 m.

anomalous surface cooling does not occur in the simulation until after 13 UTC when another impulse begins to arrive. This can be seen in the deepening potential temperature anomalies and wind field (Fig. 4.15) after 12 UTC as well as a slight MSLP rise at 13 UTC. The downward motion associated with the first impulse quickly transitions to upward again after 1230 UTC leading into another vertical velocity couplet between 13–15 UTC.

Examination of the surge at PP within the theoretical framework discussed above leads to estimates for the four phase speed parameters summarized in Table 4.5, while Table 4.6 gives the corresponding phase speed estimates. The estimated background flow in the direction of F1 (the initial shallow feature at ~ 10 UTC) is $6 \pm 0.5 \text{ m s}^{-1}$; while

the background flow in the direction of F2 (the deep second feature at \sim 12 UTC) is estimated at $8 \pm 0.6 \text{ m s}^{-1}$. Table 4.1 gives the estimated surge front a total system speed of $21 \pm 1.5 \text{ m s}^{-1}$ in the northern GoC. Comparisons to Table 4.6 show that if F1 were a bore, it would have a total system speed of $18.2 \pm 1.7 \text{ m s}^{-1}$, while if F2 were a solitary Kelvin wave, it would have a total speed of $21.0 \pm 1.7 \text{ m s}^{-1}$, with a bore having a total speed of $21.7 \pm 1.7 \text{ m s}^{-1}$.

Table 4.5. Estimated values for H_1 , H_2 , θ_1 , θ_2 in the simulation for the surge at PP.

	H_1	H_2	θ_1	θ_2
Feature 1	300 m	800 m	305 K	308.5 K
	400 m	1050 m	306 K	309.5 K
Feature 2	800 m	1050 m	304 K	308.5 K
	1050 m	1300 m	305 K	309.5 K

Table 4.6. Theoretical phase speeds using the estimated values in Table 4.5 for the surge at PP.

	C_{LKW}	C_{SKW}	C_B
Feature 1	$6.3 \pm 0.5 \text{ m s}^{-1}$	$10.1 \pm 0.7 \text{ m s}^{-1}$	$12.2 \pm 0.8 \text{ m s}^{-1}$
Feature 2	$11.5 \pm 0.8 \text{ m s}^{-1}$	$13 \pm 0.7 \text{ m s}^{-1}$	$13.7 \pm 0.7 \text{ m s}^{-1}$

The ratio H_2/H_1 is calculated for F1, which is used to distinguish between different types of bores (Rottman and Simpson 1989). Rottman and Simpson (1989) observe in a laboratory, three types of bores, A, B, and C. Type A bores are smooth undular bores with little to no turbulence along any point of the bore and occur when H_2/H_1 is less than 2. Type B bores have intermittent turbulence after the crest initial undulation and occur for $2 < H_2/H_1 < 4$. Type C bores have extensive turbulence behind the crest of the leading undulation, resemble a gravity current, and occur for $H_2/H_1 > 4$. For F1, the best estimate of this ratio is ~ 2.6 , which is near the interface of the Type A and B bores (Rottman and Simpson 1989). A weaker simulated vertical velocity field,

but one with possibly two up/down couplets, may indicate a relative lack of turbulence and suggest an undular bore of either type A or B.

For F2, it appears that a solitary Kelvin wave or bore is the most likely candidate based on the phase speed analysis and other characteristics. The solitary Kelvin wave solution agrees best with the onset of surface cooling at PP and slight pressure increase. However, the simulated pressure anomaly decrease of ~ 1 hPa after the passage of F2 is not consistent with a Kelvin wave. It is possible that a solitary Kelvin wave would induce a vertical velocity couplet seen, with the downward velocities seeming to correspond with the MSLP anomaly decrease. After this decrease, the MSLP anomaly stays nearly constant, with some slight rise through 21 UTC, which is consistent with a Kelvin wave passage. After 21 UTC, the simulation has another decrease in MSLP anomaly, which seems to be associated with large-scale subsidence that may be too strong in the simulation. Stronger modeled subsidence above the inversion layer would also be consistent with the surge features being too shallow.

Another indication that F2 may be a solitary Kelvin wave is that a nonlinear wave cannot follow a convex bend greater than some critical angle without it separating from the coast or suffering some other loss of identity (Miles 1977; Reason and Steyn 1988; 1992). For F2, $a/H \approx 0.5$, indicating some nonlinearity (Reason and Steyn 1992). The critical angle for a convex bend is defined as:

$$\phi_c = \sqrt{3\alpha} \quad (4.8)$$

With α being the amplitude of the solitary wave. For the surge at this point, $\alpha \approx 0.4$, meaning a solitary Kelvin wave could not pass a convex bend with an angle greater than $\sim 65^\circ$ without separation or some other loss of wave identity. The ridge at 30°N , seen in

the 500 m height contour in Fig. 4.12 extends upward to near 600-900 m (940-920 hPa), above the peak in the simulated winds. This ridge has a convex bend at 30°N, -112.2°W with an angle of approximately 135°, which is much larger than the critical angle for a solitary Kelvin wave with the characteristics of F2. Figure 4.23 gives CSs south of the

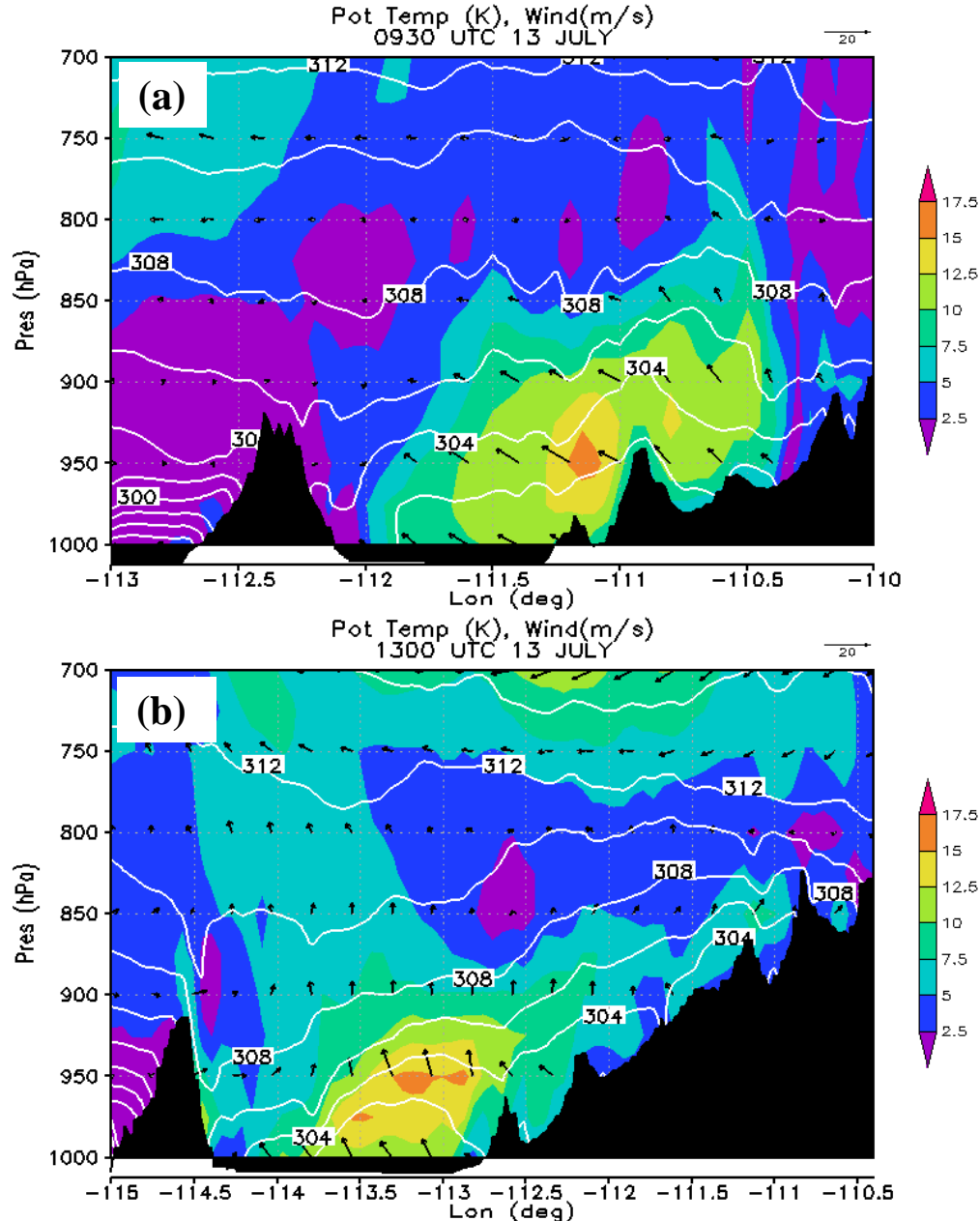


Figure 4.23. Both cross sections are the same as Fig 4.13b, except (a) is taken along across-gulf cross section AC4 at 0930 UTC and (b) is taken along across-gulf cross section AC5 at 13 UTC 13 July.

ridge (AC4) (a) and north of the ridge (AC5) in (b). One can immediately see that in (a) the maximum in surge winds is very near the topography and decays away over the GoC. In Fig. 23b, the strong flow confined below 925 hPa (\sim 750 m) has separated away from the coastline as well as the 302 K isentrope. Finally in both panels of Fig. 4.23, the surge feature appears to be trapped by the topography and decays away from the SMO, again indicating a Kelvin wave.

3) DYNAMICAL SUMMARY

The features associated with structure 2 (S2) on 12 July (Figs. 4.3 and 4.4) indicate that it is a Kelvin wave feature, with the maximum amplitude in the wind field and coldest potential temperatures near the coastline. Phase speed analysis using an idealized shallow water system and the work performed by Reason and Steyn (1992), Klemp et al. (1997) and Ralph et al. (2000) show that a solitary Kelvin wave solution is the best match. Further comparisons to nonlinear theory developed by Reason and Steyn (1992) have features that agree well with the simulation, e.g., the timescale of the Kelvin wave ridge establishment.

On 13 July the initial surge forms through a consolidation of cool air moving into the GoC from near the mouth, along with convective outflow impinging on the coastal plain around 04 UTC 13 July. There is also gap flow from the Pacific Ocean creating a hydraulic jump that moves eastward, forcing the cool air into the SMO. As this initial Kelvin wave moves up the GoC, many convective outflows, either gravity currents or bores, impinge upon the GoC near and ahead of the initial Kelvin wave, causing enhancement and deepening of the cool anomaly. As the surge moves into the central/northern GoC, after 08 UTC, the GoC LLJ is likely complicating the surge event

further. However, it appears that the best fit via phase speed analysis in the north central GoC, near KB, is that of a solitary Kelvin wave. At PP, the observed potential temperature profiles are quite similar to the simulation, except for the well-defined mixed layer present in the observations. That fact, along with using Fig. 11 from RJ2007, gives similar values for the depth of the lower layer before (H_1) and after (H_2) wave passage for the surge at PP. Using the onset of significant anomalous cooling in RJ2007, the surge total system speed is $\sim 21 \text{ m s}^{-1}$ between KB and PP. Assuming a similar flow component with the surge of $6\text{-}8 \text{ m s}^{-1}$, gives an intrinsic phase speed of $\sim 13\text{-}15 \text{ m s}^{-1}$, which would be in-line with a solitary Kelvin wave. Finally, RJ2007 notes similar features with the surge passage including a bore-like feature before “there is a deeper layer of cooling extending to the surface,” that seems to be related to a Kelvin wave passage. With similar total velocities estimated by RJ2007 and similar theoretical phase speeds due to similar height and temperature parameters, it is likely that the observed surge was indeed a bore followed by a solitary Kelvin wave at PP.

2. Topographic and microphysical modifications

From the control simulation, it appears that inflow from the Pacific Ocean may have played a role in initiating the surge and likely modified its structure along the GoC. Also, in agreement with the modeling study Stensrud et al. (1997) and many observational papers (Hales 1972; Brenner 1974; RJ2007) this study shows convective outflow is critical to surge initiation. To investigate the sensitivity of the surge evolution to these two critical modulating processes, two sensitivity runs were performed for the same time period as the control, 12 UTC 11 July – 00 UTC 14 July. As discussed prior, a modification to the microphysics routine was made to remove all sub-cloud base rain

evaporation, with cloud base being defined as the first level above ground with cloud water greater than 0.1 g kg^{-1} , which is a typical value near the edges of cumulus clouds (Pruppacher and Klett 1997). This idea follows the same road as Stensrud et al. (1997) in which they removed all diabatic effects to assess the impact of convective outflow on surge development, but this case is different in that the convective modification is less drastic and convection is explicitly resolved. To reduce the Pacific air inflow into the GoC, the gaps in the Peninsular Ranges were raised to 1000 m from the tip of the peninsula to 32.5°N , which reduced said inflow.

a. No sub-cloud evaporation

The evolution of convection on 12 and 13 July in this simulation is fairly similar to the control simulation (Fig. 4.24). The convective movement and evolution is faster in the control simulation (Fig 4.24a,c), which is expected in a simulation having stronger cold pools moving faster (Benjamin 1968; Wakimoto 1982) and outrunning the parent convection causing system dissipation (Byers and Braham 1949; Weisman et al. 1988; Rotunno et al. 1988). As examples, the convection in the northern GoC (near 30°N) (Fig 4.24a,b) is simulated farther east in the control simulation and has a more extensive and slightly colder (on average) cold pool at 00 UTC (Fig 4.25). The minimum potential temperature associated with the cold pools north of 29°N is 301 K for both simulations is 301 K; however the surface area covered by potential temperatures less than 306 K (distinctly less than environment) is 2125 km^2 and 224 km^2 for the control and No_SUBCLD runs respectively, which is nearly a factor of 10 different. Along the entirety of the SMO, the No_SUBCLD run has an average cold pool temperature (areas less than 306 K) $\sim 1 \text{ K}$ higher. By 06 UTC, the convective cluster located at 29°N , -

108.5°W (Fig 4.24c,d) is beginning to dissipate and is completely dissipated by 0930 UTC in the control run, while the No_SUBCLD cluster has higher radar reflectivity values at 06 UTC and the cluster remains until \sim 11 UTC (not shown).

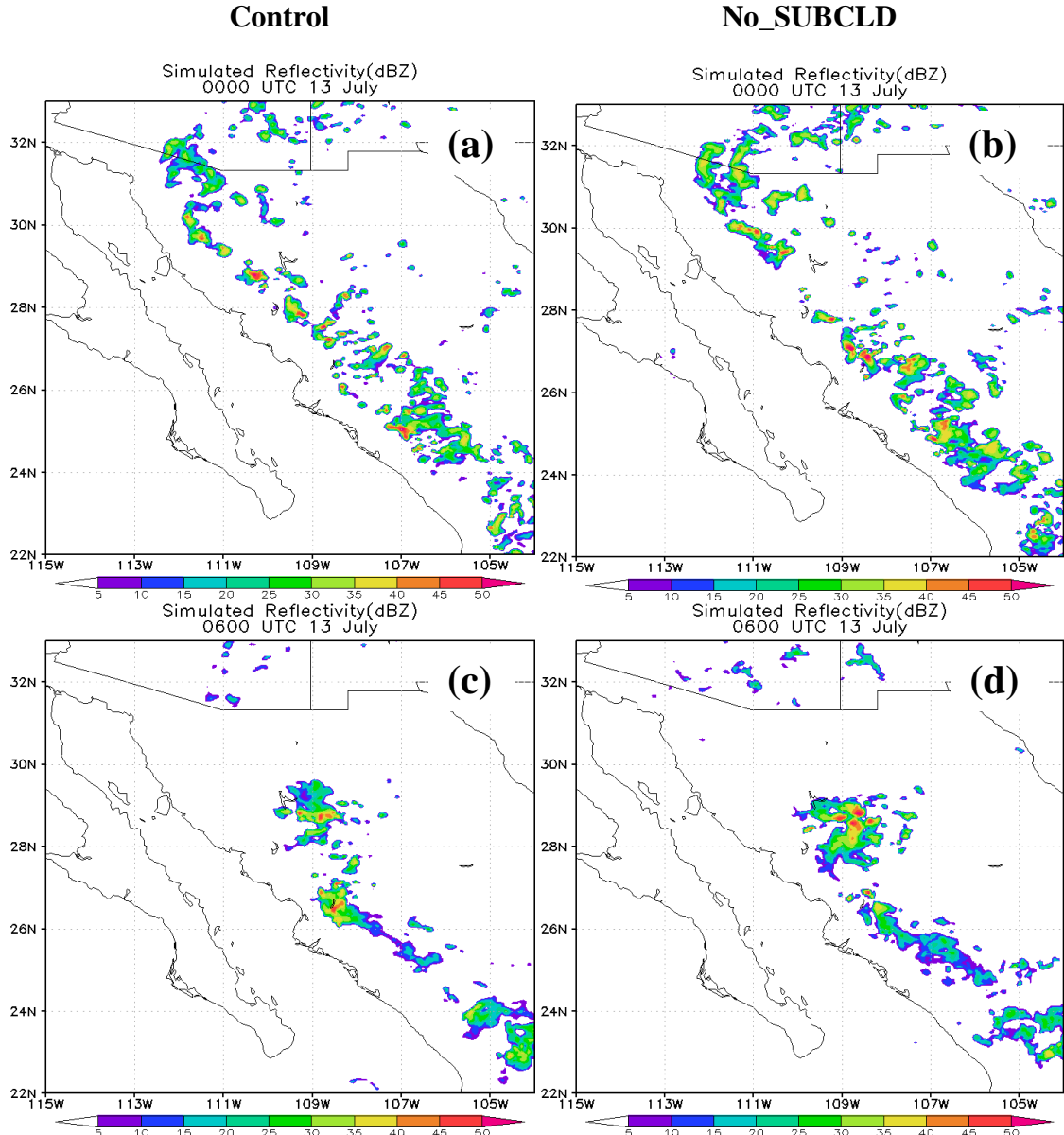


Figure 4.24. Simulated reflectivity (dBZ) from the control run at 00 (a) and 06 UTC 13 July (c) and the No_SUBCLD (b) and (d) at the same times.

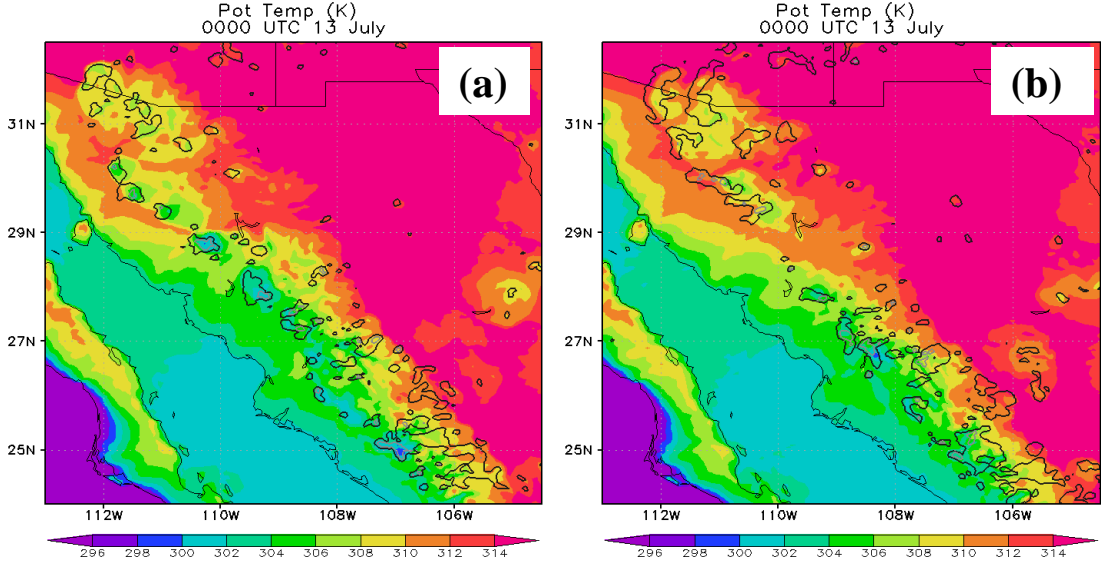


Figure 4.25. First model level (~40 m AGL) potential temperature (K) (shading) from the control run (a) and No_SUBCLD (b) at 00 UTC 13 July. The 20 (thick black) and 40 (thick gray) dBZ reflectivity contours are given for reference.

Figure 4.26 displays the 950 hPa moisture flux for the No_SUBCLD run in the same manner as Figure 4.12. Initially, (Fig. 4.26a) the No_SUBCLD surge is more intense with a larger area of greater than $120 \text{ g m kg}^{-1} \text{ s}^{-1}$ moisture flux in the southern GoC. This is due to more inflow of cool moist air from the mouth of the GoC. TS Blas is located in nearly the same position in both simulations and the convection associated with the northern outer band is nearly identical as well (not shown). It is possible the slightly altered position of TS Blas and low-level pressure gradient results in slightly stronger low-level winds near the mouth of the GoC early on 13 July in the No_SUBCLD case. However, when the convective outflow begins to impinge on the initial surge feature, the control case moisture flux is larger for the duration of the surge. Comparisons between Figure 4.26b-d and Figure 4.12b-d along with Table 4.7 show that the control run has larger maximum moisture flux values as well as more area greater than $150 \text{ g m kg}^{-1} \text{ s}^{-1}$.

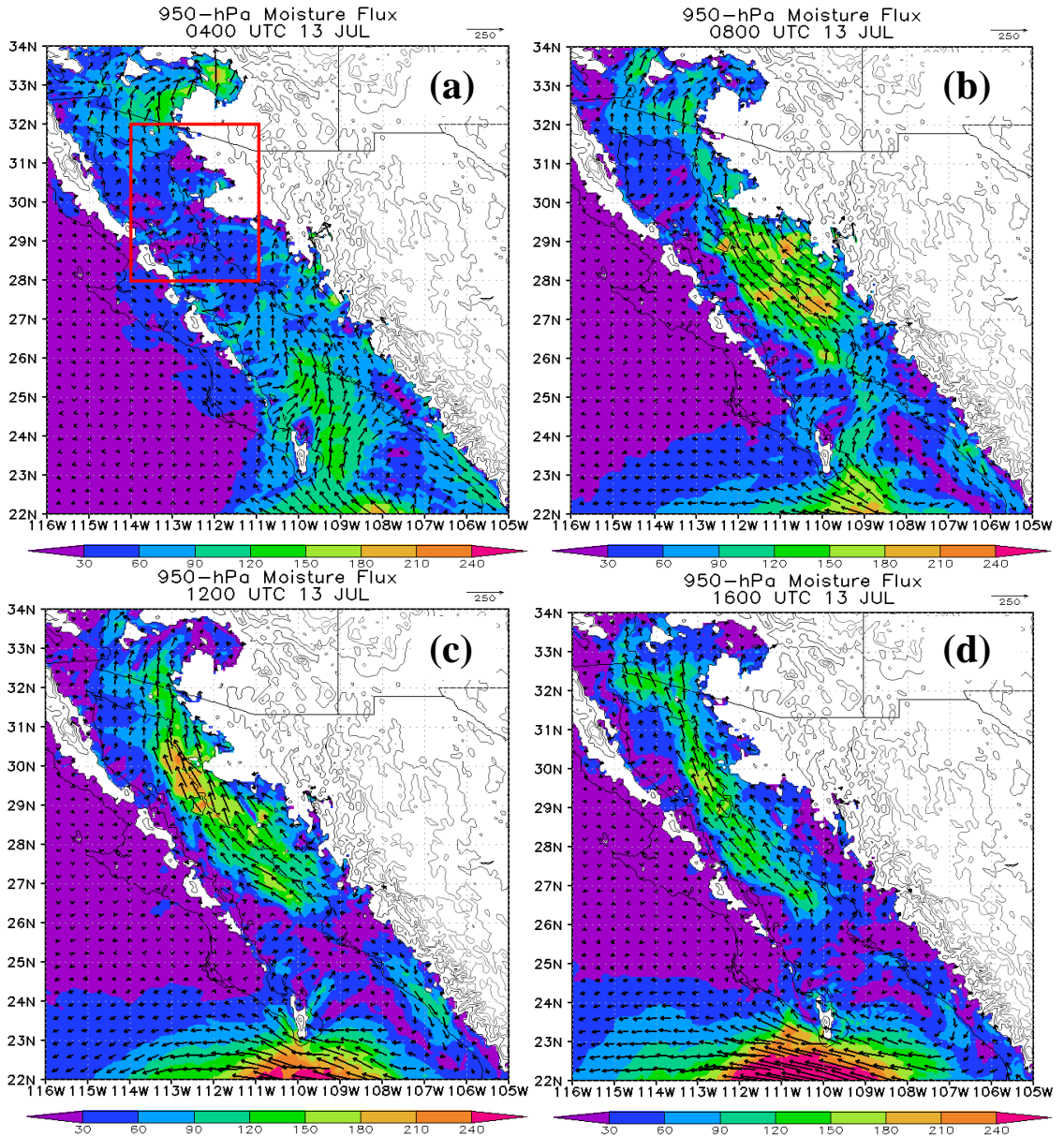


Figure 4.26. Same as Fig. 4.12 except for the No_SUBCLD simulation. The red box in (a) indicated the area used for the mean surge wind magnitude analysis.

Table 4.7. Area (km^2) with moisture flux values greater than $150 \text{ g m kg}^{-1} \text{ s}^{-1}$ for the No_SUBCLD and control simulations at 08, 12, and 16 UTC 13 July.

	No_SUBCLD	Control
08 UTC	27488	44544
12 UTC	24480	40560
16 UTC	3488	19440

At each model output time, the mean magnitude of the wind field in the northern GoC within the box shown in Figure 4.26a, below 900 hPa was computed. The No_SUBCLD simulation has a lower mean wind speed associated with the core of the surge event between 10-15 UTC 13 July than the control run and 7.2 m s^{-1} versus 7.7 m s^{-1} . A mean difference of 0.5 m s^{-1} over such a large area and time period is notable. However, since there was only one run using each configuration, it is essentially impossible to assess the statistical significance of that difference. This result does fit within the hypothesis proposed, that weaker convective outflow will result in a weaker surge, which is what Stensrud et al. (1997) found with a much coarser resolution and parameterized convection.

b. Modified topography

The control simulation indicated a possible role in surge formation and evolution for Pacific air intrusions into the GoC through gaps in the Peninsular Ranges. By raising the height of the topography to 1000 m (Fig. 2.5), the amount of Pacific air entering the GoC is greatly reduced. The Froude number in the northern GoC along the gap at 30°N is ~ 0.7 in the control run at 00 UTC 12 July, while it is ~ 0.4 in the modified topography run at the same time indicating increased blocking along the Baja Peninsula at that point. Figure 4.27 shows the 925 hPa wind for the modified topography (a) (No_gaps) and control (b) simulations. Note the significant decrease in wind magnitude for the westerly winds in the western GoC, especially near $24\text{-}25^\circ\text{N}$ and $29\text{-}30^\circ\text{N}$. It is hypothesized that the Pacific air may be involved in the consolidation of the initial surge feature, and also reinforces the GoC inversion layer along the length of the channel, making the environment more conducive to surge events. The second possibility initially considered

is that the inflow is not vital to surge initiation and is just a modifying factor. Furthermore, the dry air intrusions may encroach onto the eastern coastal plain of the GoC in a modified form (see Fig. 4.11) and create a less favorable environment for convection, therefore weakening cold pool production and the subsequent surge event.

It appears that the increased blocking in the No_gaps run does prevent drier air from encroaching onto the eastern coastal plain of the GoC, especially on 11 and early 12 July. As seen in Figure 4.27, there is continuous westerly flow of greater than 5 m s^{-1} from the Baja Peninsula into the SMO near 30°N in the control run while there is only the diurnal sea breeze flow near the SMO in the No_gaps run. There are also areas of enhanced westerly flow near 27.5°N and between $23.5\text{--}25.5^\circ\text{N}$. This approximately 24-

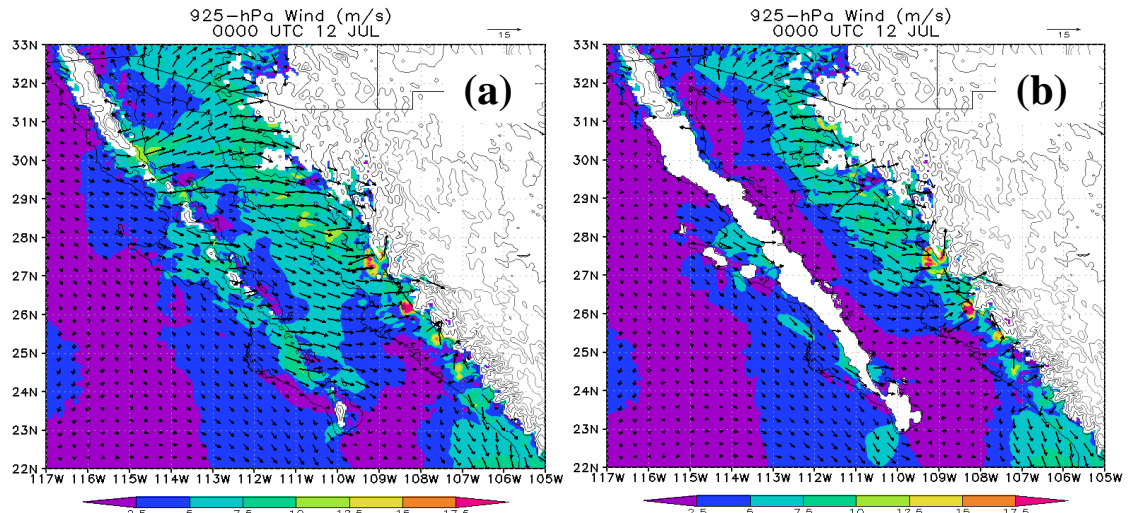


Figure 4.27. 925 hPa wind magnitude (m s^{-1}) (shading) and vectors (arrows) at 00 UTC 12 July. Topography height (contours at 0, 500, 1000, 1500, 2000 and 2500 m with lighter shading indicating higher terrain). Areas in white are elevations above the 925 hPa elevation level.

hour period of sustained Pacific inflow along large portions of the Peninsular Ranges, creates an environment with less moisture in the lowest levels in the control run preceding convective initiation on the afternoon of 12 July. Figure 4.28a displays the mass weighted difference in specific humidity between the control and No_gaps run

(control minus No_gaps) for the surface to 850 hPa at 18 UTC 12 July, while Fig. 4.28b displays potential temperature determined in the same fashion. Nearly the entire coastal plain and SMO foothills have higher specific humidity in the No_gaps run (blue shading), with the same areas having generally higher layer average potential temperatures in the control run.

The increased low-level moisture and corresponding slight decrease in temperature makes convective available potential energy (CAPE) differences less distinct, but the areas of increased moisture in the No_gaps run generally correspond to areas with more lowest 90 hPa mixed layer CAPE over the land (Fig. 4.28c). More low-level moisture (and CAPE) seems to be the reason for slightly more robust and long-lived convection in the No_gaps simulation, allowing for more cold pool generation (Fig. 4.28d), even in the face of slightly decreased low-level inflow (not shown). Figure 4.28d also reveals higher potential temperatures in the control run along most of the eastern GoC coastline and GoC between 27-31°N. The higher potential temperatures in the control run in the extreme northwest GoC in Fig. 4.28d are associated with enhanced Pacific inflow and a weaker surge. This appears to be due to the Pacific inflow restricting the western edge of the surge from fully impacting this portion of the GoC, while in the No_gaps simulation, reduced gap flow and a stronger surge result in a larger surge related cooling.

Higher layer-average potential temperatures in the control run seem counterintuitive since the Pacific air on the west side of the Baja is significantly colder than the air in the GoC. However, the Peninsular Ranges provide just enough of a barrier to block the lowest levels. This creates a situation where the air entering the gap flow

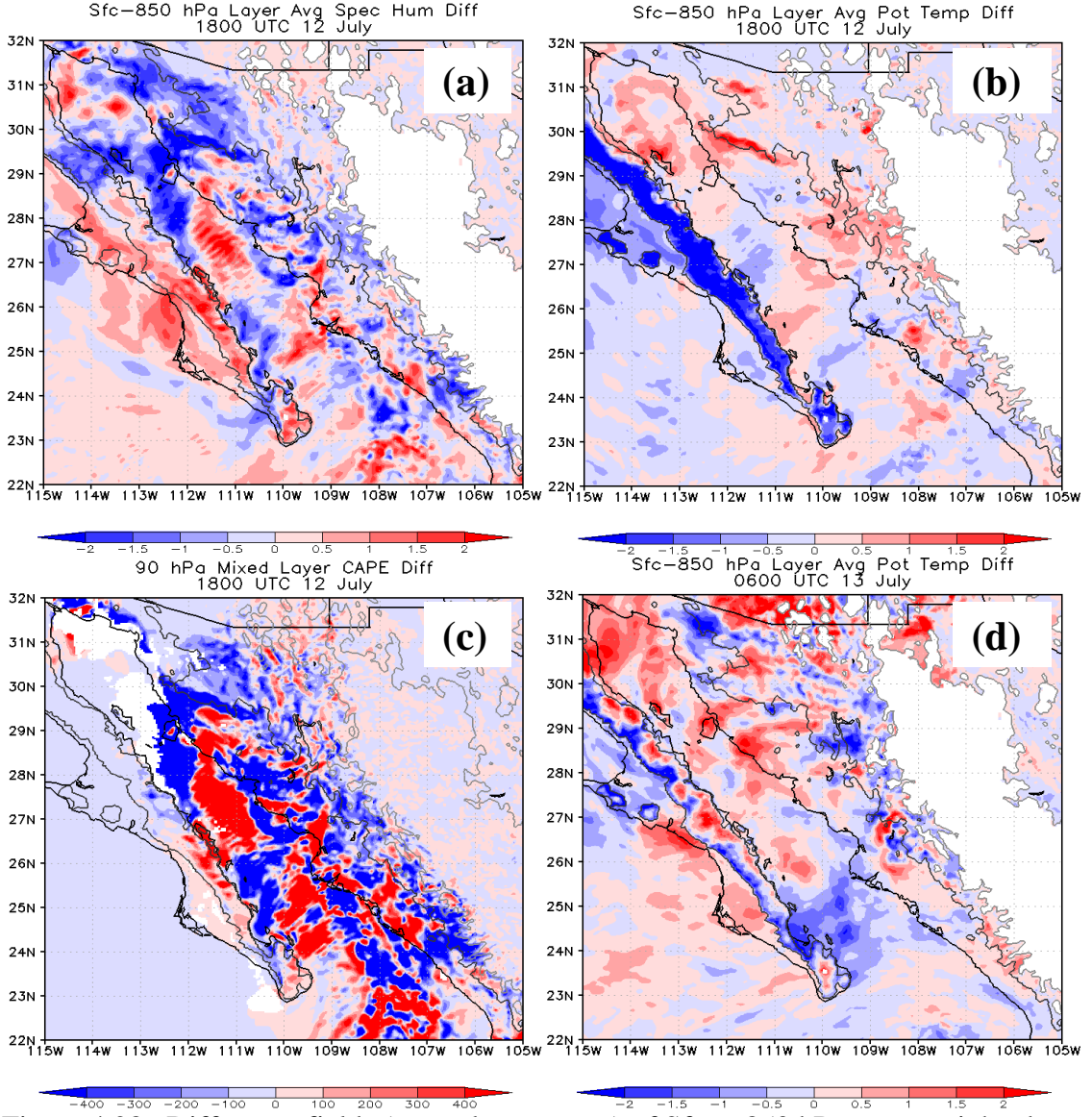


Figure 4.28. Difference fields (control – no_gaps) of Sfc to 850 hPa mass weighted mean specific humidity (g kg^{-1}) (a), potential temperature (K) (b), lowest 90 hPa above ground mixed layer CAPE (J kg^{-1}) (c) at 18 UTC 12 July, and potential temperature (K) at 06 UTC 13 July (d). Topography height (contours at 0, 500, 1500 m with lighter shading indicating higher terrain), with areas in white above the 850 hPa elevation level except in (c). White areas in (c) have convective inhibition $> 200 \text{ J kg}^{-1}$

regions is potentially warmer than the air in the GoC and in the inversion layer near the surface. Figure 4.29 shows a CS along 30°N from 116°W to 111°W for the control (a) and No_gaps (b) simulations. There is a well mixed layer (the $310\text{-}312 \text{ K}$ contours are relatively far apart) and hydraulic jump along the Baja Peninsula (114.5°W) in the control

run. The blocking of air with potential temperatures less than at least 304 K is evident as well. The No_gaps run exhibits nearly completely blocked flow without the signature of a hydraulic jump and corresponding well mixed layer. It also appears that the elevated

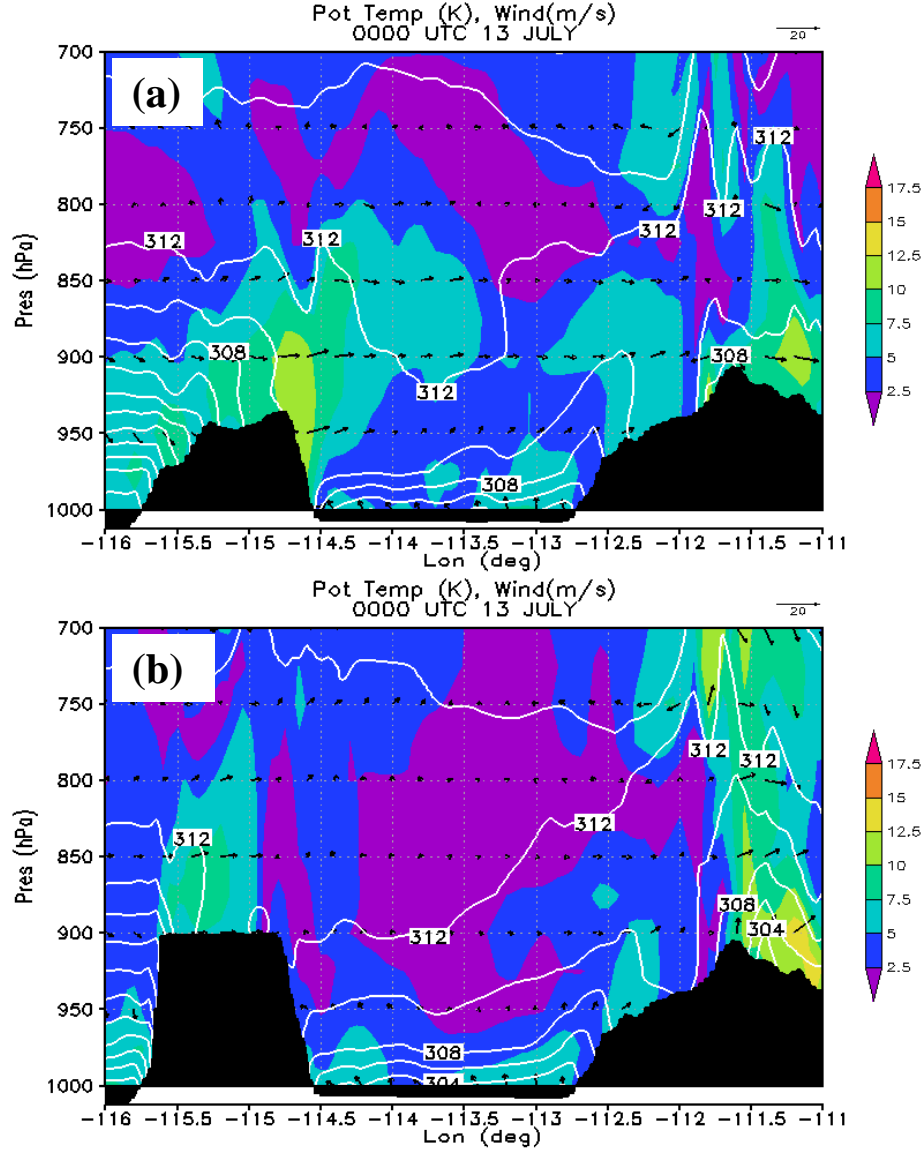


Figure 4.29. Same as Figure 4.13b, except for a plane along 30°N for the control (a) and No_gaps (b) simulations at 00 UTC 13 July.

hydraulic jump and flow in the control run may induce compressional warming in the inversion layer near the surface over the GoC. The 304-308K isentropes are slightly elevated in the No_gaps run as compared to the control simulation.

Therefore, the original hypothesis that Pacific air helps to reinforce the low-level GoC inversion seems to be incorrect. In the control simulation it appears that the flow is partially blocked along the southern Baja Peninsula, with any flow cresting the topography being potentially warmer than the marine layer in the GoC resulting in a well mixed, warm area near the Baja Peninsula on the west side of the GoC (see Fig. 4.15). Evidence of this is also seen in Figure 4.25b along a majority of the western GoC with the control run having higher layer average potential temperatures (red shading). Figure 4.30 displays a sounding from 30°N , 114°W at 00 UTC 13 July. The adiabatic layer extends to very near the surface in the control run with higher temperatures and significantly lower dew points below ~ 925 hPa. A deeper adiabatic layer, essentially to the surface, would inhibit surge propagation in the western GoC in the control run while the No_gaps run has conditions more similar to the eastern GoC across its entirety. This is because internal bores and Kelvin waves are gravity wave phenomena, which require a stably stratified environment for propagation (Reason and Steyn 1992; Klemp et al. 1997). That being said, the gap flows do not change the basic nature of the surge event. The features and dynamics of the No_gaps run are very similar to the control simulation.

All these factors should then combine to create a stronger surge in the No_gaps run, which is confirmed in Figure 4.31, Table 4.8 and wind analysis in the northern GoC. By 04 UTC 13 July the No_gaps run has very similar moisture flux values in the southern GoC as the control run. This time it is associated with reduced Pacific air intrusion and increased transport from the mouth of the GoC. This indicates the large

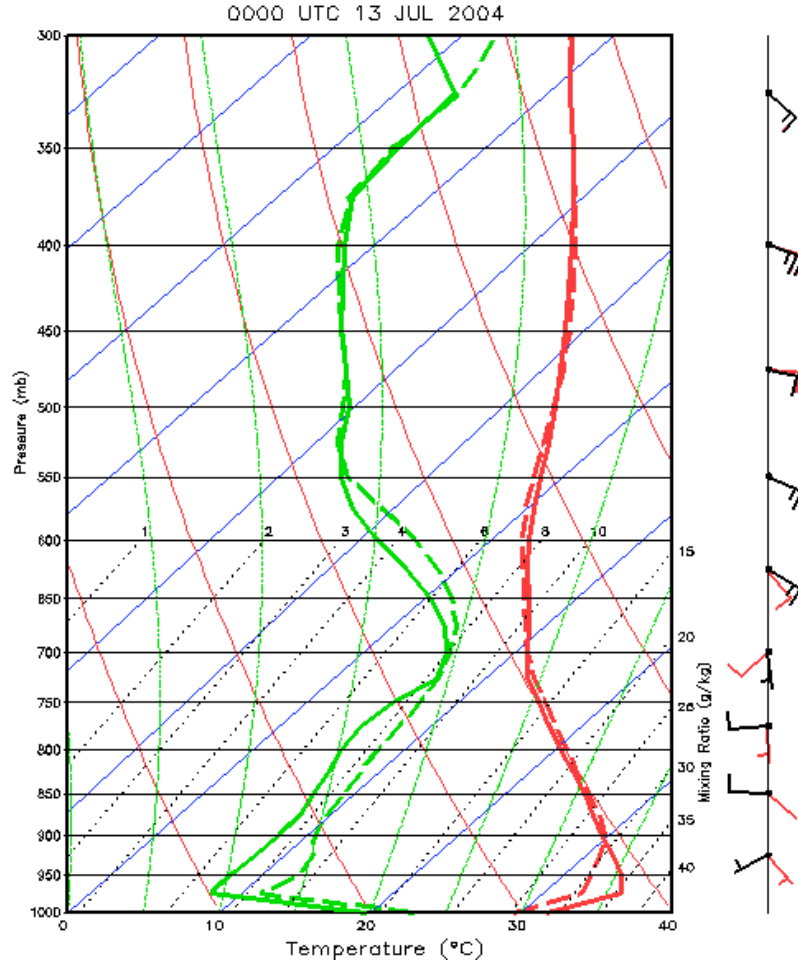


Figure 4.30. Model soundings from the control (solid lines, black wind barbs) and the No_gaps simulation (dashed lines, red wind barbs) for 30°N , 114°W at 00 UTC 13 July.

shunting effect from the Pacific inflow noted in the control run is not a necessary factor in surge initiation. There is weak Pacific inflow in the No_gaps run, so it is still possible that some may be required, just not as much as in the control run. At 08 UTC, the control and No_gaps surge events are still very similar in their location and maximum moisture flux values. The No_gaps run now has a larger area of greater than $150 \text{ g m kg}^{-1} \text{ s}^{-1}$ moisture flux values (Table 4.8) in the central GoC and higher moisture flux in the

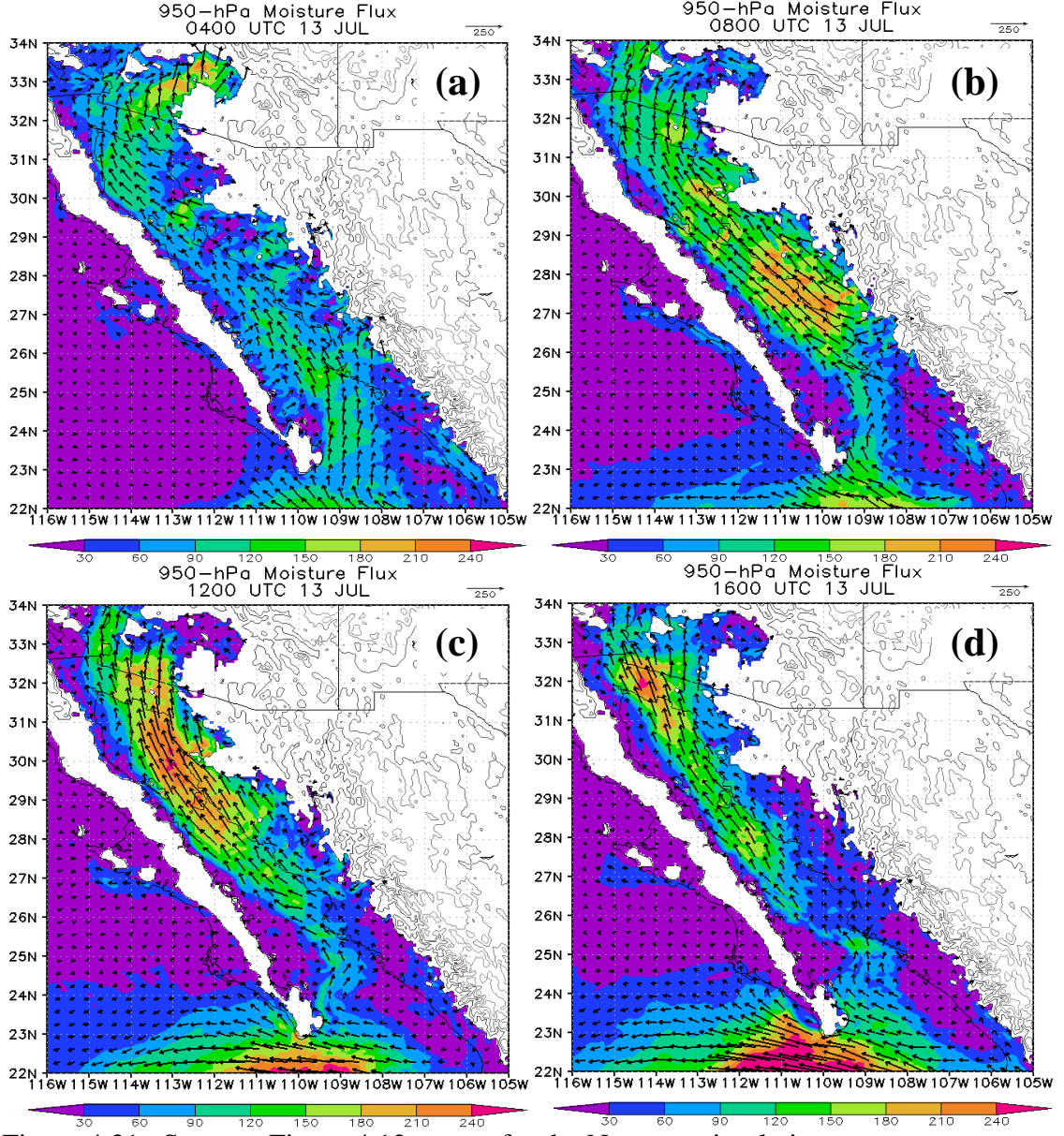


Figure 4.31. Same as Figure 4.12 except for the No_gaps simulation.

northern GoC due to the reduced Pacific inflow and stronger convective outflows associated with the more robust cold pools in the northern GoC (Fig. 28d). At 12 UTC the No_gaps surge is in a very similar location to the control run with similar maximum moisture flux values and a much larger area of greater than $150 \text{ g m kg}^{-1} \text{s}^{-1}$ moisture flux (Table 4.8). Finally, at 16 UTC the surge is more coherent and stronger north of the US/Mexico border (near 33°N) due to the lack of strong gap flows from the Pacific

introducing dry air. Performing the average wind magnitude analysis discussed in the No_SUBCLD run for the No_gaps run results in average wind magnitudes for the core surge time period of 7.7 m s^{-1} and 8.3 m s^{-1} for the control and No_gaps runs respectively. Analysis of wind profile time series for the No_gaps runs also confirms a more intense surge at PP (not shown).

Table 4.8. Area (km^2) with moisture flux values greater than $150 \text{ g m kg}^{-1} \text{ s}^{-1}$ for the No_gaps and control simulations at 08, 12, and 16 UTC 13 July.

	No_gaps	Control
08 UTC	55616	44544
12 UTC	76528	40560
16 UTC	26816	19440

3. Impacts of TUTT removal

a. Convection enhancement mechanisms

As discussed in Chapter 1, Tropical Upper Tropospheric Troughs (TUTTs) enhance precipitation and convection along the SMO during the NAM (Douglas and Englehart 2007; Bieda et al 2009; Finch and Johnson 2010). To further examine the proposed mechanisms of how this occurs (Pytlak et al. 2005; Finch and Johnson 2010), the use of a vorticity anomaly removal algorithm (see Chapter 2, section 2c) is made to remove the mid- and upper-level circulation associated with the TUTT during the 12-14 gulf surge event. Figure 4.32 shows the difference fields of temperature (a) and wind (b) for the control run with the TUTT (TUTT) and the TUTT removed (No_TUTT) simulations after six hours of integration. By 12 UTC 12 July

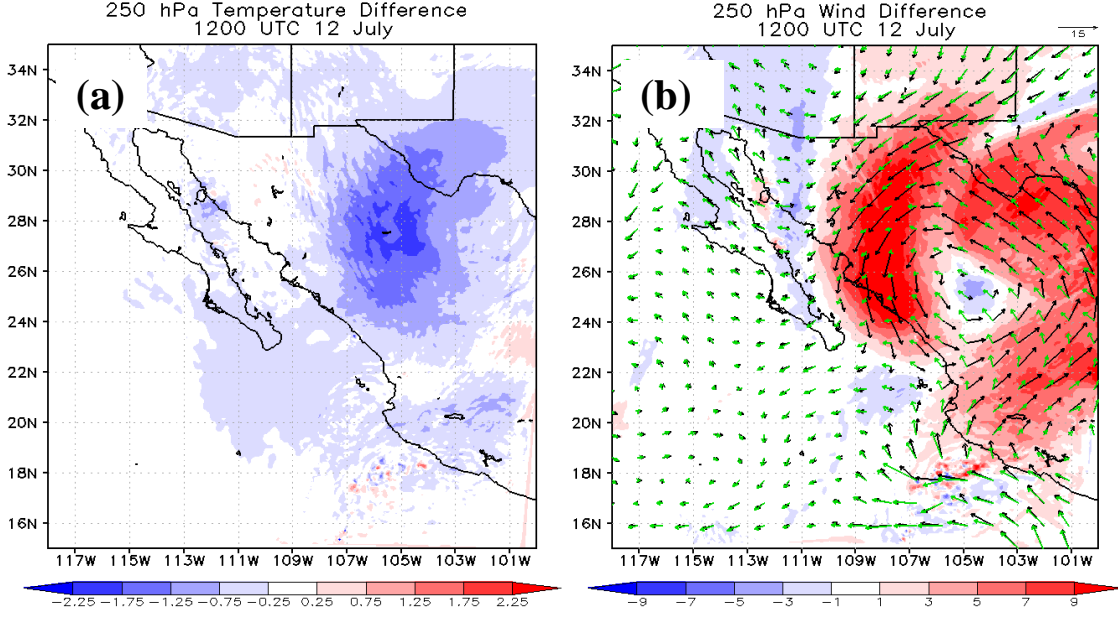


Figure 4.32. 250 hPa TUTT - No_TUTT temperature (K) (a) and wind differences (m s^{-1}) (b) at 12 UTC 12 July. The black vectors in (b) denote the TUTT wind while the green are for the No_TUTT simulation.

the simulated center has moved to near 25°N , 105°W as can be seen clearly in the wind differences (Fig 4.32b). The difference fields show the TUTT removal algorithm successfully removed the TUTT and most importantly, the 4 km simulations are able to successfully bring the TUTT circulation into the domain and sustain the distinct differences resulting from the TUTT removal.

1) DIVERGENCE MECHANISM

Prior studies of TUTTs locations outside the core NAM region found enhanced rising motion and precipitation generally on the eastern side of the circulation (Erickson 1971; Kelly and Mock 1982; Whitfield and Lyons 1992; Chen and Chou 1994). Pytlak et al. (2005) suggested that TUTTs in the NAM region have enhanced upper-level divergence in the northwest quadrant of the TUTT. However, Chen and Chou (1994) suggest that TUTTs with jet streaks in the northwest quadrant have “a classic” thermally

indirect secondary circulation in the jet streak exit region (Uccellini and Johnson 1979). The forecast-based conceptual model of Pytlak et al. (2005) indicates a jet streak exit region is located over the northwest quadrant of the TUTT, which would suggest sinking motion over the warm outer portions of the TUTT due to the thermally indirect secondary jet streak circulation. Finch and Johnson (2010) examined the TUTT modeled herein using the quasi-geostrophic (QG) omega equation and found QG-forced sinking motion in the 700 to 300 hPa layer to the west of the TUTT center when using the TUTT composite fields, which agrees with the TUTT studies outside the NAM region.

Figure 4.33 displays smoothed 300 hPa diffluence (Fig. 4.33a, b) and divergence (Fig. 4.33c, d) at 16 UTC 12 July for the TUTT and No_TUTT simulations. At 16 UTC, convection is in its incipient stages along the northern SMO. A coherent area of diffluence (red shading) is present in the TUTT simulation along 111°W over the northern SMO and GoC (24-34°N). In the No_TUTT simulation, the same general area of diffluence is present, but at about half the magnitude. Therefore, the TUTT seems to be responsible for added upper level diffluence over the northern SMO. However, the 300 hPa divergence displayed in Fig. 4.33c, d does not show coherent areas of divergence over the northern SMO in either simulation. Furthermore, both simulations have 400-200 hPa layer average downward vertical velocities over the northern SMO as seen in Figure 4.34. The TUTT simulation (Fig. 4.34a) has a larger area of greater than

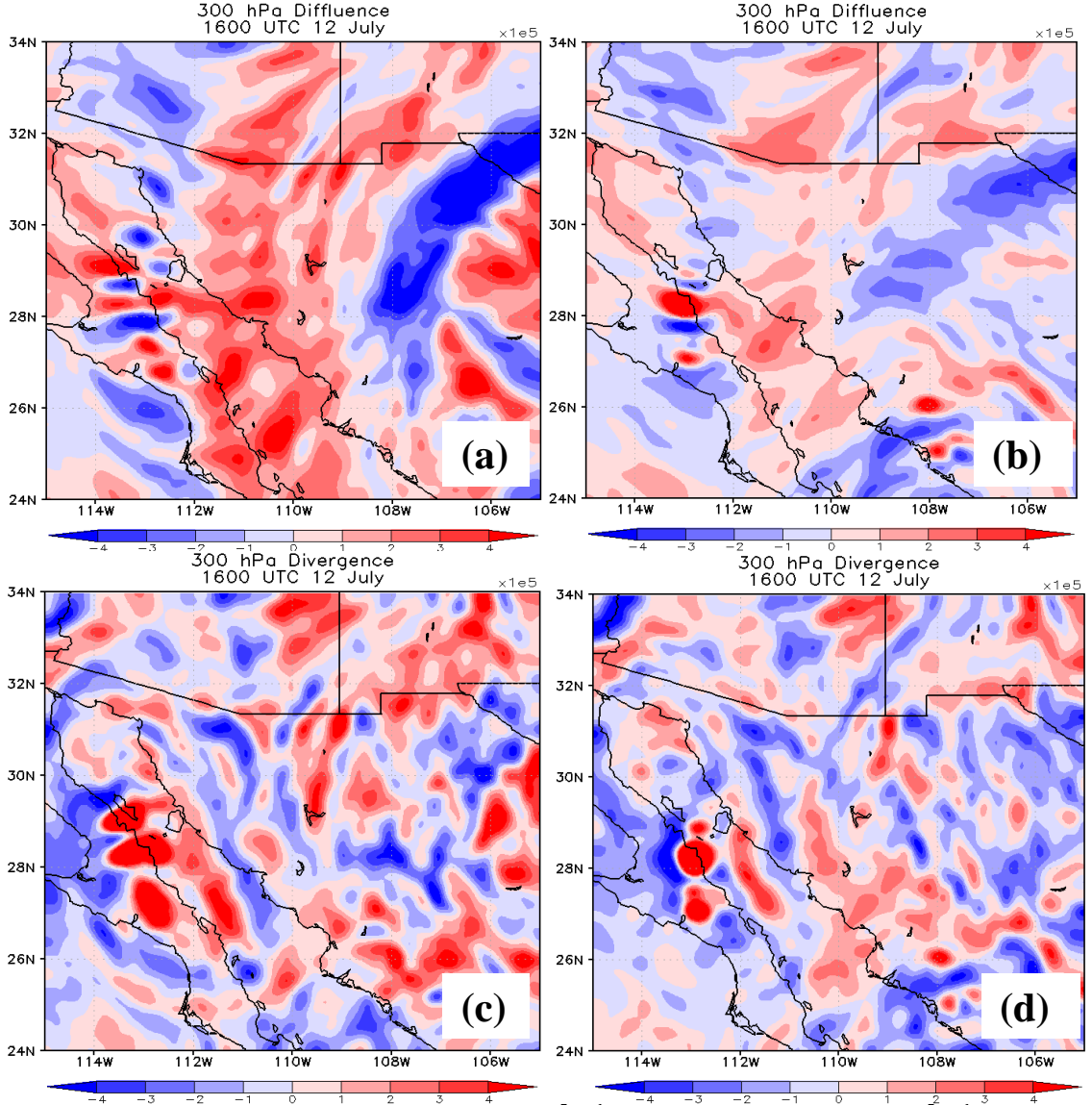


Figure 4.33. 300 hPa TUTT diffusence ($\times 10^{-5} \text{ s}^{-1}$) (a) and divergence ($\times 10^{-5} \text{ s}^{-1}$) (c), and No_TUTT diffusence (b) and divergence (d) at 16 UTC 12 July.

0.3 Pa s^{-1} omega values than the No_TUTT simulation (Fig. 4.34b). Between 700-400 hPa (Fig. 4.34c,d), both simulations have weak sinking motion over portions of the SMO with mountain circulations and incipient convection being represented by concentrated areas of more negative omega values. There is a period of weak 700-400 hPa uplift over the central and northern SMO (~14-1530 UTC) in the both simulations, which has shifted to between 32-34N by 16 UTC. The spatial pattern and magnitude of the area of

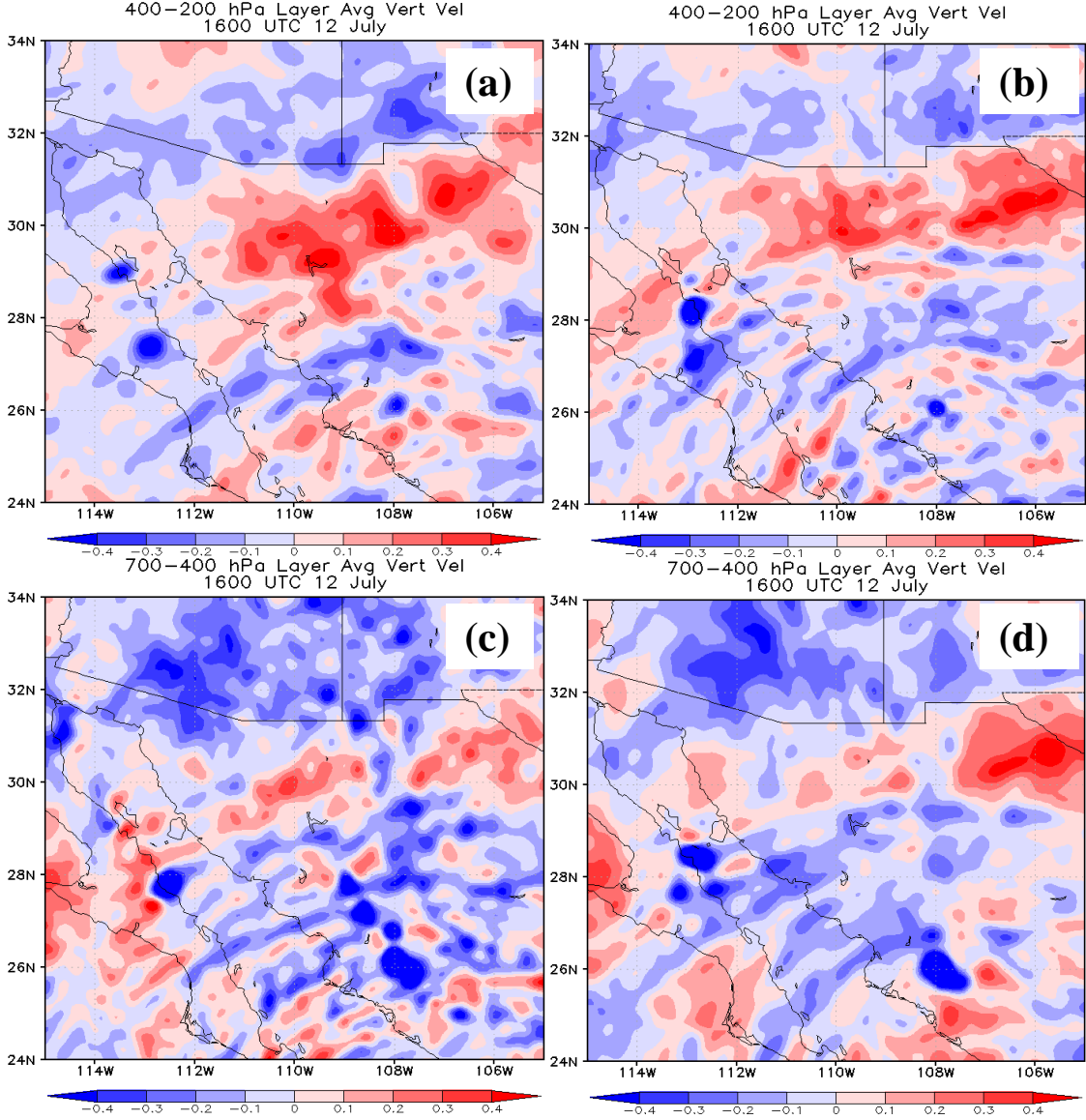


Figure 4.34. 400–200 hPa (a and b) and 700–400 (c and d) mass weighted vertical velocity (Pa s^{-1}) (negative upwards) for the TUTT (a,c) and No_TUTT simulations (b,d) at 16 UTC 12 July.

coherent rising motion are very similar however, suggesting TUTT influence in the mid-troposphere is minimal.

The TUTT simulation enhances diffluence in the northwest quadrant of the TUTT, which supports the assertion in Pytlak et al. (2005). However, Pytlak et al. (2005) further suggest this diffluence is associated with upper-level divergence and rising motion, which is not supported here. The divergence pattern is disorganized in the

northwest quadrant of the TUTT with no clear association of divergence with the diffluent area. Enhanced upper-level sinking motion to the northwest of the TUTT, over the northern SMO, just before and during convective initiation is present in the TUTT simulation as well. Therefore, another mechanism must be responsible for the enhanced precipitation and convection over the SMO when a TUTT is present to the west of the SMO axis, in agreement with Finch and Johnson (2010).

2) SHEAR MECHANISM

Finch and Johnson (2010) found that there is a correlation between enhanced convection along the SMO and the 700-400 hPa mean flow and bulk shear. They show that areas with enhanced 700-400 hPa mean flow and bulk shear have colder cloud tops and enlarged canopy areas (their Fig. 11 and 12). They propose the changes in the midlevel flow create a more favorable environment for convection to organize, move off the SMO and persist longer than on non-TUTT days. Lang et al. (2007) suggest days with increased shear in the NAM have increased convective organization through cold pool/shear interaction described by Rotunno et al. (1988). This interaction considers horizontal vorticity between the updraft vorticity; cold pool vorticity and environmental vorticity (Weisman and Rotunno 2004). As the vorticity contributions become more balanced, the updraft becomes more upright and stronger. Also, Weisman and Rotunno (2004) show that for increasing surface based or elevated shear, squall systems produce more rainfall and have larger maximum vertical velocities. The most drastic increases in precipitation generally occur when small shear magnitudes are increased, rather than cases having large shear magnitudes increasing further (Weisman and Rotunno 2004).

Figure 4.35 shows the 700-400 hPa (a) and the Sfc- 500 hPa (b) difference fields for bulk shear at 16 UTC 12 July. The TUTT simulation has a large area of increased 700-400 hPa bulk shear (red shading). The TUTT simulation generally has $1-5 \text{ m s}^{-1}$ more 700-400 hPa bulk shear with areas between 26 and 28°N having up to 9 m s^{-1} more

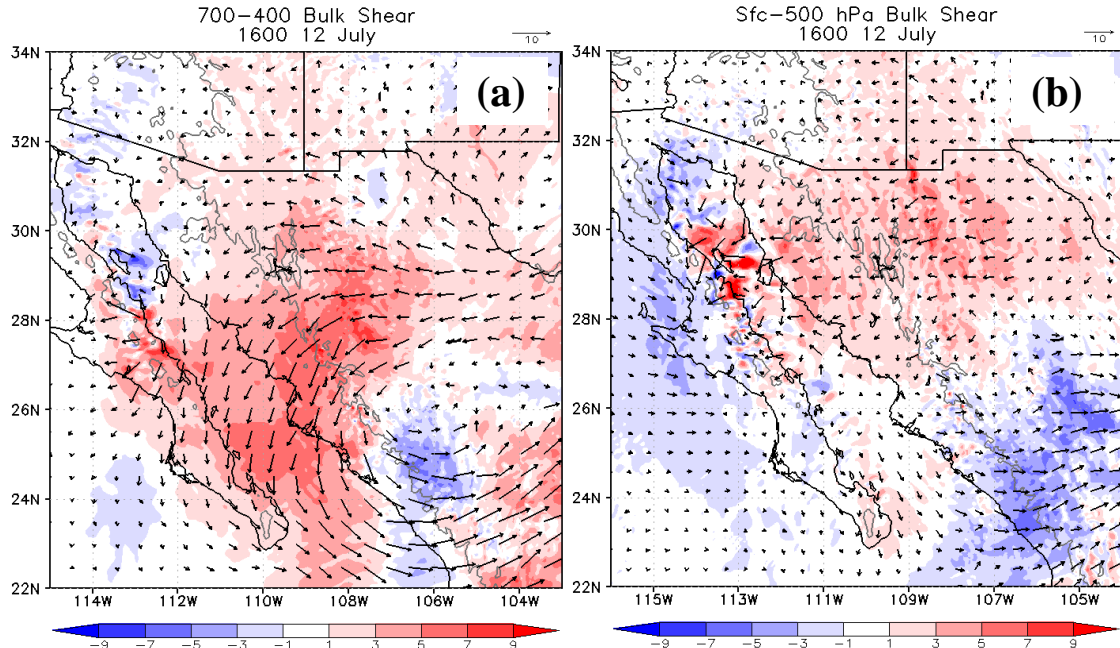


Figure 4.35. TUTT – No_TUTT 700-400 hPa (a) and Sfc-500 hPa (b) bulk shear (m s^{-1}). The black and green arrows in (a) denote the TUTT and No_TUTT simulations respectively. The black arrows in (b) display the shear difference vector. The light gray contour denotes the 750 m terrain elevation in both.

shear. These values are very similar to those of Finch and Johnson (2010) at 00 UTC 13 July when comparing to the mean NAME flow. The 700-400 hPa shear vectors in the TUTT simulation are also more perpendicular to the SMO in the same region (Fig. 4.35a). The TUTT simulation also has Sfc-500 hPa shear increases of $1-5 \text{ m s}^{-1}$ (red shading, Fig. 4.35b) over the northern SMO during convective initiation and propagation on 12-13 July. The Sfc-500 hPa shear vector is again generally more perpendicular to the SMO in the TUTT simulation. This suggests the environment is more favorable for convective organization and propagation, from a shear standpoint, in the northern SMO

in the TUTT simulation (Smith and Gall 1989; Farfán and Zehnder 1994; Weisman and Rotunno 2004; Lang et al. 2007). Over the northern SMO between 28 and 32°N, the TUTT simulation also has increased 700-400 hPa mean flow of up to 2 m s^{-1} which would, in most cases, also increase storm motion and propagation off the SMO (Byers and Braham 1949; Chappell 1986; Corfidi 2003).

(i) Thermodynamic considerations

To rule out thermodynamic changes as the convective enhancement mechanism, sounding analysis at two coastal sites (LM and KB) was performed by Finch and Johnson (2010). They argue that there are insignificant changes in CAPE related to the TUTT and show that nearly all CAPE changes over the life of the TUTT at these two sites are related to near surface moisture changes associated with the gulf surge event. However, they do note that slight mid-level cooling took place between 12-13 July at the two sites, which produced the minor changes in CAPE they associated with the TUTT. Figure 4.36 displays mass-weighted difference fields for potential temperature (a), specific humidity (b), wind (c), and the difference in 90 hPa mixed layer CAPE (d) at 16 UTC 12 July between the surface and 850 hPa. The largest magnitude differences for all fields are found over the GoC and Baja Peninsula and are due to slight differences in convective evolution early in the simulations. There is observed convection present along the GoC coast near the simulated convection between 06-09 UTC 12 July ($\sim 28^\circ\text{N}, 111^\circ\text{W}$) (not shown). The convective influences on the difference fields appear to be minimal along the SMO as evidenced by the smaller difference magnitudes in all fields and from examination of the time evolution of the difference fields near the SMO (not shown). By 16 UTC 12 July the simulations have minimal potential temperature differences with the

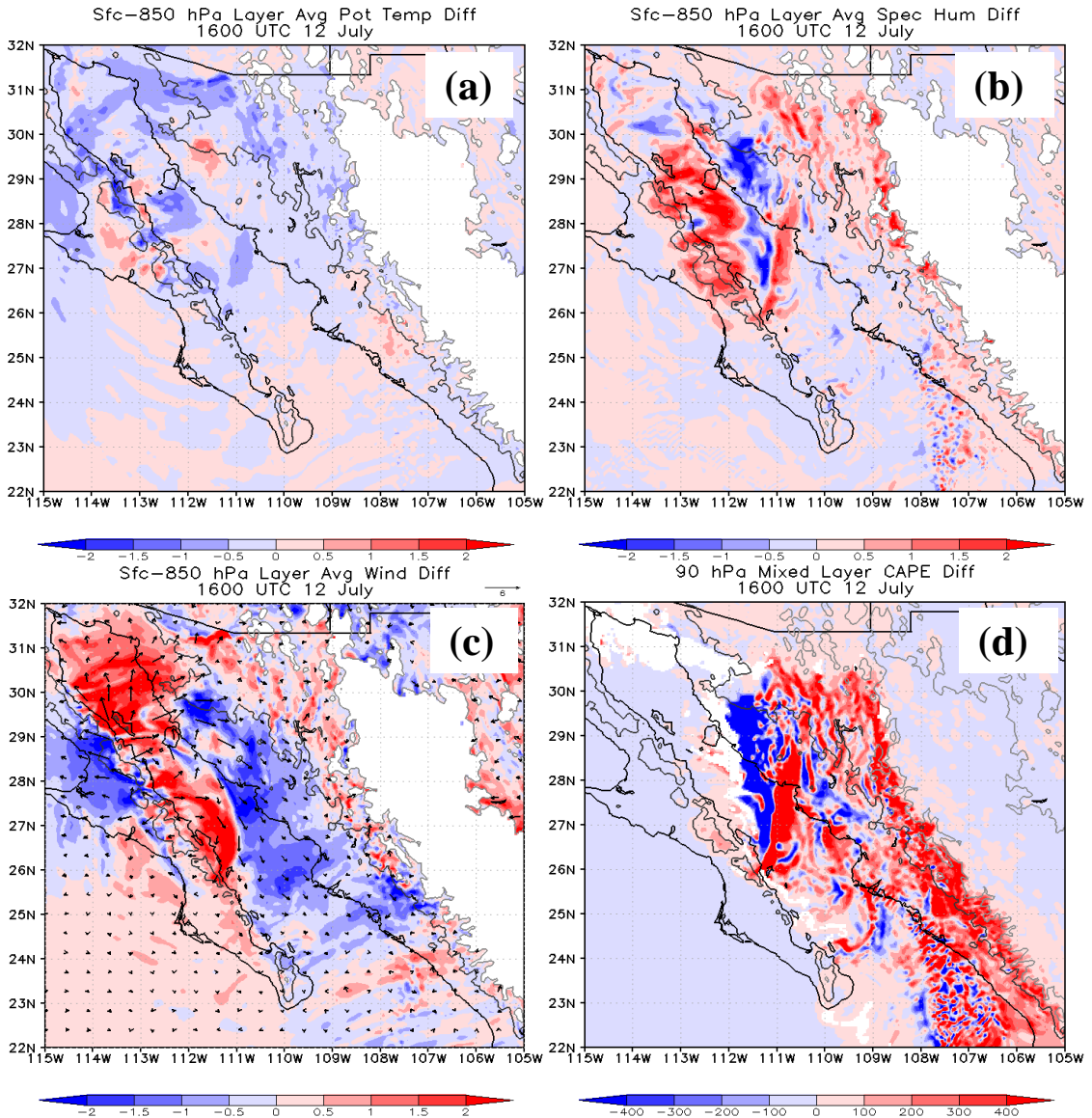


Figure 4.36. TUTT – No_TUTT Sfc-850 hPa mass weighted potential temperature (K) (a), specific humidity (g kg^{-1}) (b), wind (m s^{-1}) (c), and the lowest 90 hPa mixed layer CAPE (J kg^{-1}) in (d). The three black/gray contours denote the 0, 500 and 1500 m terrain contours (lighter is higher). White areas in (a)-(c) denote areas above 850 hPa, while in (d) they denote areas with mixed layer convective inhibition greater than 200 J kg^{-1} .

No_TUTT being around 0.5 K warmer in the lowest 150 hPa along the northern SMO ($28\text{-}31^\circ\text{N}$, $108\text{-}111^\circ\text{W}$). The TUTT simulation has slightly less moisture along the coastal plain but more moisture above 500m along the SMO, especially in the northern SMO ($29\text{-}31^\circ\text{N}$, $108\text{-}111^\circ\text{W}$). The latter is due to the TUTT simulation having slightly

stronger low-level flow directed into the SMO before 16 UTC. The No_TUTT simulation has slightly stronger low-level flow, but the TUTT simulation wind vectors are slightly more perpendicular to the SMO at 16 UTC. The increased flow in the No_TUTT simulation may be a result of more surface heating and sensible heat flux in that simulation due to the drier air at higher elevations, creating a slightly stronger mountain solenoid circulation along the ridge at 30°N. A similar response was seen in the special NAME NARR, which exhibited a surface dry bias (Ciesielski and Johnson 2008).

The most interesting of the fields in Fig. 4.36 is the lowest 90 hPa mixed layer CAPE difference field. At 16 UTC the TUTT simulation has consistently higher CAPE, up to several hundred J kg^{-1} , over most of the higher elevations along the SMO. The CAPE differences are primarily due to increased low-level moisture in the northern SMO (28-31°N, 111-108°W) and mid- to upper-level cooling along the central and southern SMO (22-27°N, 105-109°W). The central and southern SMO are much closer to the TUTT center at this time where the largest differences in mid- and upper-level temperatures reside. Figure 4.37 gives an example sounding from the northern SMO (30°N, 110°W) to highlight the slight differences in the temperature and moisture between the TUTT and No_TUTT simulations. The TUTT simulation sounding has 115 J kg^{-1} more CAPE. The parcel trajectories are nearly identical (not shown) with the TUTT simulation having a slightly lower lifted condensation level (LCL) and warmer cloud base. This combined with the small temperature differences results in the CAPE difference.

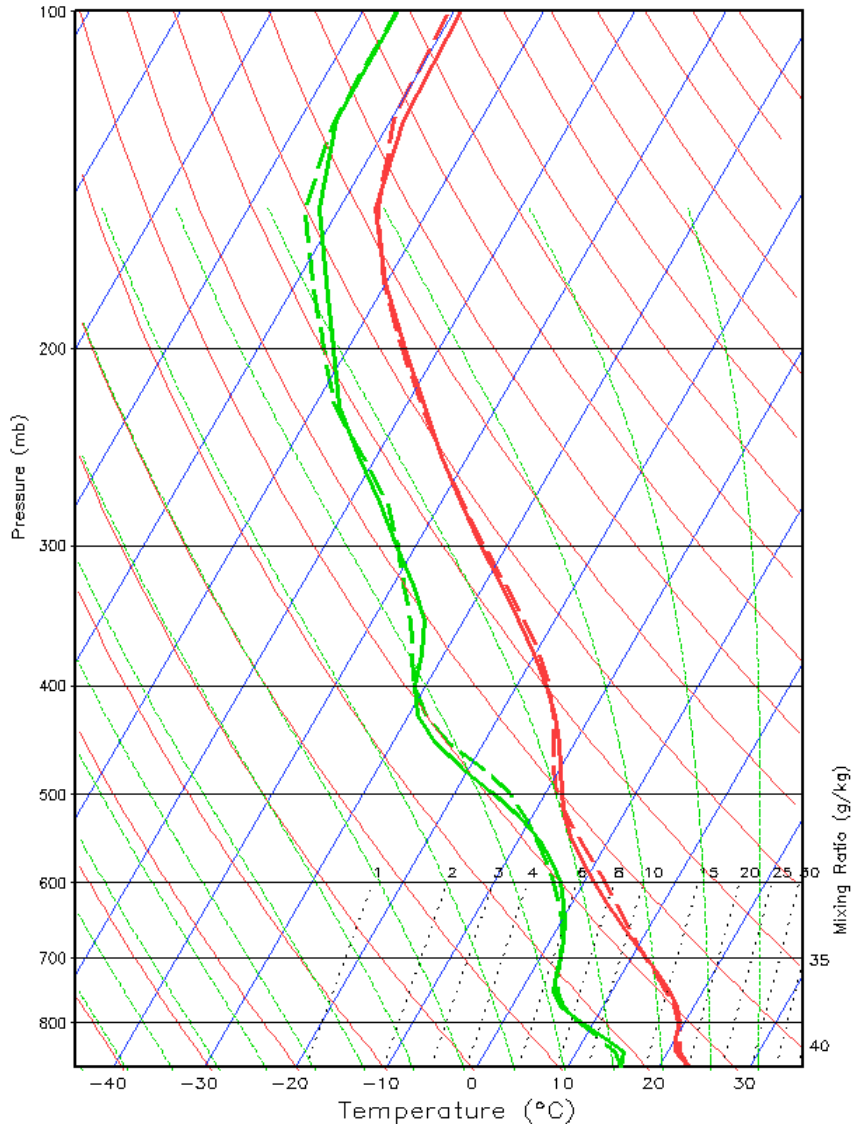


Figure 4.37. TUTT (solid) and No_TUTT (dashed) temperature ($^{\circ}\text{C}$) (red) and dew point ($^{\circ}\text{C}$) (green) sounding for 30°N , 110°W at 16 UTC 12 July. Wind barbs follow standard convention (knots) with black and red for the TUTT and No_TUTT simulations respectively.

While Finch and Johnson (2010) indicate that there are no significant CAPE differences related to the TUTT at the two coastal sites, they do find slight mid- and upper-level cooling. This cooling would be expected to be greater along the SMO, closer to the TUTT center. There may also be unobserved moisture differences (NAME soundings are along the coast and east of the SMO crest) attributable to the TUTT along

the complex terrain of the SMO foothills as well. Only slight differences in the lowest 150 hPa mean flow in these simulations result in moisture differences of up to 2 g kg^{-1} in certain valleys. These slight differences in temperature, moisture and the resultant CAPE are more significant in areas of less CAPE, like the SMO foothills, and could be significant in the initial microphysical and subsequent convective cluster evolution.

3) COMBINED MECHANISM

The subtle changes in CAPE during convective initiation result in larger vertical velocities in the nascent convective elements for the TUTT simulation. Figure 4.38 shows a time series of average vertical velocity for all grid points and model levels having $w > 1 \text{ m s}^{-1}$ along the SMO between 22 and 32°N for both simulations, while Figure 4.39 shows the difference field of vertical velocity for the two simulations from 16 UTC 12 July to 00 UTC 13 July. The 1 m s^{-1} threshold was used as a quick way to average only grid points with strong updrafts. It is evident that in the TUTT simulation, deep convection begins in earnest by 17 UTC with a rapid increase in positive vertical velocities in the mid- to upper-troposphere. The No_TUTT simulation has an initial increase near the same time, but average vertical velocities greater than 2 m s^{-1} do not occur above 8000 m AGL until after 1930 UTC. CAPE can be used as an upper bound for vertical velocity from parcel theory (Crook 1996). This assumption neglects many processes such as precipitation loading, entrainment of drier air, etc, but there is a strong correlation between CAPE and observed vertical velocity (Crook 1996). In the initial stages of convection, shear imposes a mean drag on convective elements due to the increased entrainment of drier, less energetic air into the updraft (Cotton et al. 2010). This reasoning implies the TUTT simulation should have weaker initial updrafts as

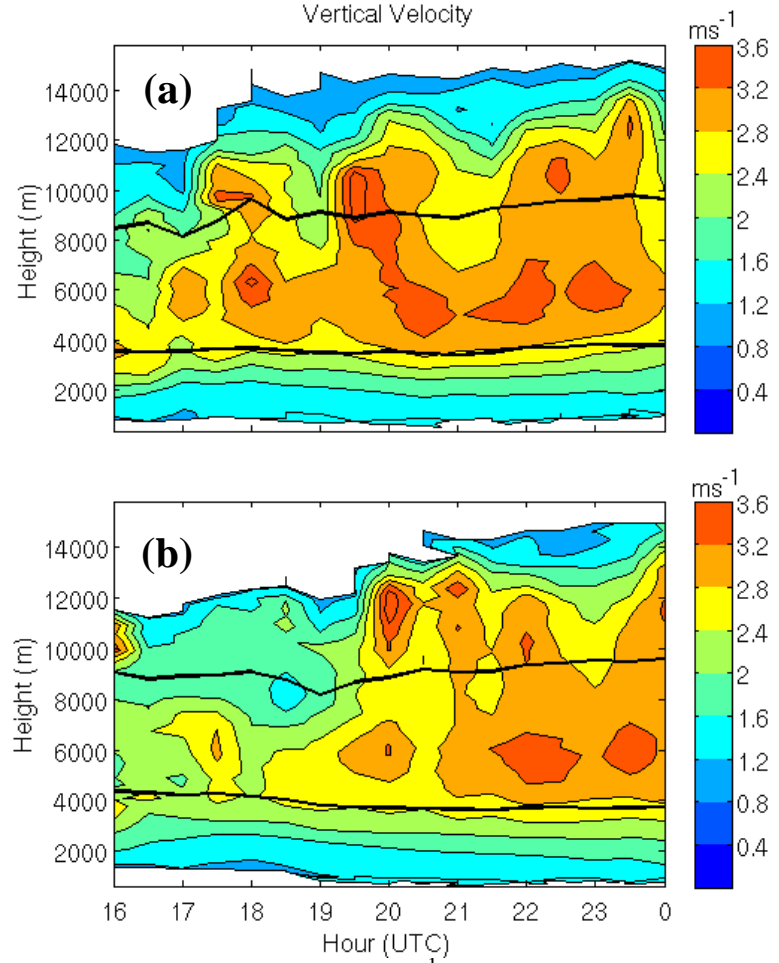


Figure 4.38. Average vertical velocity (m s^{-1}) for the TUTT (a) and No_TUTT (b) simulations with all grid points and model levels having $w > 1 \text{ m s}^{-1}$ along the SMO between 22 and 32°N . The two black contours denote the 0°C (lower) and -20°C (upper) average isotherms. All heights are AGL.

compared to the No_TUTT simulation given equal CAPE. However, as shown in Fig. 4.39, the TUTT simulation has stronger average vertical velocities from the outset in an environment with slightly stronger shear and larger CAPE at a time when precipitation loading should be minimal in both simulations. This finding suggests that the increased CAPE is largely responsible for the increased convective vigor in the TUTT simulation for possibly the first couple hours of convective development.

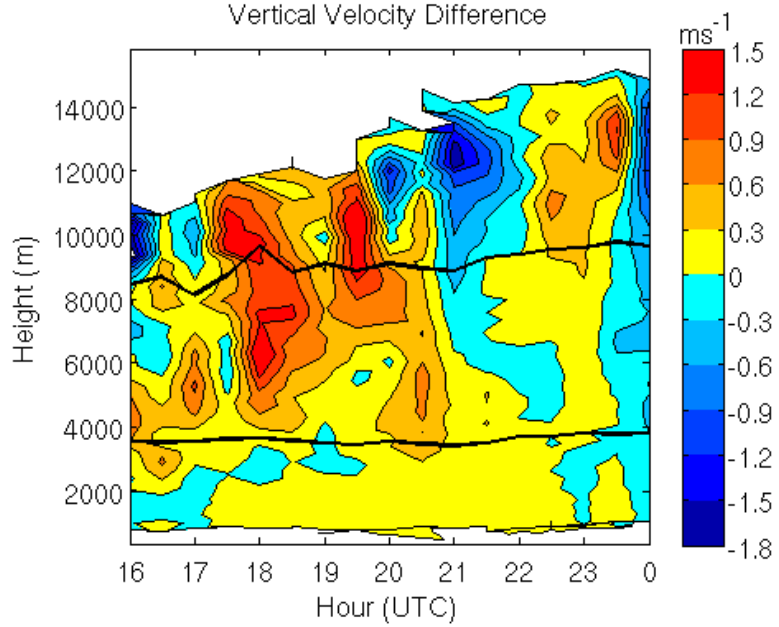


Figure 4.39. Same as Figure 4.38, except for the vertical velocity differences, TUTT – No_TUTT.

After the initial convective development, shear becomes important in organizing and maintaining convection (Rotunno et al. 1988; Weisman and Rotunno 2004). The northern SMO has enhanced shear along the northern SMO (Fig. 4.35) and stronger 700–400 hPa mean flow perpendicular to the SMO in the TUTT simulation. If the shear is helping to sustain and organize convection, that region should experience more total rainfall than the No_TUTT simulation (Weisman and Rotunno 2004; Bryan et al. 2006) and have more precipitation farther from the SMO due to the enhanced mean flow “steering” convection farther off the SMO (Chappell 1986; Corfidi 2003). Figure 4.40 displays the accumulated precipitation difference field for the time period 18 UTC 12 July – 12 UTC 13 July. This period extends from just after convective initiation through complete dissipation over the northern SMO. The southern boundary at 28°N corresponds with the southern boundary of the lightning analysis performed in Bieda et

al. (2009). The TUTT simulation produces more precipitation in this region, especially in the lower terrain.

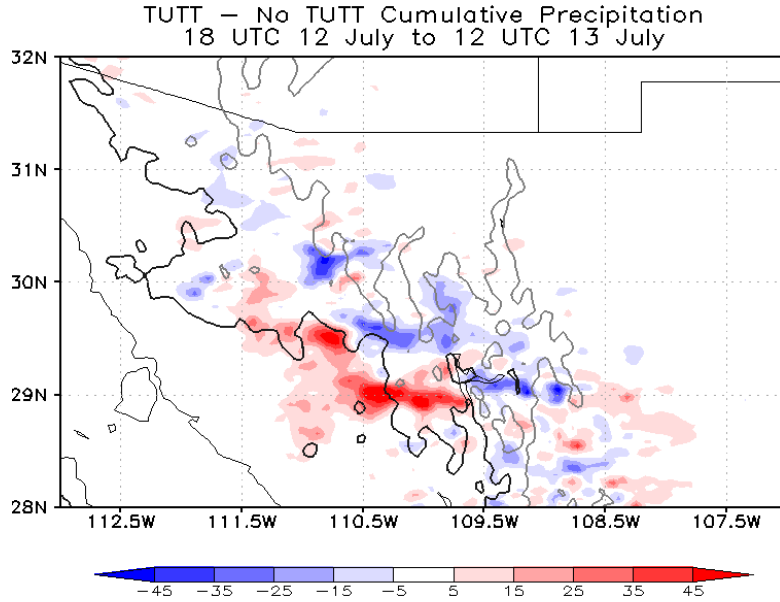


Figure 4.40. TUTT – No_TUTT cumulative precipitation differences between 18 UTC 12 July and 12 UTC 13 July in mm. The narrow black contour denotes 0 m terrain height, along with 500 m (thick black) and 1000 m (gray).

Table 4.9 gives the total precipitation for the region for each simulation, and the total precipitation broken down into three categories distinguished by terrain height: low, middle and high. The high terrain is defined by areas greater than 1000 m, the middle is set at 500 to 1000 m and the low is below 500 m. This breakdown gives a more quantitative view of the ability of convection to propagate off the high peaks. Overall, the TUTT simulation produces 23% more precipitation than the No_TUTT simulation. For the three (low to high) terrain ranges, the TUTT simulation produces 431% more, 14% less, and 18% more precipitation respectively. The changes in the percent differences strongly suggest the TUTT simulated convection propagates more strongly off the SMO. The TUTT simulation produces more precipitation at higher elevations, but less at middle elevations.

The conclusion drawn from these simulations is that the No_TUTT simulation produces slightly less initial convection, that convection does not propagate as fast toward the lower terrain, and precipitates heaviest over the slopes of the SMO. When reaching the low terrain, the No_TUTT simulated convection decays away while the TUTT convection continues westward. Examination of simulated reflectivity (not shown) finds that the TUTT simulation has more short line segments versus individual convective elements which propagate farther west.

Table 4.9. Total precipitation (kg) between 18 UTC 12 July and 12 UTC 13 July for the TUTT and No_TUTT simulations in the region defined by Fig. 4.40.

	Low	Middle	High	Total
TUTT	7.43×10^{14}	1.21×10^{15}	1.74×10^{15}	3.69×10^{15}
No_TUTT	1.40×10^{14}	1.40×10^{15}	1.47×10^{15}	3.01×10^{15}

4) MICROPHYSICAL ASPECTS

With differing initial CAPE and shear profiles, it is likely that the microphysics of convection in the two simulations differ, and potentially in significant ways. Figures 4.38 and 4.39 show that convection in the TUTT simulation is more vigorous for the first few hours, and the result is similar when examining only the northern SMO. Besides enhancing precipitation, the analysis of Bieda et al. (2009) shows that TUTTs modify the National Lightning Detection Network (NLDN) (Cummins et al. 1998) cloud-to-ground (CG) lightning climatology in the northern SMO, north of 28°N. When a TUTT passage occurs, there are more CG strikes along the northern SMO than on non-TUTT days (Bieda et al. 2009). One conclusion would be that since there is more organized convection and more precipitation there would naturally be more CG lightning. It is also

possible that microphysical differences between the storms influenced by a TUTT further enhance CG lightning strikes.

It is generally agreed that ice processes are critical to the electrification of a thunderstorm and eventual lightning production (Workman and Reynolds 1949; Reynolds et al. 1957; Takahashi 1978; Williams and Lhermitte 1983; Dye et al. 1989; Saunders et al. 1991; Carey and Rutledge 1996; Blyth et al. 2001; Petersen and Rutledge 2001). This effect occurs through the non-inductive charging process, which occurs in the mixed-phase portion of the cloud. Ice crystals and growing graupel particle collisions impart different charges on each particle. Furthermore, differential transport by the storm updraft due to terminal velocity differences creates the typical dominant dipole charge structure (positive upper, negative middle) seen in thunderstorms. The lower weak positive region, which completes the usual tripole structure, is thought to be created by additional gravitational sedimentation and size sorting of precipitation particles and is a consequence of the non-inductive charging mechanism (Wiens et al. 2005).

Due to the likely importance of ice in thunderstorm charging, some recent observational work has examined the relationship between ice content or flux and lightning flash rates. This work has found a strong correlation between precipitation ice mass and CG and total lightning (CG plus intracloud lightning) (Nesbitt et al. 2000; Petersen and Rutledge 2001; Deierling et al. 2005; Petersen et al. 2005; Wiens et al. 2005; Latham et al. 2007). Other modeling and observational work has found that lightning production is also strongly correlated with downward fluxes of graupel and the upward flux of ice crystals in the mixed phase region (Blyth et al. 2001; Latham et al. 2004; Deierling et al. 2008). Specifically of interest to this study, Wiens et al. (2005),

Kuhlman et al. (2006) and Deierling et al. (2008) show a strong correlation between graupel volume and total and CG lightning.

Figure 4.41 displays the fraction of total condensate for the graupel, snow, and cloud water hydrometeor classes produced by the Thompson two moment microphysics scheme (Thompson et al. 2008) along with the areal average integrated condensate for all grid

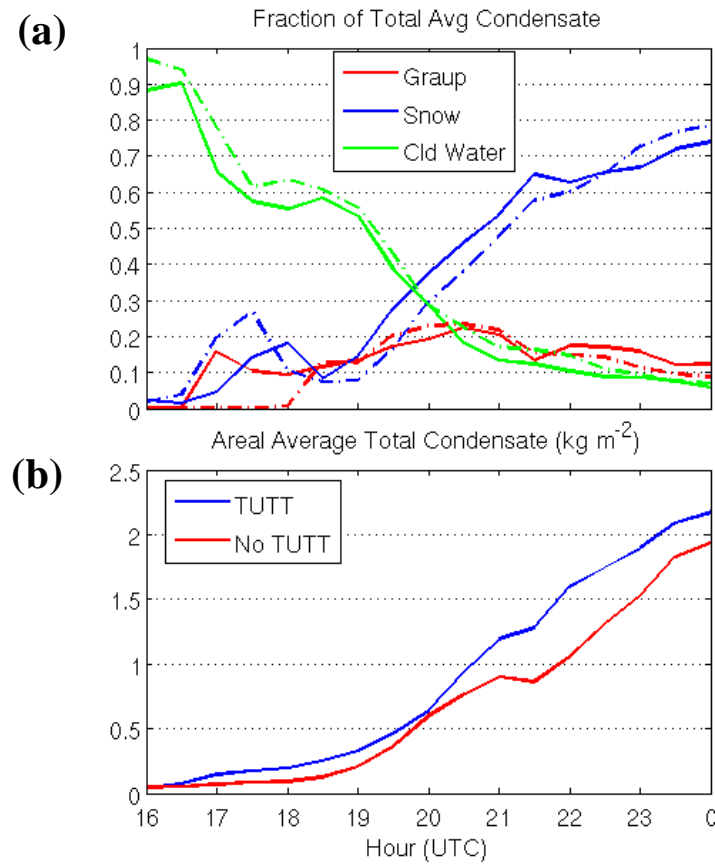


Figure 4.41. For all grid points with condensate between 28 and 33°N along the SMO, (a) shows the fraction of vertically integrated average condensate for graupel, snow and cloud water hydrometeor classes (TUTT is solid and No_TUTT is dashed) and (b) shows the total average vertically integrated condensate (kg m^{-2}). For the time period 16 UTC 12 July to 00 UTC 13 July.

points with condensate for the region shown in Fig. 4.40, 28-32°N, 113-107°W. Graupel is formed nearly immediately in the TUTT simulation, while more snow (blue dashed line) is generated in the No_TUTT simulation. Graupel forms primarily through riming

of snow crystals in nature and the microphysics scheme (Magono 1953; Weickmann 1953; Knight and Knight 1973; Reinking 1975; Thompson et al. 2008), therefore this indicates more riming is occurring in the TUTT simulation. This would account for the decreased cloud water in the TUTT simulation through about 19 UTC. The fractional graupel totals remain higher in the TUTT run until around 1830 UTC. Fractional snow amounts decrease in the No_TUTT simulation around 18 UTC, when graupel begins to form and mean updraft strengths in the mixed layer increase (Fig. 4.38). Fractional amounts for cloud ice are not shown due to their extremely low values throughout the simulation, less than 1% of the total condensate mass. This is a function of their small size and low density. The TUTT simulation does have more total cloud ice mass than the No_TUTT simulation throughout the period (not shown).

Similar to Figures 4.38 and 4.39, Figures 4.42 and 4.43 display the mean graupel mixing ratio for grid points having vertical velocities greater than 1 m s^{-1} , except only over the northern SMO between $28\text{-}32^\circ\text{N}$, $113\text{-}107^\circ\text{W}$. It is evident that the TUTT simulation generates more graupel before and more graupel overall than the No_TUTT simulation. The two thick black lines on the figures denote the 0°C and -20°C average isotherms. Focusing on just this layer, an estimate of the “charging layer” (Latham et al. 2004; Deierling et al. 2008), it is clear the TUTT simulation has much more graupel in this layer than the No_TUTT simulation through 00 UTC 13 July. After 01 UTC 13 July, the No_TUTT simulation begins to have larger average graupel mixing ratios (not shown) and more total graupel mass as seen in Figure 4.44a. However, the TUTT simulation has more cumulative graupel mass for the entire time period of 16 UTC 12 July – 10 UTC 13 July (not shown). The TUTT simulation also has more supercooled

water mass (Figure 4.44b) than the No_TUTT run through 02 UTC 13 July and more cumulative supercooled water mass (not shown).

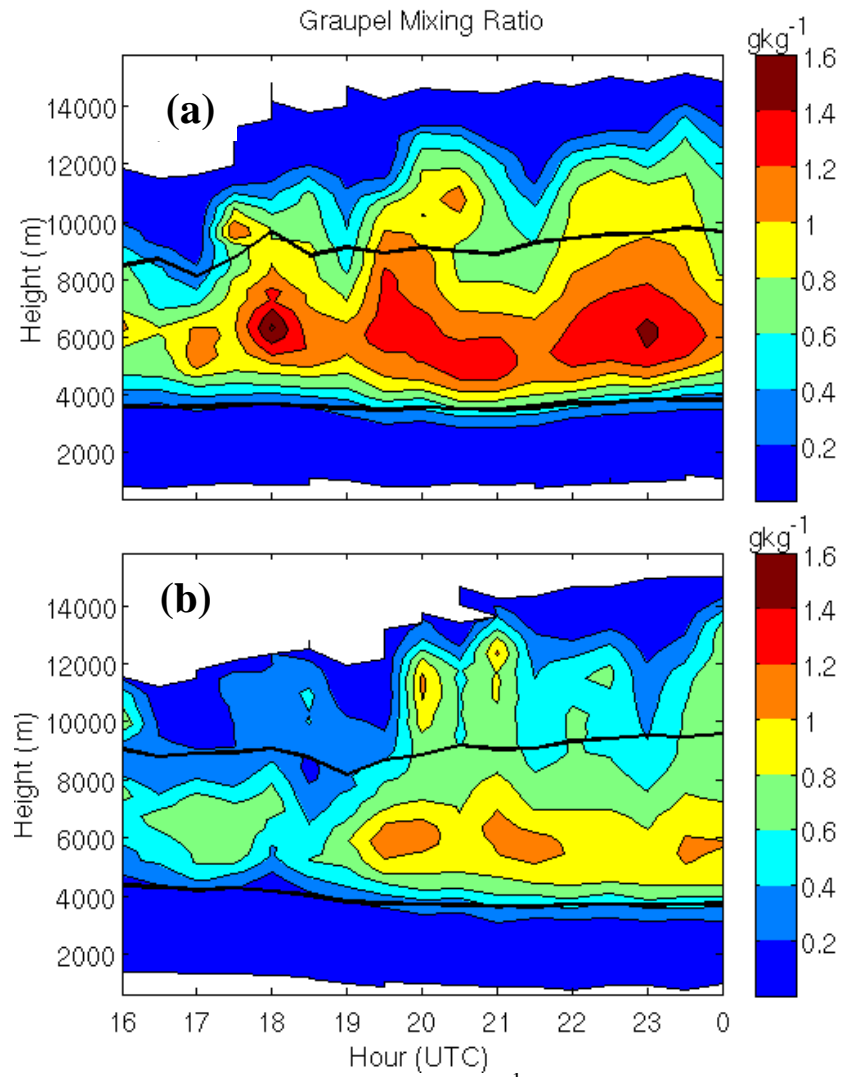


Figure 4.42. Average graupel mixing ratios (g kg^{-1}) for the TUTT (a) and No_TUTT (b) simulations using the same guidelines as Figure 4.41 for 16 UTC 12 July to 00 UTC 13 July. Again the two black contours denote 0°C (lower) and -20°C (upper)

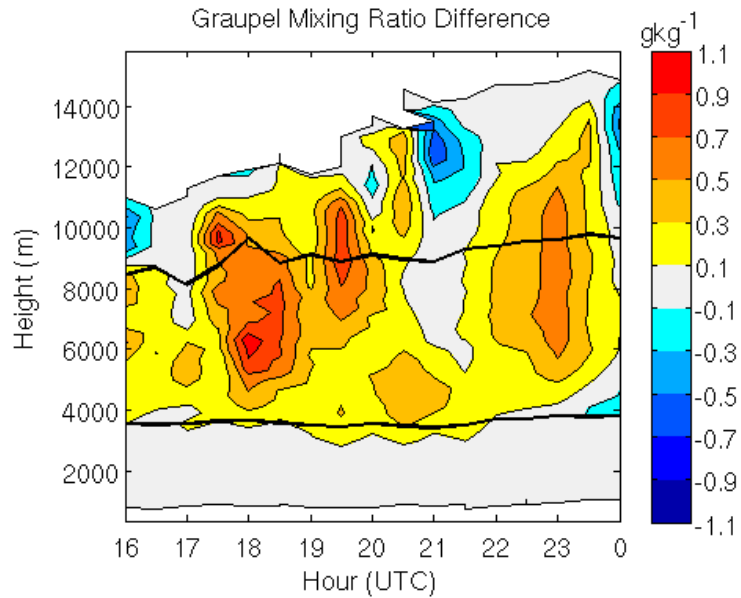


Figure 4.43. Same as Figure 4.42 except for the difference field, TUTT-No_TUTT.

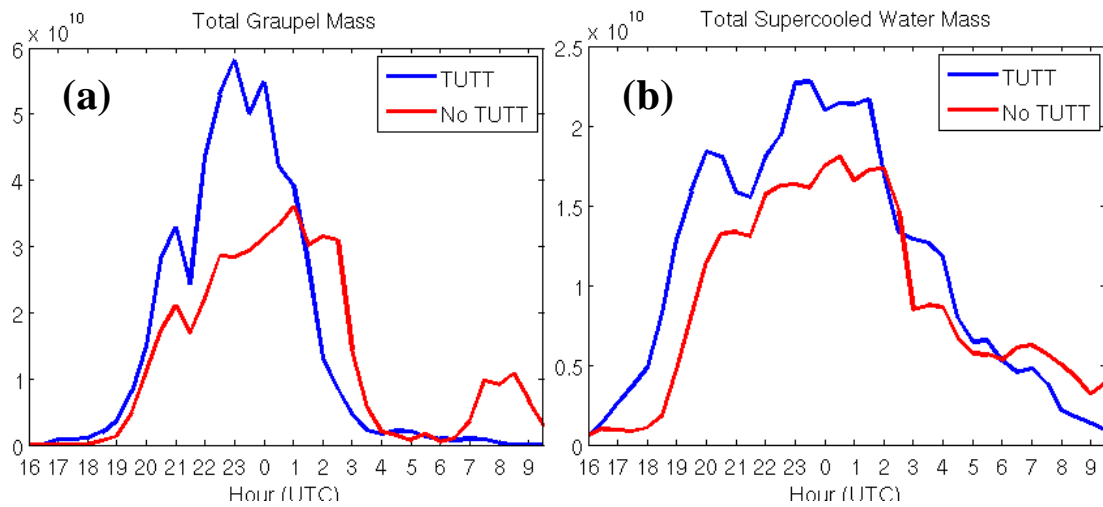


Figure 4.44. Total graupel (a) and supercooled water (b) mass (kg) for the TUTT (blue) and No_TUTT (red) simulations between 16 UTC 12 July and 0930 UTC 13 July.

Due to these simulations being performed at 4 km horizontal resolution, likely producing updrafts that are too broad and weak (Bryan et al. 2003; Bryan and Morrison 2011) no effort is made to produce quantitative graupel and ice mass fluxes and corresponding estimated lightning counts. Qualitatively, the TUTT simulation has more graupel, more cloud ice and more supercooled liquid water mass throughout most of the

16 UTC 12 July – 10 UTC 13 July and larger cumulative masses of those three particle species. Figure 4.43 shows there is more graupel in the charging zone for the TUTT simulation. Increased charging zone graupel combined with more cloud ice and supercooled liquid water mass, and stronger mean updrafts, would strongly suggest a more vigorous non-inductive charging mechanism in the TUTT simulation (Latham et al. 2004; Deierling et al. 2008). This should increase total and CG lightning counts.

It is possible to have increasing graupel and cloud ice mass fluxes without a corresponding increase in CG lightning (MacGorman et al. 1989; Tessendorf et al. 2007). MacGorman et al. (1989) propose that kinematically strong thunderstorms have “elevated charge” layers. That is to say the dominant positive and negative dipole charge layers are farther from the ground in storms with very strong updrafts, like supercells, which results in reduced CG lightning. Tessendorf et al. (2007) examined a low precipitation supercell that had no CG strikes throughout its lifecycle. They attribute this to a dearth of hydrometeors falling out of the storm, and the resultant lack of the weak low charge layer and the completed tripole that may be necessary for CG lightning production. The storm examined by Tessendorf et al. (2007) also showed some evidence of elevated charge layers in areas near the core of the updraft.

These special cases that do not have increased CG lightning with increasing graupel/cloud ice mass likely do not occur frequently in the SMO region for several reasons. The storms studied by MacGorman et al. (1989) and Tessendof et al. (2007) were supercell thunderstorms. These storms typically have larger values of shear than observed in the core NAM region (Rasmussen and Blanchard 1998; Lang et al. 2007). Manual examination of NAME radar composite images showed mostly cellular and

clustered convection with some line segments with very few if any long lived “supercell like” thunderstorms. The areas of broad, strong updraft greater than 20 m s^{-1} in these storms created an elevated charge structure, while the very low precipitation efficiency of the Tessendorf et al. (2007) storm may have been responsible for the lack of the near-surface charge layer. The environmental conditions responsible for the Tessendorf et al. (2007) storm, ~20 K dew point depression and greater than 20 m s^{-1} Sfc-500 hPa shear, would be rare to occur in the NAM region.

Carey and Buffalo (2007) state that multicell thunderstorms produce mainly negative CG flashes, while supercell storms are primarily responsible for positive CG flashes. This is interesting because positive CG storms will more often have broad strong updrafts and possibly lower precipitation efficiencies (if they were low precipitation supercells). Carey and Buffalo (2007) also show that positive CG storms occur in environments characterized by smaller warm cloud depths, higher cloud bases and lower near surface specific humidities with typical values of 1700 m, 2100 m AGL, and 11 g kg^{-1} respectively. In the northern NAM region for elevations between approximately 500-1000 m, low-level specific humidity values are around $12\text{-}15 \text{ g kg}^{-1}$ in the TUTT simulation (not shown), warm cloud depths are near 3000-4000 m (Rowe et al. 2008) and cloud bases are near ~1000-1500 m AGL in the simulations. This would suggest positive CG storms are rare in the NAM region and possibly storms that would have lowered CG flash counts as well. Orville et al. (2011), in their Figure 3j, show that positive flash rates over the northern SMO are very similar to those throughout regions of the US outside of the positive CG areas examined by Carey and Buffalo (2007) and the storm locations of MacGorman et al. (1989) and Tessendorf et al. (2007).

Finally there is some observational support for the simulated microphysical differences between the two simulations. Lang et al. (2010) examine SPOL polarimetric data for the NAME period and produce statistics for precipitation ice and liquid water mass among other things. They segment their data into terrain bands, and by regime. Lang et al. (2007) had previously defined a disturbed regime in which convection more readily organizes and propagates off and along the SMO. They relate disturbed days to easterly wave passage, with no mention of TUTT occurrence. Most importantly though, disturbed days are found to have increased shear at coastal sounding sites, in agreement with Finch and Johnson (2010) and this work. For disturbed days, Lang et al. (2010) find that for terrain less than 1500 m, extending onto the coastal plain and into the GoC, there is an increase in the precipitation ice mass. They specifically note the largest increases in precipitation ice mass in the mixed phase layer. There is also a slight increase in liquid water mass extending above the 0°C isotherm. These findings all agree with the simulated differences discussed above. While these results are for the southern SMO, they may directly applicable to the northern SMO, only ~500 km from SPOL.

b. Impacts on surge evolution

Comparisons between the TUTT and No_TUTT simulations have shown that there is more organized convection, precipitation and graupel along the northern SMO in the TUTT simulation. It follows that there may be more established cold pools in the TUTT simulation (Rotunno et al. 1988, Weisman and Rotunno 2004; Lang et al. 2007). Figure 4.45 displays potential temperature differences between the TUTT and No_TUTT simulations. At 18 UTC (Fig. 4.45a), convection is just becoming established along the central and southern SMO, while it is just initiating along the northern SMO (not shown).

The corresponding potential temperature difference field shows large differences along the southern and central SMO, corresponding to slightly different initiation points in the two simulations, rather than systematic differences in the cold pool generation. By 22

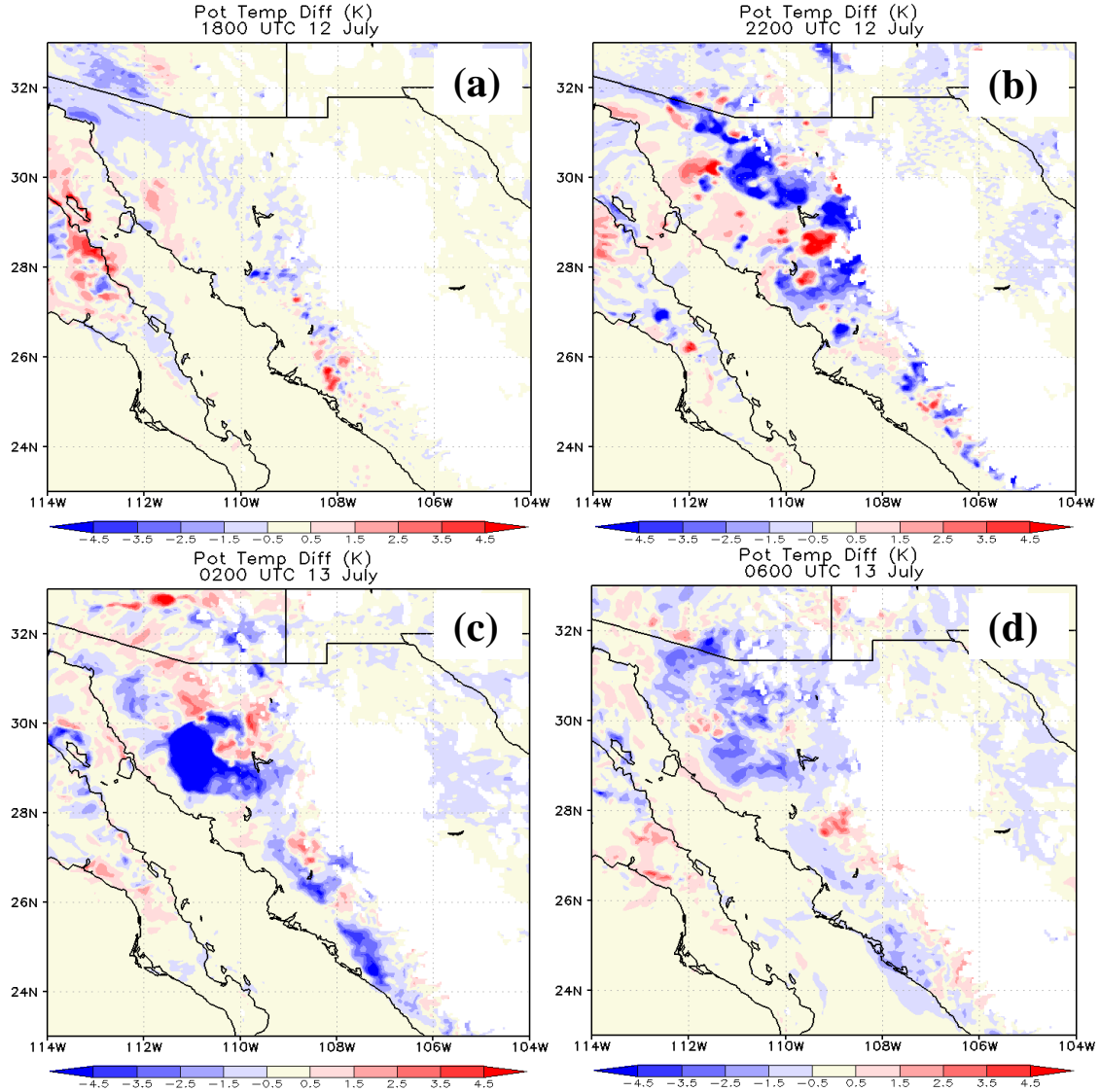


Figure 4.45. Potential temperature differences ($\text{TUTT} - \text{No_TUTT}$) (K) on the first model level (~40 m AGL) for 18 UTC (a) and 22 UTC (b) 12 July, and 02 UTC (c) and 06 UTC (d) 13 July. Areas shaded in white are above 1500 m elevation.

UTC (Fig. 4.45b), the TUTT simulation is beginning to produce more extensive cold pools (blue shading) along most of the SMO, especially north of $\sim 26^{\circ}\text{N}$. At this point there has been consistently more graupel production (Figs. 4.42, 4.43) and melting ice

mass in the TUTT simulation (not shown). The areas with the most extensive cold pools also coincide with the areas of enhanced shear (Fig. 4.35). Nearly the entire coastal plain is cooler in the TUTT simulation at 02 UTC (Fig. 4.45c), which is very near surge initiation. Again, this is likely due to the TUTT simulation having produced more graupel/melting ice mass and having had more organized convection than the No_TUTT simulation. Finally, just after surge initiation at 06 UTC (Fig. 4.45d), the TUTT simulation is still generally cooler than the No_TUTT run along a majority of the SMO. Over the GoC, the differences are near zero due to constant and equal SSTs in both simulations resulting in surface fluxes damping potential temperature anomalies.

The control simulation shows that convective outflows along the GoC are an integral part of the gulf surge which agrees with Stensrud et al. (1997). Following that, the No_subclld simulation confirms that weaker convective outflows coincide with a weaker surge, which also agrees with Stensrud et al. (1997). Figure 4.45 then implies the TUTT simulation has a stronger surge event than the No_TUTT simulation. This is confirmed in Figure 4.46, which displays the precipitable water (PW) difference (%) from 00 UTC 13 July to 00 UTC 14 July at a point (33°N , 113.5°W) near the northern extent of the gulf surge event. Over the course of the surge event the TUTT simulation has more net moisture flux into southern Arizona as evidenced by the more drastic increase in PW in the TUTT simulation. The TUTT simulation initially has ~5% less PW than the NO_TUTT simulation, while at the end of the simulation (00 UTC 14 July) it has ~15% more PW. The surge event does occur in both simulations; however the increase in PW in the No_TUTT simulation is less drastic and absolute PW begins to decrease after 21 UTC (not shown).

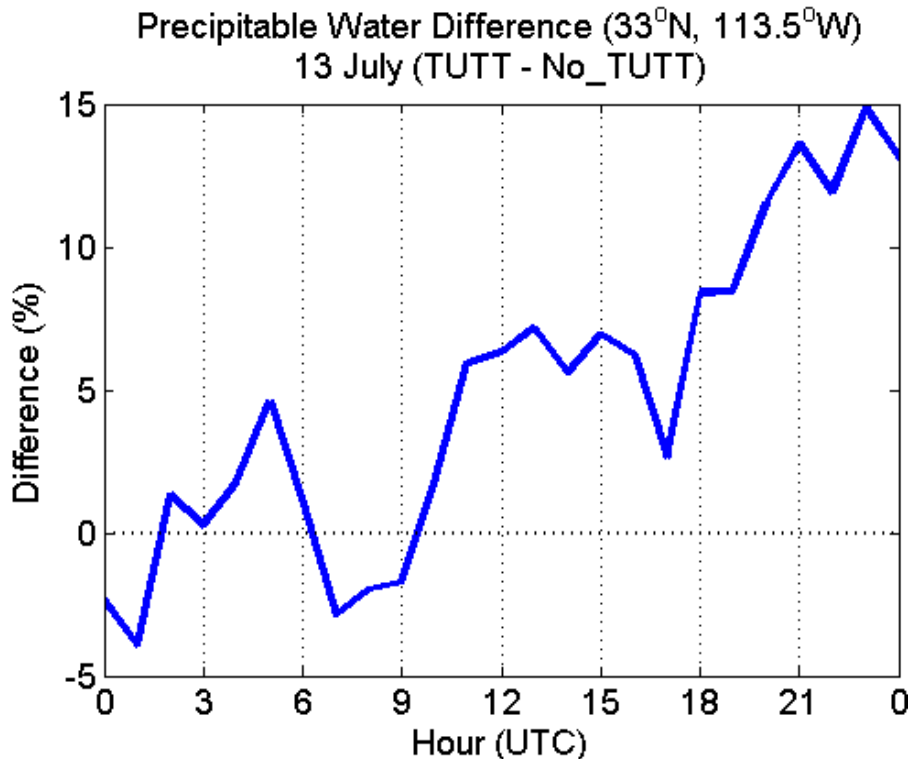


Figure 4.46. Precipitable water differences (%) between the TUTT and NO_TUTT simulations for the grid point nearest 33°N , 113.5°W (located near the northern extent of the surge event) from 00 UTC 13 to 00 UTC 14 July.

c. Summary

TUTTs in the NAM region are unique because they can enhance precipitation to the west of the TUTT center (Douglas and Englehart 2007; Bieda et al. 2009; Finch and Johnson 2010), which is unlike other TUTTs examined throughout the world (Sadler et al. 1967; Erickson 1971; Kelly and Mock 1982). The divergence mechanism proposed by Pytlak et al. (2005) states that enhanced upper-level difffluence in the northwest quadrant of a TUTT will correspond with upper-level divergence, rising motion and create an environment more favorable for convection west of the TUTT center. The TUTT and No_TUTT simulations show that difffluence is enhanced in the northwest quadrant;

however there is a lack of corresponding divergence and upward vertical velocity enhancement.

Finch and Johnson (2010) found there is a correlation between enhanced shear and mean flow, specifically in the 700-400 hPa layer and increased convective coverage for the TUTT studied herein. This study found that 700-400 hPa, Sfc-500 hPa shear and 700-400 hPa mean flow are all enhanced in the TUTT simulation in the northwest quadrant. This is primarily through changes in the mid- to upper-level flow, although there are subtle changes in the low-level flow as well. Finch and Johnson (2010) attempted to examine CAPE changes; however the analysis is limited by the sounding network and complicated by the passage of a gulf surge event, which dramatically increased low-level moisture as the TUTT was most directly influencing the sounding sites. They did note that some mid-level cooling was seen at the coastal sites associated with the TUTT, which would increase CAPE slightly. This work found that the TUTT may in fact increase CAPE, most significantly ($\sim 100\text{-}200 \text{ J kg}^{-1}$) near in the SMO foothills due to mid-upper level cooling and slight moisture increases.

Consequently, it appears that it is the combined effects of increased shear over the northern SMO and a small absolute, yet somewhat substantial percentage ($\sim 10\%$), increase in CAPE very near the SMO in the TUTT simulation that leads to the enhanced precipitation over the No_TUTT case. Finch and Johnson (2010) find a correlation between increased mid-level shear and enhanced convection along the SMO for the TUTT simulated herein. However, their observational CAPE analysis was limited to coastal sites as there were no sounding sites in the SMO foothills during NAME. Also, the influence of the gulf surge event created large changes in CAPE during the same time

period the TUTT was influencing the sounding sites. They did note some mid-level cooling near the coast, which would lead to slight increases in CAPE. In the TUTT simulation, there are slight increases in CAPE caused by very slight mid-level cooling and subtle moisture differences along the northern SMO. Examination of simulated reflectivity loops finds that convection propagates farther toward the coast of the GoC in the TUTT simulation. Precipitation increases overall and over four times as much for terrain below 500 m in the TUTT simulation, in general agreement with Douglas and Englehart (2007), Bieda et al. (2009), and Finch and Johnson (2010).

Bieda et al. (2009) also found that there is statistically significant increase in CG lightning over much of the northern SMO during TUTT passages. While the general increase in convection would be expected to lead to increased CG lightning, subtle changes in shear and CAPE also lead to microphysical differences in the two simulations. Specifically, there is more graupel in the charging layer (Latham et al. 2004) along with more supercooled liquid water, cloud ice and precipitation ice mass in the TUTT simulation. This could lead to further enhancement of CG lightning production for the TUTT simulation through a more dynamic non-inductive charging mechanism (Nesbitt et al. 2000; Petersen and Rutledge 2001; Deierling et al. 2005; Petersen et al. 2005; Wiens et al. 2005; Latham et al. 2007; Deierling et al. 2008). It is possible to have increases in graupel and ice mass without increases in CG lightning (MacGorman et al. 1989; Tessendorf et al. 2007), however the environmental conditions and convection along the northern SMO do not seem to fit with those studies, which are directed more toward supercell-like conditions. The simulated microphysical differences are supported

observationally by Lang et al. (2010). Therefore, there may be a microphysical connection to the increased lightning counts during TUTT passages as well.

The same combined mechanism and microphysical differences may result in TUTTs modifying surge strength on 13 July. This study and prior work (Stensrud et al. 1997) has shown the importance of convection in surge initiation and evolution. It follows that features which modulate convection could modulate surge intensity. The TUTT simulation produces more convective outflow through the combination of two possible mechanisms. Increased graupel production leads to more melting ice mass leading to increased cold pools and enhanced mid-level shear supports more organized convection that propagates farther off the SMO and produces more precipitation.

4. Idealized Simulations

While the control simulation is very valuable in clarifying what the dynamics of a gulf surge are and how they evolve, elucidating which features of the surge are related to what attribute present in the GoC is still difficult. For that reason, five two dimensional dry simulations using the Bryan Cloud Model (CM1) (Bryan 2002; Bryan and Fritch 2002) were performed to further examine aspects of the observed surge features. The five simulations (see Chapter 2, section 2d) again are: the base simulation which includes all four attributes highlighted for exclusion, the No_LLJ simulation which excludes the GoC LLJ, the No_fric run excluding surface friction, the No_slope run excluding the climatological along-the-GoC slope of the isentropes and the No_pool run which excludes the secondary cold pool representing convective outflow in the north central GoC ahead of the deep surge feature. The initial potential temperature (Fig. 4.47a) and

perturbation potential temperature (Fig. 4.47b) show the location and sizes of

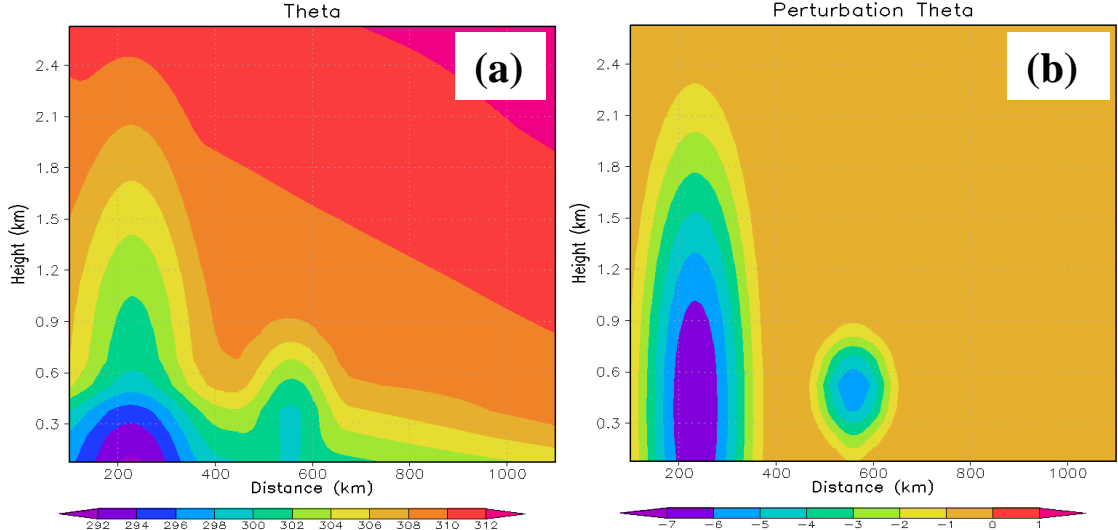


Figure 4.47. Initial potential temperature with both cold pools (a) while (b) displays the perturbation potential temperature. The primary cold pool is located near 220 km while the secondary cold pool is initialized near 550 km.

the two cold pools. The cold pool centered near 550 km is the secondary cold pool removed in the No_pool simulation.

Figure 4.48 displays a time series potential temperature anomaly and wind magnitude sampled at half hourly frequency for the base simulation and the same fields and frequency from PP. Again the goal of these highly idealized simulations is to recreate general features of the gulf surge, not precise details. From Fig. 4.48, one can see the base run recreates a deepening wind surge feature (7.5 m s^{-1} contour in Fig. 4.48a, 10 m s^{-1} contour in Fig. 4.48b) between 07-09 UTC. This feature is associated with the convective outflow leading the main surge core, the leading cold pool in the ideal simulation and the leading bore in reality. The general shape of the main surge core (10 m s^{-1} contour Fig. 4.48a, 17.5 m s^{-1} contour in Fig. 4.48b) is also recreated in the base simulation. The leading cold pool also creates a shelf of cooling just above the surface

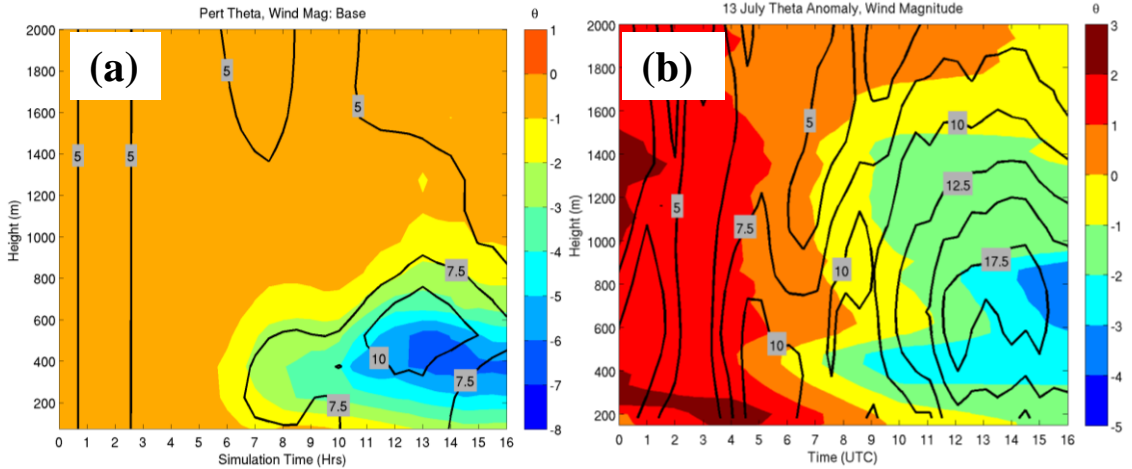


Figure 4.48. Simulated potential temperature anomalies (shading) and wind magnitude (contours) for the base simulation 900 km from the southern model boundary in (a), with the observed half-hourly interpolated sounding derived potential temperature anomalies (shading) and half-hourly 915 MHz consensus winds (contours) in (b) for 00 to 16 UTC 13 July. Note the different scales for the potential temperature anomalies.

through ~600 m with sloped perturbation isentropes intersecting the surface as the main surge arrives. The depth of the surge is less than observed in both the wind and potential temperature field, which may relate to the simple surface friction parameterization, lack of boundary layer scheme or surface fluxes precluding deeper mixing. Note, the observed convective outflow passages before 07 UTC were not attempted to be recreated in the idealized simulations.

Figure 4.49 displays potential temperature anomalies and wind magnitude contours for the other four simulations. The No_LLJ simulation (Fig. 4.49a) has nearly the same features as the base simulation. The only effect of the addition of the LLJ appears to be an enhancement of the core of the surge event, which coincides with the peak of the GoC LLJ. The vertical extent of the strongest wind core is slightly reduced. This shows the LLJ has some influence on the depth and strength of a surge when they coincide, which is expected. Without friction (Fig 4.49b) the depth of the simulated surge is reduced and the strongest winds extend to the surface. Also, the arrival of the

most negative surface potential temperature perturbations is sooner than the base simulation. These are expected results for a simulation without friction since friction is an oppositional force and show the importance of friction in modulating the surge height.

When the second cold pool representing additional convective outflow in the north central GoC and the lead internal bore in the control simulation is removed (No_pool), the surge character changes more dramatically (Fig. 4.49c). The initial deepening wind and cooling feature is lost. Some lead cooling does advance ahead of the main surge but is much weaker and arrives later than the base simulation. The core surge feature arrives at nearly the same time, however it has a gradually deepening (10 m s^{-1} contour, Fig. 4.49c) maximum wind core that is not observed. The potential temperature anomalies are also slightly less negative with slightly less surface cooling. This indicates that the various convective outflows are important to the surge structure and intensification as shown in the control simulation. The leading bore appears to increase the inversion height and deepen the surface mixed layer in the observations and control simulation. That seems to be confirmed here, because without the leading impulse the surge structure changes and the initial portion of the maximum wind core is at a lower elevation. The leading shelf of cooling is also less pronounced in the No_pool simulation as compared to the base simulation, which is in less agreement with observations.

The removal of the sloped isentropes and introduction of a well-defined marine mixed layer and strong inversion leads to drastically different surge behavior. The two cold pools generate features that propagate along the inversion layer faster than in the other simulations. This is due to an increase in the difference in the lower- and upper-layer potential temperatures (see Fig. 2.6) and a resultant increase in reduced gravity and

phase speed for the No_slope simulation. The gravity waves propagating along the inversion layer become separated from the low-level cooling, which behaves like a gravity current. All definition of the surge core is lost with very unrealistic cooling and wind structure. While this idealized mixed layer and inversion structure may be unrealistic with the strength of the inversion, the lack of a well-defined near surface mixed layer is observed at KB and PP prior to surge passage. These sites have a potential temperature profile more similar to that of the base simulation.

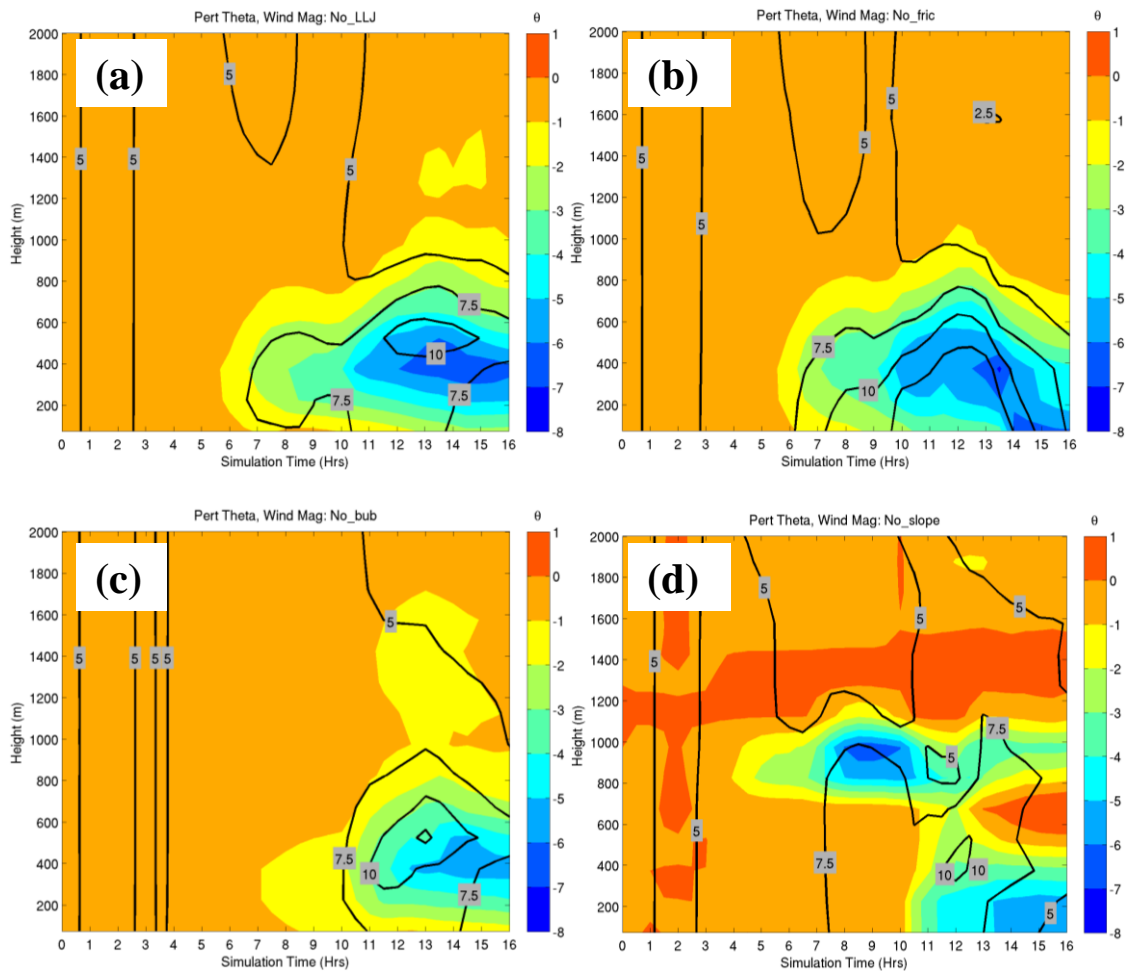


Figure 4.49. Same as Figure 4.48a, except for the No_LLJ (a), No_fric (b), No_pool (c), and No_slope (d) simulations.

Overall, this set of simulations shows the ability of a two-dimensional dry model to capture some of the features associated with the 12-13 July 2004 surge event. The

base simulation recreates the leading bore followed quickly by the main Kelvin wave through two-dimensional gravity waves. This gives further confidence to the idea that the initial strong surge feature seen in the northern GoC on 13 July is shaped primarily through convective outflow. Without the more northern convective outflow included, the surge structure changes noticeably. The GoC LLJ appears to intensify and deepen the maximum wind core beyond that of the bore and Kelvin wave alone. Finally, use of an idealized sounding that has a well-defined surface mixed layer and strong inversion leads to a wave evolution that is very unlike that observed at PP. This reaffirms the importance of simulating the correct potential temperature distribution when modeling internal gravity wave features or surges along the Gulf of California.

CHAPTER V

CONCLUSIONS

1. Control simulation

A convection-permitting simulation over the entire core of the North American Monsoon (NAM) using the WRF-ARW model for the 12-14 July 2004 Gulf of California (GoC) southerly moisture surge is able to reproduce the observed surge event. The modeled surge event is contained within a North American Monsoon Experiment (NAME) field campaign intensive observing period (IOP). IOPs have enhanced observations over the already extensive NAME observations, which allows for unprecedented comparisons between the surge simulation and observations. The simulation is compared to integrated sounding site (ISS) surface, rawinsonde, and 915 MHz wind profiler observations, NAME radar network reflectivity maps, and cross sections from the NOAA WP-3D research aircraft.

The simulation captures the general timing and features of convection in the southern GoC on 12 July along with a corresponding cold pool and a larger disturbance in the flow field, denoted as structure 2 (S2) in Mejia et al. (2010) and this study, that appears to be forced by the convectively generated cold pool. The idealized two-layer shallow water framework discussed in Ralph et al. (2000) and the work of Reason and Steyn (1992) is applied to examine the dynamics of S2. From this analysis, it appears that S2 is a Kelvin wave with some non-linearity. S2 propagates up the southern GoC on 12 July with an intrinsic phase speed of $\sim 17 \text{ m s}^{-1}$ and a total speed of $\sim 21 \text{ m s}^{-1}$ and

becomes ill-defined around 22 UTC in the central GoC near Kino Bay (KB) (Fig 5.1). While S2 is not the actual initial surge feature seen in the northern GoC, it is important because it signifies the leading edge of southerly flow, slight cooling and moistening below 800 hPa in the southern and central GoC. The southerly flow behind S2 continues through the surge on 13 July. Thus, S2 appears to precondition the southern and central GoC to a cooler and moister state leading into the surge event on 13 July.

On 13 July the simulation correctly reproduces convection along the Sierra Madre Occidental (SMO) and loosely organized clusters that propagate off the SMO towards the GoC through around 09 UTC. The simulation appears to produce too little stratiform precipitation and evolves the convection too fast as compared to the radar network observations. The timing of the surge feature at KB and Puerto Penasco (PP) is slightly advanced in the simulation, by 1-3 hours. Surface traces show that the simulation generally reproduces the correct surge surface features. The simulated surge is too shallow and has weaker wind speeds than observed in the 915 MHz wind profiler and rawinsonde data. This may be related to the boundary layer scheme in the model in combination with the lack of stratiform precipitation and corresponding weaker convective outflows impacting surge strength. However, the simulated surge structure in a cross-gulf cross section agrees very well with that observed by the NOAA WP-3D. The wind field in this case appears to be only slightly shallower than observed. The simulated surge has a total system speed of $\sim 22 \text{ m s}^{-1}$, which is in very good agreement with the observed surge system speed diagnosed by Rogers and Johnson (2007; RJ2007). The simulated surge (in the total system speed sense) also appears to slow down as it enters the northern GoC, also in agreement with RJ2007.

Modeled surge initiation occurs between 01-04 UTC in the southern GoC through a confluence of inflow from the mouth of the GoC, gap flow from the Pacific Ocean and convective outflow along the SMO. The surge is then substantially modified and enhanced by the continuation of cool air input from several convective outflows along the southern and central GoC. The same dynamical analysis of the surge on 13 July shows that the surge is likely a solitary Kelvin wave at KB with an intrinsic phase speed of \sim 13 $m s^{-1}$. By the time the surge reaches PP, a leading bore-like feature is found in the simulation and observations (RJ2007), and has an intrinsic phase speed of \sim 13 $m s^{-1}$. This bore deepens the inversion layer at PP and increases the background flow ahead of the surge core and significant surface cooling. Following the leading bore, the brunt of the simulated surge appears to be a solitary Kelvin wave with an intrinsic phase speed of \sim 14 $m s^{-1}$. This feature is associated with surface cooling and another slight pressure rise at PP.

a. Surge schematic

Figures 5.1 and 5.2 show the general evolution of the simulated surge on 12 and 13 July, respectively. Initially, convection associated with the tropical easterly wave precursor to tropical storm Blas creates a disturbance in the southern GoC on 12 July around 06-09 UTC. In the simulation, this Kelvin wave propagates up the GoC and becomes diffuse just south of KB around 22 UTC 12 July (Fig 5.1). Behind the initial Kelvin wave is southerly flow and slight cooling and moistening below \sim 800 hPa in the observations and \sim 750 hPa in the simulation. Convection then forms along the length of the SMO late on 12 July into 13 July. Inflow from the mouth of the GoC and Pacific Ocean along with convective outflow impinging on the southern GoC appears to initiate

the surge feature by early on 13 July (Fig 5.2). Continued convective outflow entering the GoC intensifies the surge as it propagates up the GoC. As the core of the surge reaches the northern GoC, it appears to be a non-linear, or solitary, Kelvin wave. Substantial low-level cooling and moistening are associated with the simulated and observed surge feature.

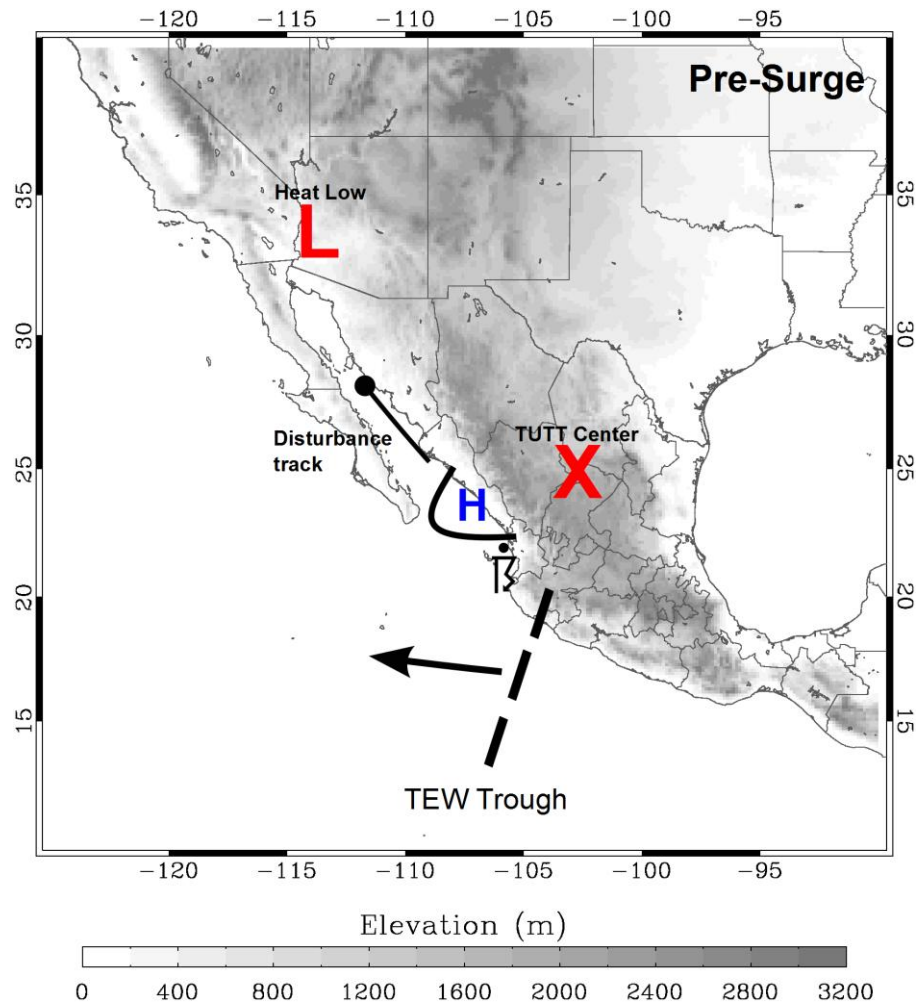


Figure 5.1. General schematic of the evolution of important features on 12 July. The red X marks the general position of the TUTT around 12 UTC, the blue H and curved black line denote the position of the coastally trapped disturbance (S2) and corresponding higher MSLP around 12 UTC with the straight line ending near 28°N indicating motion and dissipation location, the heavy thunderstorm symbol denotes the location of the organized convective cluster around 09 UTC, while the dashed line and arrow give the location and movement of the TEW trough.

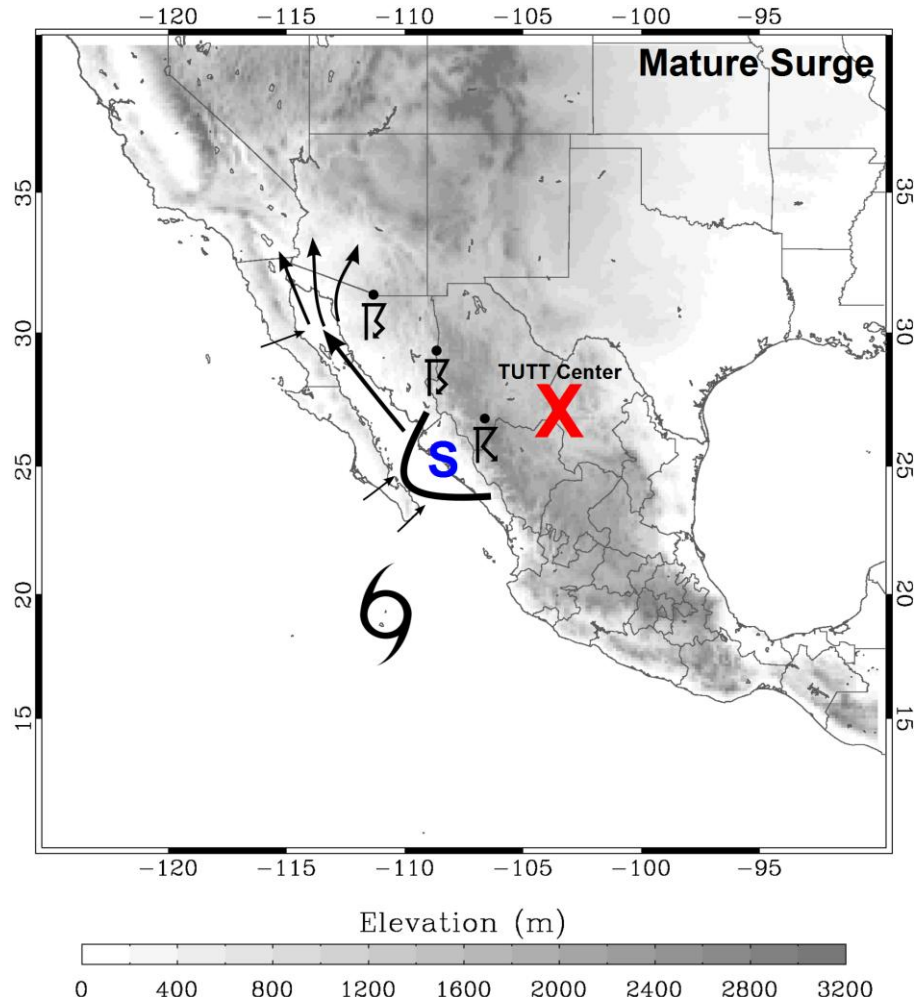


Figure 5.2. General schematic of the evolution of important features on 13 July. The red X marks the general position of the TUTT around 06 UTC. The blue S, black curve, thick black arrow denote the general initiation location of the gulf surge as well as its propagation, while the three thinner arrows denote the surge spreading into the northern GoC and desert US after 12 UTC. Smallest arrows indicate general areas of gap/inflow from Pacific Ocean before 12 UTC. The tropical cyclone symbol denotes the location of TS Blas around 12 UTC. The heavy thunderstorm symbols denote areas of more organized and persistent convection between 00-10 UTC while the moderate thunderstorm symbol (near 25°N) indicates less organized and persistent convection.

That the surge signal seen at PP around 12 UTC 13 July is preceded by a wave on 12 July (Fig. 5.1) associated with a tropical easterly wave could possibly explain how TEW/TCs are tied to gulf surge events. Stensrud et al. (1997), Fuller and Stensrud

(2000) and Adams and Stensrud (2007) show that gulf surges are typically preceded by tropical easterly wave passage. Adams and Stensrud (2007) also find that removal of tropical easterly waves in simulations results in weaker surges that occur at different times and are often associated with waves generated internally by the model. In this case, removal of the Kelvin wave on 12 July may change the evolution and character of the surge event on 13 July. The Kelvin wave is followed by cooling, moistening and southerly flow in the southern and central GoC that extends throughout 13 July. It could be that without this initial cooling and inflow into the southern GoC, the surge and convective initiation and evolution along the southern SMO would be different. This should be the subject of further study.

2. Modified microphysics and topography simulations

A sensitivity test removing evaporation from rain below cloud base (No_SUBCLD) shows that the moisture flux associated with the surge is lessened in the No_SUBCLD run as compared to the control simulation. The mean wind speed in the northern GoC during the peak hours of the surge, 10-15 UTC 13 July is 7.2 m s^{-1} and 7.7 m s^{-1} in the No_SUBCLD and control simulations, respectively. These findings agree with Stensrud et al. (1997) where a run without any diabatic processes developed a much weaker surge compared to their control run. This simulation produces a weaker surge with less drastic model modifications and also at a convective permitting resolution.

A second sensitivity simulation examining the influence of gap flow (No_gaps) on surge evolution and strength is also performed. The simulation increases the height of the peninsular ranges such that flow is essentially completely blocked from entering the GoC from the Pacific Ocean. This does result in greater moisture fluxes in the simulated

surge due to less dry air entering the GoC. This dry air encroaches, in a modified form, all the way to the eastern GoC coastal plain and the SMO, altering convective evolution. The No_gaps simulation has slightly more moisture near the SMO and slightly more extensive convection that produces larger cold pools and the resulting increase in surge intensity. The No_gaps simulation has a mean wind speed in the northern GoC between 10-15 UTC 13 July of 8.3 m s^{-1} , compared to 7.7 m s^{-1} in the control simulation. Most importantly, this simulation shows that the general features, evolution and dynamics of the surge are very similar regardless of the topography of the Baja Peninsula.

3. Impacts of TUTT removal

Tropical upper-tropospheric troughs (TUTTs) in the NAM region are unique in that they have enhanced precipitation on the western side (Douglas and Englehart 2007; Bieda et al 2009; Finch and Johnson 2010), while TUTTs throughout the rest of the world typically have enhanced precipitation on the eastern flank (Erickson 1971; Kelly and Mock 1982; Chen and Chou 1994; Whitfield and Lyons 1992). Finch and Johnson (2010) found that enhanced shear in the 700-400 hPa layer had the highest correlation with increased convection for the TUTT studied here and found quasigeostrophic diagnosed subsidence in the western side, in disagreement with the mechanism proposed by Pytlak et al. (2005). The use of a modified vorticity removal algorithm allows for the removal of the vorticity anomaly associated with the TUTT in the initial conditions for a simulation. Two simulations, one with the TUTT (TUTT) and one without (No_TUTT) are then started from the same initial conditions, permitting examination of TUTT influences on convection and the gulf surge.

Results show that the TUTT simulation has enhanced 300 hPa diffusence in advance of the circulation center, in agreement with Pytlak et al. (2005). However, there is no appreciable enhancement of upper-level divergence or rising motion along the SMO in the TUTT simulation as compared to the No_TUTT simulation. The TUTT simulation does show enhanced 700-400 hPa and Sfc-500 hPa shear along the central and northern SMO on late 12 July, in agreement with Finch and Johnson (2010). The TUTT simulation also shows slight increases (on the order of 100 J kg^{-1}) in CAPE, primarily along the SMO foothills. Some slight mid-level cooling was found in the sounding analysis of Finch and Johnson (2010), but the large CAPE changes due to the surge event on 13 July and lack of sounding sites near the SMO foothills prevented conclusive evidence in their study that the TUTT affected CAPE as well as shear. The TUTT simulation shows that a combination of slightly increased shear and CAPE caused by low-level moistening and mid-level cooling along the northern SMO results in more organized convection that produces more extensive cold pools. This further clarifies how TUTTs enhance precipitation along the SMO.

The TUTT simulation produces 23% more precipitation than the No_TUTT simulation along the SMO north of 28°N between 18 UTC 12 July and 12 UTC 13 July, when the TUTT is influencing the northern SMO. More robust updrafts for the first ~5 hours of convective evolution along the northern SMO as are found in the TUTT simulation as well. Breaking down precipitation into three terrain categories, low: $< 500 \text{ m}$, middle: between 500 and 1000 m, and high: $> 1000 \text{ m}$, the TUTT simulation produces 431% more, 14% less, and 18% more for the categories respectively. This implies that the No_TUTT simulation produces slightly less initial convection over the high terrain,

that convection does not propagate as fast toward the lower terrain, and precipitates heaviest over the slopes of the SMO before decaying quickly over the low terrain. Assessment of simulated radar reflectivity loops confirms this finding.

There are also significant microphysical differences between the two simulations. The TUTT simulation produces more graupel, cloud ice and supercooled liquid water between 16 UTC 12 July and 01 UTC 13 July. Specifically the TUTT simulation produces the most significant graupel increases in the layer between 0 and -20°C, known as the charging zone (Latham et al. 2004). The TUTT simulation also produces more total graupel and supercooled liquid water mass for the entire period between 16 UTC 12 July – 10 UTC 13 July. Prior work has shown a strong correlation between CG and total lightning counts to graupel volume and/or ice mass flux in the charging zone (Nesbitt et al. 2000; Petersen and Rutledge 2001; Deierling et al. 2005; Petersen et al. 2005; Wiens et al. 2005; Latham et al. 2007; Deierling et al. 2008). The increased graupel, cloud ice and supercooled liquid water as well as more robust updrafts in the TUTT simulation suggests a more active charging zone and stronger non-inductive charging process and an increase in CG lightning (Wiens et al. 2005; Latham et al. 2007; Deierling et al. 2008).

This may further explain the results of Bieda et al (2009). They found that days with TUTTs present in the NAM region produce a statistically significant increase in cloud-to-ground (CG) lightning along the SMO and coastal plain north of 28°N. While the increased convective organization and precipitation totals would lead one to believe CG lightning would increase, microphysical changes could play an important role as well, which is evident herein.

The simulated microphysical changes have observational support from Lang et al. (2010), who use SPOL polarimetric radar data to derive hydrometeor statistics for the NAME period for disturbed and non-disturbed days. Their definition of disturbed days includes days when convection is more organized and includes TUTT days as well as TEW days. They find statistically significant increases in ice mass on disturbed days that are the largest in the mixed phase region. Slight increases in liquid water above the freezing level are also found on disturbed days. These results agree very well with the simulated differences.

These processes likely also result in the weaker simulated surge in the No_TUTT simulation on 13 July. Convection is intimately linked to surge initiation and evolution as shown in this study and others (e.g. Stensrud et al. 1997). Since TUTTs modulate convection it is logical they also modulate surge strength. The TUTT simulation produces more convective outflow through the combination of increased shear and graupel production. The enhanced graupel amounts lead to more melting ice mass, leading to increased cold air production and larger cold pools. Enhanced mid-level shear supports more organized convection that propagates further off the SMO and produces more precipitation and helps to partially balance the vorticity created by more intense cold pools (Rotunno et al. 1988; Weisman and Rotunno 2004). However, this is one example and no statistical study has been performed linking TUTTs to surge strength over an extended period of time. An analysis similar to that of Bieda et al. (2009) investigating surge duration and/or intensity and TUTTs, in conjunction with these results, could robustly link TUTTs and surge characteristics in the northern GoC and the desert US.

4. Idealized surge simulations

Idealized two-dimensional dry simulations using the Bryan Cloud Model (CM1) help distinguish which simulated and observed processes relate to certain surge features. Four processes or features (and corresponding simulations removing such features), the GoC low-level jet (LLJ) (No_LLJ), surface friction (No_fric), the sloped state of the isentropes along the GoC (No_slope), and the convective outflow related to the leading bore at PP (No_bub) are all examined in the idealized framework. The simulation including all these processes (base) is able to recreate the initial, bore-related elevated cooling at the northern end of the GoC, followed by the arrival of the highest wind speeds and surface cooling. The shape of the maximum wind core is also in the best agreement with observations in the base simulation. Removal of the GoC LLJ results in a smaller area of maximum winds in the surge core. The No_fric simulation has slightly shallower cooling and an unrealistic wind field, with the maximum winds extending all the way to the surface. Without the leading bore feature, the leading slightly elevated cooling loses definition and the shape of the surge wind core less resembles observations. Finally, the No_slope simulation results in a completely unrealistic idealized surge. The two-dimensional simulations show that convective outflows can generate the observed features in the presence of many other modifying processes like the GoC LLJ.

Further two-dimensional simulations could examine variations of the basic cases shown here. Changes to the inversion height and strength may yield more “surge like” evolution. Different initial sizes and intensities to the cold bubbles will likely change the duration and structure of the idealized surge as well. Inclusion of more sophisticated surface friction and fluxes would be very beneficial as well as some type of boundary

layer parameterization. Three-dimensional simulations should also be explored. These simulations could include real topography and a non-homogeneous temperature structure similar to the two-dimensional simulations. These simulations may be more difficult to initialize and perform due to the added dimension. The GoC LLJ, topography, temperature structure and Pacific Ocean inflow become much more complex to address in a three-dimensional framework. However, further beneficial information would result from some successful simulations in a three-dimensional framework.

REFERENCES

- Adams, D. K. and A. C. Comrie, 1997: The North American monsoon. *Bull. Amer. Meteor. Soc.*, **78**, 2197-2213.
- Adams, J. L., and D. J. Stensrud, 2007: Impact of tropical easterly waves on the North American monsoon. *J. Climate*, **20**, 1219-1238.
- Anagnostou, E. N., C. A. Morales, and T. Dinku, 2001: The use of TRMM precipitation radar observations in determining ground radar calibration biases. *J. Atmos. Oceanic Technol.*, **18**, 616-628.
- Anderson, B. T., J. O. Roads, and S.-C. Chen, 2000a: Large-scale forcing of summertime monsoon surges over the Gulf of California and the southwestern United States. *J. Geophys. Res.*, **105**, 24 455- 24 467.
- Anderson, B. T., J. O. Roads, and S.-C. Chen, 2000b: Regional simulation of the low-level monsoon winds over the Gulf of California and southwestern United States. *J. Geophys. Res.*, **105**, 17 955-17 969.
- Anderson, B. T., J. O. Roads, and S. C. Chen, 2001: Model dynamics of summertime low-level jets over northwestern Mexico. *J. Geophys. Res.*, **106**, D4, 3401-3413.
- Angevine, W. M., A. B. White, and S. K. Avery, 1994: Boundary-layer depth and entrainment zone characterization with a boundary-layer profiler. *Boundary-Layer Meteor.*, **68**, 375-385.
- Badan-Dangon, A., C. E. Dorman, M. A. Merrifield, and C. D. Winant, 1991: The lower atmosphere over the Gulf of California. *J. Geophys. Res.*, **96**, 877-896.
- Beals, E. A., 1922: The semipermanent Arizona low. *Mon. Wea. Rev.*, **50**, 341-345.
- Berbery, E. H., 2001: Mesoscale moisture analysis of the North American Monsoon. *J. Climate*, **14**, 121-137.
- Benjamin, T. B., 1968: Gravity currents and related phenomena. *J. Fluid. Mech.*, **31**, 209-248.
- Bieda, S. W. III, C. L. Castro, S. L. Mullen, A. C. Comrie, and E. Pytlak, 2009: The relationship of transient upper-level troughs to variability of the North American monsoon system. *J. Climate*, **22**, 4213-4227.

- Blyth, A. M., H. J. Christian, K. Driscoll, A. M. Gadian, and J. Latham, 2001: Determination of ice precipitation rates and thunderstorm anvil ice contents from satellite observations of lightning. *Atmos. Res.*, **59-60**, 217-229.
- Bordoni, S. and B. Stevens, 2006: Principal component analysis of the summertime winds over the Gulf of California. A gulf surge index. *Mon. Wea. Rev.*, **134**, 3395-3414.
- Bordoni, S., P. E. Ciesielski, R. H. Johnson, B. D. McNoldy, and B. Stevens, 2004: The low-level circulation of the North American monsoon as revealed by QuikSCAT. *Geophys. Res. Lett.*, **31**, L10109, doi:10.1029/2004GL020009.
- Brenner, I. S., 1974: A surge of maritime tropical air-Gulf of California to the southwestern United States. *Mon. Wea. Rev.*, **102**, 375-389.
- Bryan, G. H., 2002: An Investigation of the Convective Region of Numerically Simulated Squall Lines. Ph.D. dissertation, The Pennsylvania State University, 181 pp.
- Bryan, G. H., and J. M. Fritsch, 2002: A Benchmark Simulation for Moist Nonhydrostatic Numerical Models., *Mon. Wea. Rev.*, **130**, 2917-2928.
- Bryan, G. H., J. C. Wyngaard, and J. M. Fritsch, 2003: Resolution requirements for the simulation of deep moist convection. *Mon. Wea. Rev.*, **131**, 2394-2416.
- Bryan, G. H., J. C. Knievel, and M. D. Parker, 2006: A multimodel assessment of RKW theory's relevance to squall-line characteristics. *Mon. Wea. Rev.*, **134**, 2772-2792.
- Bryan, G. H., and H. Morrison, 2011: Sensitivity of a simulated squall line to horizontal resolution and parameterization of microphysics. *Mon. Wea. Rev.*, in press.
- Bryson, R. A., and W. P. Lowry, 1955: Synoptic climatology of the Arizona summer precipitation singularity. *Bull. Amer. Meteor. Soc.*, **36**, 329-339.
- Bruyere, C., M. Duda, J. Dudhia, D. Gill, H.-C. Lin, J. Michalakes, S. Rizvi, W. Wang, and X. Zhang, 2010: Weather Research and Forecasting ARW Version 3 Modeling System User's Guide, Mesoscale & Microscale Meteorology Division, National Center for Atmospheric Research, 312 pp. [Available from the National Center for Atmospheric Research, Boulder, CO 80301].
- Byers, H. R., and R. R. Braham, 1948: Thunderstorm structure and circulation. *J. Meteor.*, **5**, 71-86.
- Campbell, A., 1906: Sonora storms and Sonora clouds of California. *Mon. Wea. Rev.*, **34**, 464-465.

- Carey, L. D., and S. A. Rutledge, 1996: A multiparameter radar case study of the microphysical and kinematic evolution of a lightning producing storm. *J. Meteor. Atmos. Phys.*, **59**, 33-64.
- Carey, L. D., and K. M. Buffalo, 2007: Environmental control of cloud-to-ground lightning polarity in severe storms. *Mon. Wea. Rev.*, **135**, 1327-1353.
- Carleton, A. M., 1985: Synoptic and satellite aspects of the southwestern U.S. summer “monsoon.” *J. Climatol.*, **5**, 389-402.
- Carleton, A. M., 1986: Synoptic-dynamic character of “bursts” and “breaks” in the southwest U.S. summer precipitation singularity. *J. Climatol.*, **6**, 605-623.
- Carleton, A. M., D. A. Carpenter, and P. J. Weser, 1990: Mechanisms of interannual variability of southwest United States summer precipitation maximum. *J. Climate*, **3**, 999-1015.
- Chappell, C. F., 1986: Quasi-stationary convective events. *Mesoscale Meteorology and Forecasting*, P.S. Ray, Ed., Amer. Meteor. Soc., 289-309.
- Chen, G. T. J., and L. F. Chou, 1994: An investigation of cold vortices in the upper-troposphere over the western north pacific during the warm-season. *Mon. Wea. Rev.*, **122**, 1436-1448.
- Ciesielski, P. E. and R. H. Johnson, 2008: Diurnal cycle of surface flows during 2004 NAME and comparison to model reanalysis. *J. Climate*, **21**, 3890-3913.
- Corfidi, S. F., 2003: Cold pools and MCS propagation: Forecasting the motion of downwind-developing MCSs. *Wea. Forecasting*, **18**, 997-1017.
- Cotton, W. R., G. H. Bryan, and S. C. van den Heever, 2010: Storm and Cloud Dynamics. Academic Press, 2nd Ed., 820 pp.
- Crook, N. A., 1996: Sensitivity of moist convection forced by boundary layer processes to low-level thermodynamic fields. *Mon. Wea. Rev.*, **124**, 1767-1785.
- Cummins, K. L., M. J. Murphy, E. A. Bardo, W. L. Hiscox, R. B. Pyle, and A. E. Pifer, 1998: A combined TOA/MDF technology upgrade of the U.S. National Lightning Detection Network. *J. Geophys. Res.*, **103** (D8), 9035-9044.
- Deierling, W., W. A. Petersen, J. Latham, S. M. Ellis, and H. J. Christian Jr., 2005: On the relationship of thunderstorm ice hydrometeor characteristics and total lightning measurements. *Atmos. Res.*, **76**, 114-126.

- Deierling, W., W. A. Petersen, J. Latham, S. Ellis, H. J. Christian, 2008: The relationship between lightning activity and ice fluxes in thunderstorms. *J. Geophys. Res.*, **113**, D15210, doi:10.1029/2007JD009700.
- Douglas, A. V., and P. J. Englehart, 2007: A climatological perspective of transient synoptic features during NAME 2004. *J. Climate*, **20**, 1947-1954.
- Douglas, M. W., R. A. Maddox, K. Howard, and S. Reyes, 1993: The Mexican monsoon. *J. Climate*, **6**, 1665-1677.
- Douglas, M. W., 1995: The summertime low-level jet over the Gulf of California. *Mon. Wea. Rev.*, **123**, 2334-2347.
- Douglas, M. W., A. Valdez-Manzanilla, R. G. Cueto, 1998: Diurnal variation and horizontal extent of the low-level jet over the northern Gulf of California. *Mon. Wea. Rev.*, **126**, 2017-2025.
- Douglas, M. W., and J. C. Leal, 2003: Summertime surges over the Gulf of California: Aspects of their climatology, mean structure, and evolution from radiosonde, NCEP reanalysis, and rainfall data. *Wea. Forecasting*, **18**, 55-74.
- Douglas, M. W., J. F. Mejia, J. M. Galvez, R. Orozco, and J. Murillo, 2006: The seasonal evolution of the diurnal variation of the low-level winds around the Gulf of California. Is there a link to vegetation green-up during the wet season? Preprints, *18th Conf. on Climate Variability and Change*, Atlanta, GA, Amer. Meteor. Soc, CD-ROM, J3.4.
- Dye, J. E., J. J. Jones, A. J. Weinheimer, and W. P. Winn, 1989: Observations within two regions of charge during initial thunderstorm electrification. *Quart. J. Roy. Meteor. Soc.*, **114**, 1271-1290.
- Erickson, C. O., 1971: Diagnostic study of a tropical disturbance. *Mon. Wea. Rev.*, **99**, 67-78.
- Farfan, L. M., and J. A. Zehnder, 1994: Moving and stationary mesoscale convective systems over northwest Mexico during the Southwest Area Monsoon Project. *Wea. Forecasting*, **9**, 630-639.
- Fawcett, P. J., J. R. Stalker, and D. S. Gutzler, 2002: Multistage moisture transport into the interior of northern Mexico during the North American summer monsoon. *Geophys. Res. Lett.*, **29**, 2094, doi:10.1029/2002G1015693.
- Finch, Z. O., and R. H. Johnson, 2010: Observational analysis of an upper-level inverted trough during the 2004 North American Monsoon Experiment. *Mon. Wea. Rev.*, **138**, 3540-3555.

Fredrick, S., C. Davis, D. Gill, S. Low-Nam, 2009: Bogussing of Tropical Cyclones in WRF Version 3.1. Technical document, National Center for Atmospheric Research, 6 pp. [Available from the National Center for Atmospheric Research, Boulder, CO 80301.]

Fuller, R. D., and D. J. Stensrud, 2000: The relationship between tropical easterly waves and surges over the Gulf of California during the North American monsoon. *Mon. Wea. Rev.*, **128**, 2983-2989.

Gill, A. E., 1982: Atmosphere-Ocean Dynamics. Academic Press, 662 pp.

Gochis, D. J., A. J. Jimenez, C. J. Watts, J. Garatuza-Payan, and W. J. Shuttleworth, 2004: Analysis of 2002 and 2003 warm season precipitation from the North American Monsoon Experiment event rain gauge network. *Mon. Wea. Rev.*, **132**, 2938-2953.

Green, C. R., and W. D. Sellers, Ed, 1964: Arizona Climate. University of Arizona Press, 503 pp.

Haertel, P. T., R. H. Johnson, S. N. Tulich, 2001: Some simple simulations of thunderstorm outflows. *J. Atmos. Sci.*, **58**, 504-516.

Hales, J. E., Jr., 1972: Surges of maritime tropical air northward over the Gulf of California. *Mon. Wea. Rev.*, **100**, 298-306.

Hales, J. E., Jr., 1974: Southwestern United States summer monsoon source-Gulf of Mexico or Pacific Ocean? *J. Appl. Meteor.*, **13**, 331-342.

Hales, J. E., Jr., 1975: A severe southwestern desert thunderstorm: 19 August 1973. *Mon. Wea. Rev.*, **103**, 344-351.

Hastings, J. R., and R. Turner, 1965: Seasonal precipitation regimes in Baja California. *Geogr. Ann.*, **47A**, 204-223.

Higgins, R. W., Y. Chen, and A. Douglas, 1999: Interannual variability of the North American warm season precipitation regime. *J. Climate*, **12**, 653-680.

Higgins, R. W., W. Shi, and C. Hain, 2004: Relationships between Gulf of California moisture surges and precipitation in the southwestern United States. *J. Climate*, **17**, 2983-2997.

Higgins, R. W., W. Shi, 2005: Relationships between Gulf of California moisture surges and tropical cyclones in the eastern Pacific basin. *J. Climate*, **18**, 4601-4620.

- Higgins, R. W., and Coauthors, 2006: The North American Monsoon Experiment (NAME) 2004 field campaign and modeling strategy. *Bull. Amer. Meteor. Soc.*, **87**, 70-94.
- Holland, G. J., and L. M. Leslie, 1986: Ducted coastal ridging over southeast Australia. *Quart. J. Roy. Meteor. Soc.*, **112**, 731-748.
- Ives, R. L., 1949: Climate of the Sonoran desert region. *Ann. Assoc. Amer. Geogr.*, **39**, 143-187.
- Johnson, R. H., P. E. Ciesielski, B. D. McNoldy, P. J. Rogers, and R. K. Taft, 2007: Multiscale variability of the flow during the North American Monsoon Experiment. *J. Climate*, **20**, 1628-1648.
- Jones, D. M. A., 1956: Rainfall drop size-distribution and radar reflectivity. Research Rep. No. 6, Illinois State Water Survey Meteorological Laboratory, University of Illinois, Urbana, 39 pp. [Available from the Illinois State Water Survey Meteorological Laboratory, University of Illinois, Urbana, IL 61820.]
- Kelley, W. E., and D. R. Mock, 1982: A diagnostic study of upper-tropospheric cold lows over the western North Pacific. *Mon. Wea. Rev.*, **110**, 471-480.
- Klemp, J. B., R. Rotunno, W. C. Skamarock, 1997: On the propagation of internal bores. *J. Fluid Mech.*, **331**, 81-106.
- Knight, C. A., and N. C. Knight, 1973: Conical graupel. *J. Atmos. Sci.*, **30**, 118-124.
- Knupp, K., 2006: Observational analysis of a gust front to bore to solitary wave transition within an evolving nocturnal boundary layer. *J. Atmos. Sci.*, **63**, 2016-2035.
- Kuhlman, K. M., C. L. Ziegler, E. R. Mansell, D. R. MacGorman, and J. M. Straka, 2006: Numerically simulated electrification and lightning of the 29 June 2000 STEPS supercell storm. *Mon. Wea. Rev.*, **134**, 2734-2757.
- Lang, T. L., D. A. Ahijevch, S. W. Nesbitt, R. E. Carbone, S. A. Rutledge and R. Cifelli, 2007: Radar-observed characteristics of precipitating systems during NAME 2004. *J. Climate*, **20**, 1713-1733.
- Lang, T. J., S. A. Rutledge, and R. Cifelli, 2010: Polarimetric radar observations of convection in northwestern Mexico during the North American Monsoon Experiment. *J. Hydromet.*, **11**, 1345-1357.
- Latham, J., A. M. Blyth, H. J. Christian Jr., W. Deierling, and A. M. Gadian, 2004: Determination of precipitation rates and yields from lightning measurements. *J. Hydrol.*, **288**, 13-19.

- Latham, J. W. A. Petersen, W. Deierling, and H. J. Christian, 2007: Field identification of a unique globally dominant mechanism of thunderstorm electrification. *Quart. J. Roy. Meteor. Soc.*, **133**, 1453-1457.
- Li, J., S. Sorooshian, W. Higgins, X. Gao, B. Imam, K. Hsu, 2008: Influence of spatial resolution on diurnal variability during the North American monsoon. *J. Climate*, **21**, 3967-3988.
- Lorenz, E. N., 1963: Deterministic nonperiodic flow. *J. Atmos. Sci.*, **20**, 130-141.
- MacGorman, D. R., D. W. Burgess, V. Maxur, W. D. Rust, W. L. Taylor, and B. C. Johnson, 1989: Lightning rates relative to tornadic storm evolution on 22 May 1981. *J. Atmos. Sci.*, **46**, 221-250.
- Maddox, R. A., R. Canova, and L. R. Hoxit, 1980: Meteorological characteristics of flash flood events over the western United States. *Mon. Wea. Rev.*, **108**, 1866-1877.
- Maddox, R. A., D. M. McCollum, and K. W. Howard, 1995: Large-scale patterns associated with severe summertime thunderstorms over central Arizona. *Wea. Forecasting*, **10**, 763-778.
- Magono, C., 1953: On the growth of snow flake and graupel. *Sci. Repts. Yokahama Nat. Univ.*, Ser. 1, No. 2, 18-40.
- Maloney, E. D., and D. L. Hartmann, 2000: Modulation of eastern North Pacific hurricanes by the Madden-Julian oscillation. *J. Climate*, **13**, 1451-1460.
- Marshall, J. S., and W. Mc K. Palmer, 1948: The distribution of raindrops with size. *J. Meteor.*, **5**, 165-166.
- Martin, E. R., and R. H. Johnson, 2008: An observational and modeling study of an atmospheric internal bore during NAME 2004. *Mon. Wea. Rev.*, **136**, 4150-4167.
- Mejia, J. F., M. W. Douglas, and P. J. Lamb, 2010: Aircraft observations of the 12-15 July 2004 moisture surge event during the North American Monsoon Experiment. *Mon. Wea. Rev.*, **138**, 3498-3513.
- Mesinger, F. and co-authors, 2006: North American regional reanalysis. *Bull. Amer. Meteor. Soc.*, **87**, 343-360.
- Miles, J. W., 1977: Diffraction of solitary waves. *Z. Angew. Math. Phys.*, **28** 889-902.
- Nesbitt, S. W., E. J. Zipser, and D. J. Cecil, 2000: A census of precipitation features in the tropics using TRMM: Radar, ice scattering and lightning observations. *J. Climate*, **13**, 4087-4106.

- Orville, R. E., G. R. Huffines, W. R. Burrows, and K. L. Cummins, 2011: The North American lightning detection network (NLDN)-analysis of flash data: 2001-09. *Mon. Wea. Rev.*, **139**, 1305-1322.
- Petersen, W. A., and S. A. Rutledge, 2001: Regional variability in tropical convection: Observations from TRMM. *J. Climate*, **14**, 3566-3596.
- Petersen, W. A., H. J. Christian, and S. A. Rutledge, 2005: TRMM observations of the global relationship between ice water content and lightning. *Geophys. Res. Lett.*, **32**, L14819, doi:10.1029/2005GL023236.
- Pruppacher, H. R., and J. D. Klett, 1997: *Microphysics of Clouds and Precipitation*, 2nd Ed, Springer, 954 pp.
- Pytlak, E., M. Goering, and A. Bennett, 2005: Upper Tropospheric Troughs and Their Interaction with the North American Monsoon. *Preprints, 19th Conf. On Hydrology, 85th Annual Amer. Meteor. Soc. Meeting*, San Diego, CA, Amer. Meteor. Soc., JP2.3.
- Ralph, F. M., P. J. Neiman, P. O. G. Persson, J. M. Bane, M. L. Cancillo, J. M. Wilczak, and W. Nuss, 2000: Kelvin waves and internal bores in the marine boundary layer inversion and their relationship to coastal trapped wind reversals. *Mon. Wea. Rev.*, **128**, 283-300.
- Rasmussen, E. N., and D. O. Blanchard, 1998: A baseline climatology of sounding-derived supercell and tornado forecast parameters. *Wea. Forecasting*, **13**, 1148-1164.
- Rasmusson, E. M., 1967: Atmospheric water vapor transport and the water balance of North America, Part 1: Characteristics of the water vapor flux field. *Mon. Wea. Rev.*, **95**, 403-426.
- Reason, C. J. C., and D. G. Steyn, 1988: Comment on “Diffraction of solitary Kelvin waves at Cape Mendocino.” *Mon. Wea. Rev.*, **116**, 804-805.
- Reason, C. J. C., and D. G. Steyn, 1992: The Dynamics of Coastally Trapped Ridges in the Lower Atmosphere. *J. Atmos. Sci.*, **49**, 1677-1692.
- Reed, T. R., 1933: The North American high-level anticyclone. *Mon. Wea. Rev.*, **61**, 321-325.
- Reinking, R. F., 1975: Formation of Graupel. *J. Appl. Meteor.*, **14**, 745-754.

- Reitan, C. H., 1957: The role of precipitable water vapor in Arizona's summer rains. Tech Rep. on the Meteorology and Climatology of Arid Regions 2, The Institute of Atmospheric Physics, The University of Arizona, Tucson, 19 pp. [Available from The Institute of Atmospheric Physics, The University of Arizona, Tucson, AZ 85721.]
- Reiter, E. R., and M. Tang, 1984: Plateau effects on diurnal circulation patterns. *Mon. Wea. Rev.*, **112**, 638-651.
- Reynolds, S. E., M. Brook, and M. F. Gourley, 1957: Thunderstorm charge separation. *J. Meteor.*, **14**, 163-178.
- Rogers, P. J., and R. H. Johnson, 2007: Analysis of the 13-14 July gulf surge event during the 2004 North American Monsoon Experiment, *Mon. Wea. Rev.*, **135**, 3098-3117.
- Rottman, J. W., and J. E. Simpson, 1989: The Formation of Internal Bores in the Atmosphere: A Laboratory Model. *Quart. J. Roy. Meteor. Soc.*, **115**, 941-963.
- Rotunno, R., M. L. J. B. Klemp, and M. L. Weisman, 1988: A theory for strong, long-lived squall lines. *J. Atmos. Sci.*, **45**, 463-485.
- Rowe, A. K., S. A. Rutledge, T. J. Lang, P. E. Ciesielski, and S. M. Saleeby, 2008: Elevation-dependent trends in precipitation observed during NAME. *Mon. Wea. Rev.*, **136**, 4962-4979.
- Sadler, J. C., 1967: The tropical upper-tropospheric trough as a secondary source of typhoons and a primary source of trad-wind disturbances. Hawaii Institute of Geophysics Rep. 67-12, 103 pp. [Available from HIG, 2525 Correa Rd., Honolulu HI 96822.]
- Saunders, C. P. R., W. D. Keith, and R. P. Mitzeva, 1991: The effect of liquid water on thunderstorm charging. *J. Geophys. Res.*, **96**, 11 007- 11 017.
- Simpson, J. E., 1982: Gravity currents in the laboratory, atmosphere, and ocean. *Annual Rev. Fluid Mech.*, **14**, 213-234.
- Simpson, J. E., 1997: Gravity currents in the environment and the laboratory. Cambridge University Press, 244 pp.
- Skamarock, W. C., R. Rotunno, and J. B. Klemp, 1999: Models of Coastally Trapped Disturbances. *J. Atmos. Sci.*, **56**, 3350-3365.
- Smith, W. P., and R. L. Gall, 1989: Tropical squall lines of the Arizona monsoon. *Mon. Wea. Rev.*, **117**, 1553-1569.

- Stensrud, D. J., R. L. Gall, S. L. Mullen, and K. W. Howard, 1995: Model climatology of the Mexican monsoon. *J. Climate*, **8**, 1775-1793.
- Stensrud, D. J., R. L. Gall, and M. K. Nordquist, 1997: Surges over the Gulf of California during the Mexican monsoon. *Mon. Wea. Rev.*, **125**, 417-437.
- Takahashi, T., 1978: Riming electrification as a charge generation mechanism in thunderstorms. *J. Atmos. Sci.*, **35**, 1536-1548.
- Tang, M., and E. R. Reiter, 1984: Plateau monsoons of the Northern Hemisphere: A comparison between North American and Tibet. *Mon. Wea. Rev.*, **112**, 617-637.
- Tessendorf, S. A., K. C. Wiens, and S. A. Rutledge, 2007: Radar and lightning observations of the 3 June 2000 electrically inverted storm from STEPS. *Mon. Wea. Rev.*, **135**, 3665-3681.
- Thompson, G., P. R. Field, R. M. Rasmussen, and W. D. Hall, 2008: Explicit forecasts of winter precipitation using an improved bulk microphysics scheme. Part II: Implementation of a new snow parameterization. *Mon. Wea. Rev.*, **136**, 5095-5115.
- Thorncroft, C. D., B. J. Hoskins, and M. E. McIntyre, 1993: Two paradigms of baroclinic-wave life-cycle behavior. *Quart. J. Roy. Meteor. Soc.*, **119**, 17-55.
- Uccellini, L. W., and D. R. Johnson, 1979: Coupling of upper and lower tropospheric jet streaks and implications for the development of severe convective storms. *Mon. Wea. Rev.*, **107**, 682-703.
- Vera, C. and Coauthors, 2006: Toward a unified view of the American monsoon systems. *J. Climate*, **19**, 4977-5000.
- Wakimoto, R. M., 1982: The life cycle of thunderstorm gust fronts as viewed with Doppler radar and rawinsonde data. *Mon. Wea. Rev.*, **110**, 1060-1082.
- Watts, C. J., R. L. Scott, J. Garatua-Payan, J. C. Rodriguez, J. H. Prueger, W. P. Kustas, and M. Douglas, 2007: Changes in vegetation condition and the surface fluxes during NAME 2004. *J. Climate*, **20**, 1810-1820.
- Wiens, K. C., S. A. Rutledge, and S. A. Tessendorf, 2005: The 29 June 2000 supercell observed during STEPS, part II: Lightning and charge structure. *J. Atmos. Sci.*, **62**, 4151-4177.
- Weickmann, H., 1953: Observational data on the formation of precipitation in cumulonimbus clouds. *Thunderstorm Electricity*, H. R. Byers, Ed., The University of Chicago Press, 66-138.

- Weisman, M. L., J. B. Klemp, R. Rotunno, 1988: Structure and evolution of numerically simulated squall lines. *J. Atmos. Sci.*, **45**, 1990-2013.
- Weisman, M. L., and R. Rotunno, 2004: “A theory for strong long-lived squall lines” revisited. *J. Atmos. Sci.*, **61**, 361-382.
- Weisman, M. L., C. Evans, and L. F. Bosart, 2011: The 8 May 2009 “super-derecho”: analysis of a 3 km WRF-ARW real-time forecast. *Mon. Wea. Rev.*, submitted.
- Whitfield, M. B., and S. W. Lyons, 1992: An upper-level low over Texas during summer. *Wea. Forecasting*, **7**, 89-106.
- Williams, E. R., and R. M. Lhermitte, 1983: Radar tests of the precipitation hypothesis for thunderstorm electrification. *J. Geophys. Res.*, **88**, 10 984-10 992.
- Wolff, J., L. Nance, J. H. Gotway, P. Oldenburg, M. Harrold, and Z. Trabold, 2011: WRF QNSE test and evaluation. Preprints, *20th Conference on Numerical Weather Prediction*, Seattle, WA. Amer. Meteor. Soc., P470, 12 pp.
- Workman, E. J., and S. E. Reynolds, 1949: Electrical activity as related to thunderstorm cell growth. *Bull. Amer. Meteor. Soc.*, **30**, 142-149.
- Zehnder, J. A., 2004: Dynamic mechanisms of the Gulf surge. *J. Geophys. Res.*, **109**, D10107, doi:10.1029/2004JD004616.

LIST OF ABBREVIATIONS

AC1	Across-the-GoC 1
AC2	Across-the-GoC 2
AC3	Across-the-GoC 3
AC4	Across-the-GoC 4
AC5	Across-the-GoC 5
AG1	Along-the-GoC 1
AGL	Above Ground Level
ARW	Advanced Research WRF
CAPE	Convective Available Potential Energy
CG	Cloud-to-Ground
CM1	Cloud Model 1
CS	Cross-Section
CSL	Cabo San Lucas
ECMWF	European Center for Medium-Range Weather Forecasts
EOF	Empirical Orthogonal Function
F1	Feature 1
F2	Feature 2
GFS	Global Forecast System
GoC	Gulf of California

GOES	Geostationary Operational Environmental Satellite
GoM	Gulf of Mexico
GUA	Guasave
IOP	Intensive Observing Period
ISS	Integrated Sounding System
KB	Kino Bay
LCL	Lifted Condensation Level
LLJ	Low-level Jet
LM	Los Mochis
MSLP	Mean Sea Level Pressure
NA	North America
NAM	North American Monsoon
NAME	North American Monsoon Experiment
NARR	North American Regional Reanalysis
NCAR	National Center for Atmospheric Research
NLDN	National Lightning Detection Network
NMM	Nonhydrostatic Mesoscale Model
NOAA	National Oceanic and Atmospheric Administration
PP	Puerto Penasco
PW	Precipitable Water
QNSE	Quasi-Normal Scale Elimination
RASS	Radio Acoustic Sounding System
RS2007	Rogers and Johnson (2007)

S1	Structure 1
S2	Structure 2
SMN	Servicio Meteorologico Nacional
SMO	Sierra Madre Occidental
SOR	Successive Over-Relaxation
SPOL	NCAR polarimetric radar
TC	Tropical Cyclone
TD	Tropical Depression
TEW	Tropical Easterly Wave
TS	Tropical Storm
TUTT	Tropical Upper Tropospheric Trough
US	United States
USGS	United States Geological Survey
WPP	WRF Post Processor
WPS	WRF Preprocessing System
WRF	Weather Research and Forecasting
YSU	Yonsei University